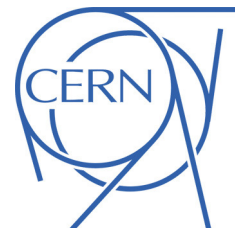# ATLAS NOTE

March 1, 2011

Measurement of the inclusive isolated prompt photon cross section in pp collisions at $\sqrt{s}$ = 7 TeV with the ATLAS detector

H. Abreu, N. Andari, C. Becot, R. Blair, F. Bucci, L. Carminati, S. Chekanov, V. Dao,
R.K. Daya, M. Delmastro, M.T. Dova, M. Escalier, M. Fanti, L. Fayard, E. Fuchs,
A. Hamilton, M. Hance, P. Harrau, J. Huston, M. Jimenez Belenguer, R. Ishmukhametov,
M. Kado, T. Koffas, Z. Liang, M. Liu, J.F. Marchand, G. Marchiori, B. Martin, V. Perez Reale,
J. Saxon, M. Stockton, K. Tackmann, H.J. Torres Davila, M. Tripiana, R. Turra, G. Unal,
P. Waller, H.H. Williams, L. Yuan

Abstract

The first measurement of the cross section for the inclusive production of isolated prompt photons in pp collisions at a center-of-mass energy $\sqrt{s}$ = 7 TeV is presented. The measurement covers the pseudorapidity ranges $|\eta^\gamma| < 1.37$ and $1.52 \leq |\eta^\gamma| < 1.81$, in the transverse energy range $15 \leq E_T^\gamma < 100$ GeV. The results are based on an integrated luminosity of 880 nb^{-1}, collected with the ATLAS detector at the LHC. Photon candidates are identified by exploiting the fine granularity of the electromagnetic calorimeter, which provides event-by-event rejection of the dominant background from photons produced by π^0 decays, and of the inner detector, which allows the reconstruction of photons that convert to electron-positron pairs. Residual background in the selected sample is estimated using data-driven techniques based on the observed distribution of the isolation energy in a narrow cone around the photon candidate. The results are compared with next-to-leading order perturbative QCD calculations.

Contents

1 Introduction

Prompt photon production at hadron colliders provides a handle for testing perturbative QCD predictions [1]. They provide a colorless probe of the hard scattering process at leading order, and are directly sensitive to the gluon content of the proton (through the $qg \rightarrow q\gamma$ process, which dominates the leading-order production of prompt photons at the LHC). It can also be used to constrain parton structure functions [2]. Furthermore, photon identification is important for many physics signatures, including searches for Higgs boson or graviton decays to photon pairs, decays of excited fermions, and decays of pairs of supersymmetric particles, characterized by the production of two energetic photons and large missing transverse energy. Prompt photon production has a significantly higher cross section at the LHC compared to the Tevatron and HERA. The prompt-photon cross section at the LHC is more than a factor of thirty higher than at Tevatron, and a factor of 10^4 higher than for photoproduction at HERA, assuming a similar kinematic range in transverse momentum and pseudorapidity [3]. This will allow the exploration of the TeV energy scale after only a few years of data taking.

In the following, all photons produced in proton-proton collisions not coming from hadron decays are considered as "prompt". They include both "direct" photons, which take part in the hard subprocess (the photons originating from all the Feynman diagrams with a photon leg), and "fragmentation" photons, which are the result of the fragmentation of a colored high p_T parton [4, 5]. Photons are considered isolated, from a theoretical perspective, if the amount of hadronic transverse energy E_T^{iso} carried by all the colored partons within a cone, centered around the photon direction in the pseudorapidity (η) and azimuthal angle (ϕ) plane, is smaller than some value:

$$\text{for} \quad (\eta - \eta^\gamma)^2 + (\phi - \phi^\gamma)^2 \leq R^2, \qquad E_T^{iso} \leq E_T^{cut} \tag{1}$$

The isolation criterion used in this note to define true isolated photons is $E_T^{iso} < 4$ GeV in a cone of radius $R = 0.4$. The corresponding experimental isolation variable used to define an isolated photon at reconstruction level is described in Section 4.4. As pointed out in [5], the isolated cross section cannot be identified with only the direct cross section, since there is a residual contribution to the prompt photon signal from fragmentation processes. The background consists of all photon candidates that are not real isolated prompt photons: they will also be called "fake" photons in the following. In a hadron collider environment, the main background is composed of photons from decays of light neutral mesons like π^0 or η.

This note describes the extraction of a signal of isolated prompt photons with transverse energies above 15 GeV from the background using (880 ± 100) nb^{-1} of data collected by ATLAS between April and August 2010, and the first ATLAS measurement of the isolated prompt photon production cross section in pp collisions at $\sqrt{s} = 7$ TeV, in the pseudorapidity ranges $|\eta^\gamma| < 0.6$, $0.6 \leq |\eta^\gamma| < 1.37$ and $1.52 \leq |\eta^\gamma| < 1.81$, in the transverse energy range $15 \leq E_T^\gamma < 100$ GeV. The pseudorapidity range $1.81 \leq |\eta^\gamma| < 2.37$ has also been investigated; however, due to large uncertainties in the photon identification efficiencies in that region, it has been excluded from the final measurement.

Recent measurements of the inclusive prompt photon cross section at the Tevatron, in $p\bar{p}$ collision at a centre-of-mass energy $\sqrt{s} = 1.96$ TeV, are reported in Refs. [6, 7]. The measurement by the D0 Collaboration [6] is based on 326 pb^{-1} and covers a pseudorapidity range $|\eta^\gamma| < 0.9$ and a transverse energy range $23 < E_T^\gamma < 300$ GeV, while the measurement by the CDF Collaboration [7] is based on 2.5 fb^{-1} and covers a pseudorapidity range $|\eta^\gamma| < 1.0$ and a transverse energy range $30 < E_T^\gamma < 400$ GeV. Both D0 and CDF measure an isolated prompt photon cross section in agreement with next-to-leading order (NLO) perturbative QCD calculations, with a slight excess seen by CDF in their data between 30 and 50 GeV.

The note is organized as follows. In Section 2, the note begins by briefly recalling the main characteristics of the ATLAS detector. Section 3 summarizes the data and simulated samples used for this

analysis. Section 4 describes the various steps of the photon identification together with a comparison between data and Monte Carlo (MC) simulations. Section 5 illustrates the expected photon identification and trigger efficiencies. Section 6 describes the methods used to derive the residual background from the data and to extract the prompt photon signal, together with the associated systematic uncertainties. In Section 7 the isolated prompt photon production cross section is measured from the observed signal transverse energy distribution, the estimated photon efficiency, the total integrated luminosity and the unfolding of the detector finite energy resolution. In Section 8 the sources of systematic uncertainties on the cross section measurement are identified and the corresponding uncertainties are estimated. In Section 9 the NLO perturbative QCD (pQCD) predictions for the isolated prompt photon production cross section are computed and compared with the experimental results.

2 The ATLAS detector

The ATLAS detector is described in detail in Ref. [8]. The main features of the subdetectors relevant to this analysis are summarized here, including the inner detector and the calorimeter (in particular its electromagnetic section).

The inner detector is comprised of three subsystems: at small radial distance r from the beam axis ($50.5 < r < 150$ mm), pixel silicon detectors are arranged in three cylindrical layers in the barrel and in three disks in each end-cap; at intermediate radii ($299 < r < 560$ mm), double layers of single-sided silicon microstrip detectors are used, organized in four cylindrical layers in the barrel and nine disks in each end-cap; at larger radii ($563 < r < 1066$ mm), a straw tracker with transition radiation detection capabilities divided into one barrel section (with 73 layers of straws parallel to the beam line) and two end-caps (with 160 layers each of straws radial to the beam line) is used. These three systems lie within in a 2 T axial magnetic field produced by a superconducting solenoid. The inner detector has full coverage in ϕ. The silicon pixel and strip subsystems cover the pseudorapidity range $|\eta| < 2.5$, while the transition radiation tracker acceptance is limited to the range $|\eta| < 2.0$. The inner detector allows an accurate reconstruction of tracks from the primary proton-proton collision point and also from secondary vertices, permitting an efficient reconstruction of photon conversions in the inner detector material up to a radius of ≈ 80 cm.

The electromagnetic calorimeter is a lead-liquid Argon (Pb-LAr) sampling calorimeter with an accordion geometry. It is divided in a barrel section covering the pseudorapidity region $|\eta| < 1.475$ and two end-cap sections covering the pseudorapidity regions $1.375 < |\eta| < 3.2$. It consists of three longitudinal layers. The first layer, with a thickness between 3 and 5 radiation lengths, has a very high granularity in the η direction (between 0.003 and 0.006 depending on η, with the exception of the regions $1.4 < |\eta| < 1.5$ and $|\eta| > 2.4$), sufficient to provide an event-by-event discrimination between single photon showers and proximate double showers coming from a π^0 decay. The second layer of the electromagnetic calorimeter, which collects most of the energy deposited in the calorimeter by the photon shower, has a thickness of around 17 radiation lengths and a granularity of 0.025×0.025 in $\eta \times \phi$, where ϕ is the azimuthal coordinate around the beam z axis. A third layer, with thickness varying between 4 and 15 radiation lengths, is used to correct leakage beyond the calorimeter for high energy showers. Before the accordion calorimeter, a thin presampler layer, covering the pseudorapidity interval $|\eta| < 1.8$, is used to correct fluctuations of energy loss before the calorimeter. The sampling term a of the energy resolution ($\sigma(E)/E \approx a/\sqrt{E \text{ (GeV)}}$) varies between 10% and 17% as a function of $|\eta|$ [9], and is the largest contribution to the resolution up to about 200 GeV, where the global constant term (0.7%) starts to dominate [10]. The total amount of material before the first active layer of the electromagnetic calorimeter (including the presampler) varies between 2.5 and 6 radiation lengths as a function of pseudorapidity, excluding the transition region ($1.37 < |\eta| < 1.52$) between the barrel and the end-caps, where the material thickness increases to 11.5 radiation lengths. A proper description of this material is important for accurate modeling of the

calorimeter response including the detailed shape of electromagnetic showers.

Between April and August 2010, when the data analysed for the cross section measurement presented in this article were collected, a certain number of optical links in the calorimeter readout system were non-functional. This number increased over time; in the latest weeks of data taking, in the period between runs 159040 and 160980 (which corresponds to 87% of the total integrated luminosity used for this measurement) about 25 out of 1524 optical links were non-functional. The (η, ϕ) maps of the dead readout optical links for the presampler, first and second sampling layers for data collected between runs 159040 and 160980 are shown in Figure 1.

(a) Presampler   (b) First Sampling   (c) Second Sampling
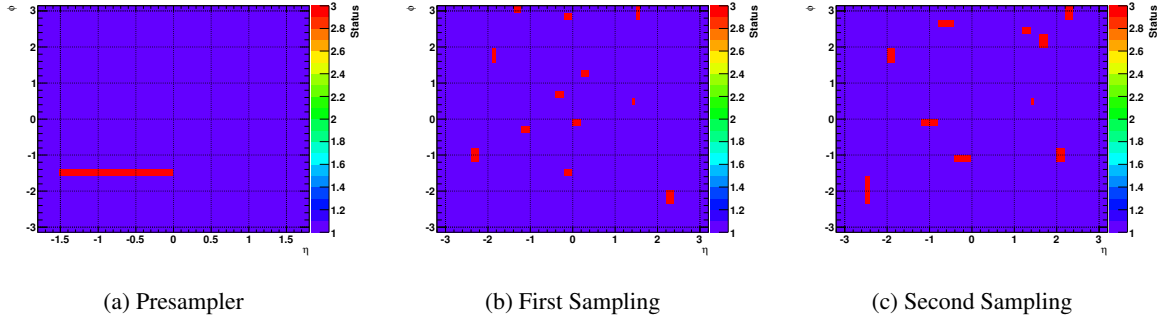
Figure 1: Maps of the dead front-end board (FEB) links for the presampler, first sampling, and second sampling for runs after 159040, corresponding to the bulk of the data used in this analysis. Photon candidates that fall into the red regions are ignored.

A hadronic sampling calorimeter is located beyond the electromagnetic calorimeter. It is made of steel and scintillating tiles in the barrel section, with depth around 7.4 interaction lengths, and of two wheels of copper and liquid argon in each end-cap, with depth around 9 interaction lengths. In this analysis the hadronic calorimeter is used to reduce background due to photons from neutral hadron decays, exploiting the fact that energy leakage in the hadronic calorimeters from isolated prompt photons is lower than that for fake photons from decays of π^0 or other neutral hadrons in jets, since the latter are accompanied by nearby hadrons produced in the same jet.

3 Collision data and simulated samples

3.1 Collision Data

The measurement presented here is based on proton-proton collision data collected at a centre-of-mass energy $\sqrt{s} = 7$ TeV with the ATLAS detector at the LHC between April and August 2010. Data taken between ATLAS run periods A and E4 have been included in the analysis. The total integrated luminosity of the sample, as used in the measurement, is 880 ± 100 nb^{-1}.

3.1.1 Trigger Requirements

Events are triggered using the `g10_loose` high-level calorimeter trigger, based on the energy deposits in the electromagnetic and hadronic calorimeters. The `g10_loose` high-level trigger is seeded by a level-1 hardware trigger (`L1_EM5`), which, using a coarser granularity (0.1×0.1 in $\eta \times \phi$) than that of the electromagnetic calorimeter, searches for electromagnetic clusters with fixed size 0.2×0.2 and retains only those whose total transverse energy in two of their four trigger channels is above 5 GeV. The high level trigger exploits the full granularity and precision of the calorimeter to refine the level-1 trigger

selection, based on improved energy resolution and detailed information on energy deposition in the calorimeter cells. The nominal transverse energy threshold of the `g10_loose` trigger is 10 GeV. The selection criteria that are applied by the trigger on the fraction and profile of the energy released in the various layers of the calorimeters are looser than the photon identification criteria applied in the following analysis steps, and are chosen, together with the transverse energy threshold value, in order to reach a plateau of constant efficiency close to 100% for true photons with $E_T > 15$ GeV.

3.1.2 Data Quality

Only events where both the calorimeter and the inner detector are fully operational, and have good data quality, are used. In particular, events are required to belong to the $Z \rightarrow ee\ e/\gamma$ "Good Runs List" (GRL).[1]

3.1.3 Total Integrated Luminosity

The total integrated luminosity of the selected sample, after trigger and GRL requirements, is (880 ± 100) nb^{-1}. A detailed list of all the runs included in this measurement, and the corresponding `g10_loose` integrated luminosities, is available in Table 1.

3.1.4 Primary Vertex Requirement

For this analysis, events are required to have a reconstructed primary vertex consistent with the average beam spot position and with at least three associated tracks. The efficiency of this requirement is greater than 99.9% both in data and in simulated signal events containing at least one photon candidate with transverse energy above 15 GeV (and lying within the calorimeter acceptance). The total number of selected events is 9.6 million.

3.1.5 Non-Collision Backgrounds

The amount of non-collision background in the data sample is estimated with control samples collected using a dedicated, low-threshold calorimetric trigger. This trigger selects events that either have no proton bunch passing through the interaction region (for cosmic background studies), or in which there is only one bunch corresponding to a single beam (for non-collision beam-induced background studies). The contribution to the final candidate sample was found to be negligible (see Section 9 of [11]).

Run Number	Data Period	Good LB	Bad LB	Luminosity [nb^{-1}]
152166	A	47	48	0.0029
152214	A	43	0	0.0032
152221	A	163	0	0.0210
152345	A	80	0	0.0161
152409	A	589	1	0.0794
152441	A	359	1	0.0672
152508	A	66	0	0.0109
152777	A	249	1	0.0453
152844	A	55	1	0.0078
152845	A	239	0	0.0262

---

[1]Note that the same quality requirements apply for electrons from Z and photons.

Run Number	Data Period	Good LB	Bad LB	Luminosity [nb^{-1}]
152878	A	114	1	0.0250
152933	A	128	1	0.0215
152994	A	59	1	0.0053
153030	A	83	0	0.0225
153134	A	42	1	0.0057
153136	A	20	1	0.0021
153159	A	89	1	0.0112
153200	A	36	0	0.0078
153565	B	893	0	0.7653
154810	B	62	0	0.1526
154813	B	128	0	0.2624
154815	B	30	0	0.0618
154817	B	279	0	0.5339
155073	B	318	5	1.1564
155112	B	474	0	3.4111
155116	B	83	0	0.4992
155160	B	263	0	1.3289
155228	C1	16	0	0.0385
155280	C1	16	0	0.0284
155569	C1	240	0	0.9909
155634	C1	186	0	1.0697
155669	C1	54	0	0.4409
155678	C1	68	0	1.1924
155697	C1	240	0	3.4226
156682	C2	105	0	1.3008
158045	D1	61	0	0.7205
158116	D1	413	0	14.4433
158269	D1	75	0	3.4323
158299	D1	71	0	1.3367
158392	D1	212	0	7.6043
158466	D2	16	0	1.6204
158545	D2	23	0	1.3337
158548	D2	196	0	10.0807
158549	D2	85	0	3.1816
158582	D2	307	0	16.0859
158632	D3	110	0	5.5031
158801	D3	177	0	7.1641
158975	D3	219	0	20.5129
159041	D4	259	0	25.6413
159086	D4	404	0	54.0469
159113	D5	256	0	28.0369
159179	D6	108	0	15.0164
159202	D6	81	0	9.7998
159203	D6	79	0	8.2898
159224	D6	539	0	64.2961

Continued on following page

Run Number	Data Period	Good LB	Bad LB	Luminosity [nb^{-1}]
160387	E1	235	0	58.4255
160472	E1	366	0	76.3450
160479	E1	25	0	4.6985
160530	E2	424	0	92.4522
160613	E3	189	0	48.0307
160736	E3	59	0	17.1593
160800	E3	61	1	16.1291
160801	E3	370	0	75.7851
160879	E3	409	0	80.6187
160899	E4	15	0	4.8064
160953	E4	53	0	19.4108
160954	E4	62	1	16.6286
160958	E4	195	0	40.6305
160963	E4	13	0	2.3340
160980	E4	30	0	8.9862
Total	A-E4	12113	65	877.603

Table 1: Runs used in the inclusive photon analysis, which cover all runs through period E4, except runs 158443 and 160975, which had prescales applied on the g10_loose trigger chain. A lumi block (LB) is bad either if the trigger was disabled, or if the luminosity value for that lumi block in the database is invalid.

3.2 Simulated events

To study the characteristics of signal and background events, Monte Carlo samples are generated using PYTHIA 6.4.21 [12], a leading-order (LO) parton-shower MC generator, with the modified leading order MRST2007 [13] parton distribution functions (PDFs). The event generator parameters are set according to the ATLAS MC09 tune [14], and the ATLAS detector response is simulated using the GEANT4 program [15]. These samples are then reconstructed with the same algorithms used for data. More details on the event generation and simulation infrastructure of the ATLAS experiment are provided in Ref. [16]. For the study of systematic uncertainties related to the choice of the event generator and the parton shower model, alternative samples are also generated with HERWIG 6.5 [17]. For a summary of the relevant simulated samples, see Table 2.

To study background processes, two classes of samples are simulated. In the first one, generated non-diffractive minimum bias events are filtered requiring at least 6 GeV of transverse energy in a 0.18×0.18 region in $\eta \times \phi$ at the truth particle level, mimicking a calorimetric L1 trigger requirement. The events passing this filter, whose efficiency is around 5.3%, are then fully simulated. This filter is found to be unbiased for transverse energies above 10 GeV. The equivalent integrated luminosity of this sample, according to the effective production cross section (including the filter efficiency) $\sigma = 2.58$ mb returned by PYTHIA, is 16 nb^{-1}.

Since the E_T spectrum of reconstructed fake candidates decreases rapidly above the filter threshold, a second class of samples, enriched in candidates with higher transverse energies, is used to study fake photon candidates with reconstructed $E_T > 20$ GeV. In these samples, all relevant 2→2 QCD hard subprocesses (see Table 3). are switched on, the transverse momentum of the hard-scattering products is required to be greater than (at least) 15 GeV, and the same filter as for the minimum bias sample is applied. The filter has a higher threshold than in the minimum bias sample, with cuts at 17 and 35 GeV

Table 2: Monte Carlo datasets used in the inclusive photon analysis. All samples contain all relevant signal processes, unless otherwise indicated. The QCD samples contain both prompt photon production events and the most significant sources of background as summarized in Table 3.

Data Set	Process	σ	Filter type	Filter threshold	Filter efficiency	Events in tuples	Equivalent luminosity	Generator
		[pb]		[GeV]			[pb^{-1}]	
105801	QCD	4.845E+10	1 jet	6	5.32E-2	39957193	1.55E-2	PYTHIA
105802	QCD	1.148E+9	1 jet	17	8.62E-2	48931022	4.94E-1	PYTHIA
105807	QCD	5.484E+7	1 jet	35	1.57E-1	4992566	5.79E-1	PYTHIA
105802	QCD	9.162E+8	1 jet	17	8.26E-2	9969117	1.32E-1	HERWIG
105807	QCD	4.396E+7	1 jet	35	1.43E-1	4884587	7.77E-1	HERWIG
115801	QCD	4.911E+10	1 prompt γ	7	9.77E-5	989274	2.06E-1	PYTHIA
115802	QCD	1.147E+9	1 prompt γ	17	1.83E-4	964406	4.60E+0	PYTHIA
115871	QCD	3.924E+10	1 prompt γ	7	1.65E-4	999189	1.54E-1	HERWIG
115872	QCD	9.162E+8	1 prompt γ	17	1.08E-4	927922	9.41E+0	HERWIG
108085	γ-jet	5.015E+6	1 prompt γ	7	2.76E-1	999631	7.21E-1	PYTHIA
108087	γ-jet	2.250E+5	1 prompt γ	17	4.70E-1	4994464	4.72E+1	PYTHIA
108081	γ-jet	1.731E+4	1 prompt γ	35	6.04E-1	1998486	1.91E+2	PYTHIA
108082	γ-jet	1.521E+3	1 prompt γ	70	6.63E-1	999662	9.92E+2	PYTHIA
105830	γ-jet	1.963E+5	1 prompt γ	17	4.66E-1	4988495	5.46E+1	HERWIG
105831	γ-jet	1.478E+4	1 prompt γ	35	6.01E-1	1999395	2.25E+2	HERWIG
108092	γ-jet	1.282E+3	1 prompt γ	70	6.52E-1	998963	1.11E+3	HERWIG
106043	$W \to e\nu$	8.938E+3	None	None	1.00E+0	6995437	7.84E+2	PYTHIA

The sample with a 17 GeV minimum is found to be unbiased for transverse energies above 20 GeV. Its equivalent integrated luminosity, according to the effective production cross section σ = 0.99 mb computed with PYTHIA (taking into account also the filter efficiency, 8.6%), is 494 nb^{-1}. The sample with a parton-level p_T cut at 33 GeV and a truth-particle-jet filter cut at 35 GeV helps us to extend the reach to higher transverse energies, and corresponds to an integrated luminosities of 579 nb^{-1}.

Table 3: Elementary QCD processes that are enabled in the QCD PYTHIA samples.

Process	PYTHIA subcode
$q_i q_j \to q_i q_j$	11
$q_i \bar{q}_i \to q_k \bar{q}_k$	12
$q_i q_i \to gg$	13
$q_i g \to q_i g$	28
$gg \to q_k \bar{q}_k$	53
$gg \to gg$	68
$q_i \bar{q}_i \to Q_k \bar{Q}_k$	81
$gg \to Q_k \bar{Q}_k$	82
$q_i \bar{q}_i \to g\gamma$	14
$q_i g \to q_i \gamma$	29

All of these QCD background samples contain "fake" photon candidates (typically from π^0 and η decays), as well as prompt photon signals produced by QED radiation emitted off quarks and by parton fragmentation. The higher energy sample contains also the contribution of the direct LO gamma-jet hard-scattering contributions, either from $q_i \bar{q}_i \to g\gamma$ or $q_i g \to q_i \gamma$. Reconstructed prompt photon candidates are matched to particles in the truth record of the event with the ATLAS McTruthClassifier tool, which uses a combination of ancestry information and ΔR matching to determine whether a candidate is signal or background. All prompt photon contributions are removed from these samples when studying

9

the background contribution.

Signal-like photons are present in all of the relevant datasets, either as the result of a filter which selects only signal photons at the generator level, or as part of a sample which also contains background processes. For signal-only samples, two types of filters are used. The first class of prompt photon samples consists of simulated leading order γ-jet events, and contains only hard-scattering photons (hard subprocesses $qg \rightarrow q\gamma$ and $q\bar{q} \rightarrow g\gamma$) with generated transverse momenta above some threshold (7, 17, 35 or 70 GeV thresholds are used in these studies). The equivalent luminosities of these samples range from 71 nb^{-1}(for a 7 GeV threshold) to 1 fb^{-1}(for a 70 GeV threshold). The box-diagram hard subprocess $gg \rightarrow g\gamma$ is part of the next-to-next-to-leading order (NNLO) cross section and gives a negligigle contribution to the total prompt photon cross section compared to the other two subprocesses. It is therefore not included in the generated samples.

The second class of signal samples contains both hard-scattering photons and photons from QED radiation off quarks, and also includes photons from parton fragmentation. The events generated for this class of samples are similar to those generated for the study of the QCD backgrounds (the same elementary processes of Table 3 are activated), but the filter applied before the full simulation only retains events that contain reconstructed photons matched to signal photons in the truth record, with generated transverse momenta above some threshold, either 7 GeV or 17 GeV. The equivalent luminosities for those two samples are 206 nb^{-1}and 4600 nb^{-1}, respectively. These samples are used to study the contribution to the prompt photon signal of photons from fragmentation or from the NLO part of the direct process and that are less isolated than those from the LO direct processes. In such studies, all direct LO photon contributions are removed from these samples in the analysis.

Finally, for the efficiency and purity studies involving electrons from W decays, a pure sample of $W \rightarrow e\nu$ events is used. The sample has no generator filter applied, but consists only of events with a final state W decaying leptonically to an electron and a neutrino.

4 Photon reconstruction and identification

4.1 Photon reconstruction

Photon reconstruction and identification is seeded by clusters in the electromagnetic calorimeter with transverse energies exceeding 2.5 GeV, measured in projective towers of 3 × 5 cells in the second layer of the calorimeter. These energy clusters are then matched to tracks that are reconstructed in the inner detector and extrapolated to the calorimeter. Clusters without matching tracks are directly classified as unconverted photon candidates. Clusters with matched tracks are considered as electron candidates. To recover photon conversions, clusters matched to tracks originating from reconstructed conversion vertices in the inner detector or to tracks consistent with coming from a conversion are considered as converted photon candidates. To increase the reconstruction efficiency of converted photons, converted candidates where one of the two tracks is not reconstructed are also retained (see Refs. [10] and [18] for more details on converted photon reconstruction).

The final energy measurement, for both converted and unconverted photons, is made using only the calorimeter, with a cluster size that depends on the photon classification. In the barrel, a cluster corresponding to 3×5 cells in the second layer is used for unconverted photons, while the cluster for converted photon candidates is 3×7 cells (to compensate for the opening between the conversion products in the ϕ direction due to the magnetic field). In the end-cap, a cluster size of 5×5 is used for all candidates. A dedicated energy calibration [9] is then applied to account for upstream energy loss, lateral leakage, and longitudinal leakage. (The calibration is applied separately for converted and unconverted candidates.)

4.2 Photon preselection

Photon candidates with calibrated transverse energies (E_T) above 15 GeV are retained for the successive analysis steps. To ensure a proper identification, the cluster barycenter in the second layer of the electromagnetic calorimeter is required to lie in the pseudorapidity region covered by the very finely segmented first layer: $|\eta| < 1.37$, or $1.52 \leq |\eta| < 1.81$. For the regions briefly mentioned in the introduction, the range $1.81 \leq |\eta| < 2.37$ has not been included in the final results. In addition, for this analysis, photon candidates are selected to be outside regions of the electromagnetic calorimeter where either the presampler, first, or second layers have non working readout optical links: the full 3×7 (in the barrel) or 5×5 (in the end-cap) clusters are required not to overlap with any of these regions. Photon candidates are also rejected if one of the core 3×3 second layer cells does not work properly, or if one of the first layer cells facing the hottest cell in the second layer is non-functional. The `checkOQ.C` egamma object quality tool is used to apply these requirements. The tool makes use of run-dependent maps of dead OTX and inactive channels to remove photon candidates whose cluster overlaps with these bad regions. A summary of the dead OTX maps for the run ranges analysed in this measurement, and the integrated luminosity associated with each map, is presented in Table 4. These requirements reject 6.4% of the photon candidates reconstructed in collision data.

In the following, "preselection" is defined as the combination of criteria described in this section and the event-quality criteria defined in the previous sections:

- the event belongs to the e/γ Good Runs List (good inner detector and calorimeter data quality)

- the event passes the g10_loose trigger

- the event contains at least one primary vertex with at least three associated tracks

- the photon candidate has reconstructed $E_T > 15$ GeV and pseudorapidity in the fiducial region ($|\eta^\gamma| < 1.37$ or $1.52 \leq |\eta^\gamma| < 1.81$)

Table 4: Run periods, and equivalent luminosities, for the different object quality maps used in the inclusive photon analysis.

Run Start	Run End	Dead OTX map	Integrated Luminosity [μb^{-1}]
152166	155227	152166	8552.85
155228	155759	155228	7183.43
155760	158114	155760	2021.34
158115	158642	158115	64622.16
158643	158706	158643	0.00
158707	159039	158707	27677.04
159040	-	159040	767567.89
Total	-	-	877624.71

- the cluster of the photon candidate does not contain a bad calorimeter cell (no cell corresponding to a dead OTX in the cluster; no cell with dead HV in the core of the cluster)

After the preselection, 1.3 million photon candidates remain in the data sample. The average multiplicity of photons with $E_T > 15$ GeV and within the pseudorapidity acceptance, in events containing at least one such photon candidate, is 1.02 in collision data.

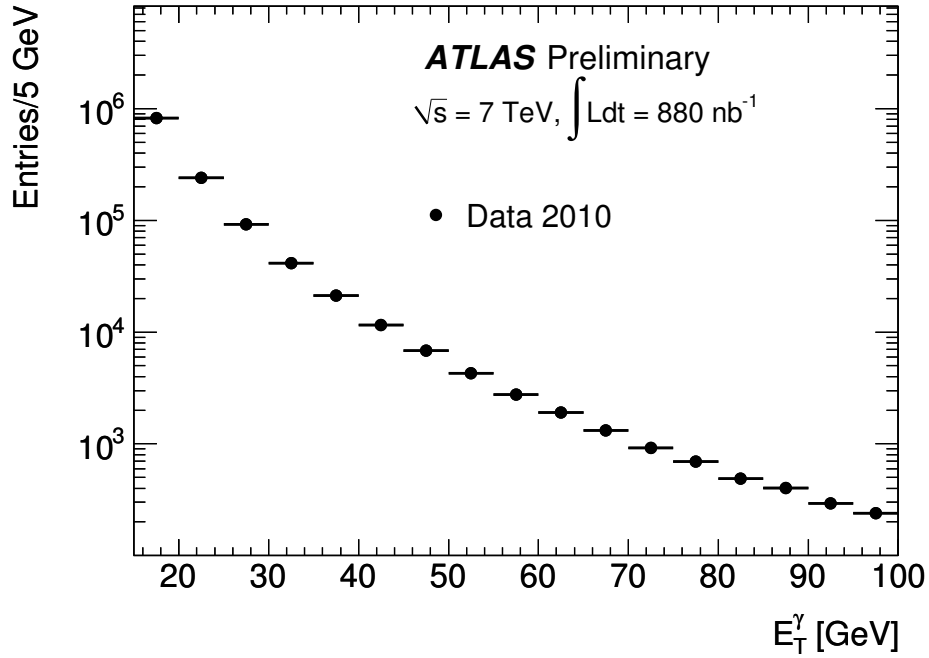The transverse energy distribution of these candidates is shown in Fig. 2.

Figure 2: Transverse energy distribution of photon candidates in data, after reconstruction and preselection, for reconstructed transverse energies between 15 and 100 GeV and pseudorapidity $|\eta^\gamma| < 1.37$ or $1.52 \le |\eta^\gamma| < 1.81$.

4.3 Photon identification

Shape variables computed from the lateral and longitudinal energy profiles of the shower in the calorimeters are used to discriminate signal from background. Two sets of cuts (a "loose" one and a "tight" one), based on independent requirements on several shape variables, are defined. Given the present level of understanding of the detector performance, more complicated multivariate techniques are not currently used. The selection criteria do not depend on the photon candidate transverse energy, but vary as a function of the photon reconstructed pseudorapidity, to take into account significant changes in the total thickness of the upstream material or variations in the calorimeter geometry or granularity.

4.3.1 Loose Selection Criteria

A set of loose selection criteria for photons is defined, based on independent requirements on three quantities:

- the leakage R_{had} in the first layer of the hadronic compartment beyond the electromagnetic cluster, defined as the ratio between the transverse energy deposited in the first layer of the hadronic calorimeter and the photon transverse energy

- the ratio R_η between the energy deposits in 3×7 over 7×7 cells in the second layer of the electromagnetic calorimeter

- the RMS width w_2 [2] of the energy distribution along η in the second layer of the electromagnetic calorimeter.

True photons are expected to have small hadronic leakage (typically below 1–2%) and a narrower energy profile in the electromagnetic calorimeter, more concentrated in the core of the cluster, with respect to photons from meson decays.

The loose selection criteria on R_{had}, R_η and w_2 are the same for converted and unconverted candidates. They have been chosen, using simulated prompt photon events, in order to obtain a true prompt photon efficiency, with respect to reconstruction, rising from 97% at $E_{\text{T}}^\gamma = 20$ GeV to above 99% for $E_{\text{T}}^\gamma > 40$ GeV for both converted and unconverted photons [10]. The number of photon candidates in data passing the preselection and loose photon identification criteria is 0.81 million, with an average multiplicity per event of 1.002 in events containing at least one such photon.

4.3.2 Tight Selection Criteria

To further reject the background, the selection requirements on the quantities used in the loose selection are tightened. In addition, the transverse shape along the ϕ direction in the second layer (a variable R_ϕ is computed from the ratio between the energy deposits in 3×3 over 3×7 cells) and the shower shape in the first layer of the calorimeter are examined. Several variables that discriminate single photon showers from overlapping nearby showers (which originate from neutral meson decays to photon pairs) are computed from the energy deposited in the first layer:

- the total RMS width $w_{s\,\text{tot}}$ of the energy distribution along η over all the strips of the cluster,

- the asymmetry E_{ratio} between the first and second maxima in the energy profile of the first layer along η (1 when there is no second maximum),

---

[2] w_2 is defined as $\sqrt{\frac{\sum E_i \eta_i^2}{\sum E_i} - \left(\frac{\sum E_i \eta_i}{\sum E_i}\right)^2}$, where the sums are computed using all the cells i of the cluster (E_i is the energy released in the cell and η_i its pseudorapidity).

- the energy difference ΔE between the second maximum and the minimum between the two maxima (0 when there is no second maximum),

- the fraction F_{side} of the energy in seven strips centered around the first maximum which is not contained in the three core strips centered around the first maximum,

- the RMS width w_{s3} of the energy distribution computed with the three core strips.

The second and third variables provide rejection against cases where the two showers give separated energy maxima in the first layer. The last two variables provide rejection against cases where the two showers are merged in a wider maximum.

The values of the cuts have been optimized using samples of simulated signal and background events prior to data taking. Different criteria are applied to converted and unconverted photon candidates: they have been chosen to nominally obtain an efficiency of 85% with respect to reconstruction for true prompt photons in both categories for transverse energies greater than 20 GeV [10]. About 0.2 million photon candidates are retained in the data sample after the tight selection, with an average multiplicity differing from one by less than 6×10^{-4} in events containing at least one tight photon candidate.

4.3.3 Robust Tight Selection Criteria

As seen for electrons in [19], the photon showers in collision data are wider in η than expected from simulation. While the exact cause of the difference between data and simulation is still under investigation, the result is a loss in efficiency for photons in collision data, due primarily to cuts on R_η and w_2 which reject more signal photons than anticipated.

To reduce this inefficiency, the tight cuts on R_η and w_2 are relaxed according to the observed differences between simulation and collision data. The differences are modeled as shifts of the individual shower shape variables, and are computed by comparing the means of the distributions for tight candidates from collisions with the corresponding values in simulation.[3] The cut is then relaxed by the observed difference, with the constraint that the new "tight" cut cannot be weaker than the loose cut on the same variable (which in turn can not be weaker than the trigger requirements on the same quantity). In those cases, the tight cut was set equal to the loose cut. The implications of these relaxed cuts are discussed in section 5.2.1. A total of 195294 candidates satisfy the combination of the preselection, acceptance, and robust-tight selection criteria. A complete description of the procedure used to define these "robust" tight cuts is given in section 2.4 of [20]. More details on the discriminating variables used to define all of the selection criteria are provided in [21].

4.4 Photon isolation energy

Isolation is an important observable for prompt photon studies. The prompt photon signal is expected to be more isolated from hadronic activity than the background from π^0 (or other neutral hadrons), where the π^0 is unlikely to carry the full original jet energy. Also, because of the mixture of hard-scattering and fragmentation contributions in the prompt photon signal, it is important to have a well modeled isolation variable that can be linked to the particle-level (or parton-level) isolation cut used in next-to-leading-order QCD computations. A robust isolation prescription will help limit the non-perturbative fragmentation contribution, which is poorly understood in theory, while retaining the signal produced at hard scales.

For the study discussed here, the isolation variable is computed using calorimeter cells from both the electromagnetic and hadronic calorimeters, in a cone of radius 0.4 in the $\eta - \phi$ space around the photon

---

[3]In the simulation case, the sample is composed of the QCD samples described in section 3.2, which contain realistic mixtures of signal and background processes.

candidate. The contributions from 5×7 electromagnetic calorimeter cells in the $\eta - \phi$ space around the photon barycenter are not included in the calculation. The small leakage from the photon outside this region, evaluated as a function of photon transverse energy on simulated samples of single photons (thus avoiding additional contributions from the underlying event), is then subtracted from the isolation variable. After this correction, the isolation energy of truly isolated photons is independent of the photon transverse energy.

To reduce uncertainties from underlying event modeling, the isolation is then further corrected using a method suggested in Ref. [22]. Based on the standard seeds for jet reconstruction, which are noise-suppressed three-dimensional topological clusters [8], and for two different pseudorapidity regions ($|\eta| <$ 1.5 and $1.5 < |\eta| < 3.0$), a k_T jet-finding algorithm [23, 24], implemented in `FastJet` [25], is used to reconstruct all jets without any explicit transverse momentum threshold. During reconstruction, each jet is assigned an area via a Voronoi tessellation [26] of the $\eta - \phi$ space. According to the algorithm, every point within a jet's assigned area is closer to the axis of that jet than of any other jet. The transverse energy density for each jet is then computed from the ratio between the jet transverse energy and its area. The ambient transverse energy density for the event, from pileup and underlying event, is taken to be the median jet transverse energy density. Finally, this ambient transverse energy density is multiplied by the area of the isolation cone to compute the correction to the isolation energy.

The estimated ambient transverse energy fluctuates significantly event-by-event, reflecting the fluctuations in the underlying event and pileup activity in the data. The mean correction to the calorimeter transverse energy in a cone of radius $R = 0.4$ for an event with one pp interaction is around 440 MeV in events simulated with `PYTHIA` and 550 MeV in `HERWIG`. In the data, the mean correction is 540 MeV for events containing at least one photon candidate with $E_T > 15$ GeV and exactly one reconstructed primary vertex, and increases by an average of 170 MeV with each additional reconstructed primary vertex. The average number of reconstructed primary vertices for the sample under study is 1.56. For a consistent comparison of this measurement to a theoretical prediction which incorporates an underlying event model, the method described above should be applied to the generated final state in order to evaluate and apply the appropriate event-by-event corrections.

After this correction, the distribution of the isolation variable for direct photons in simulated γ+jet events is centered at zero, with fluctuations that are dominated by electronic noise from the calorimeter measurement. For more details of the isolation calculation, the determination of the correction terms, and the impact of the jet-area corrections on the measured cross section, see Appendix A.

A study was performed in [27] to determine the correspondence between the parton-level and reconstruction-level isolation criteria. The efficiency of a parton-level isolation cut on `PYTHIA` photons originating in a Bremsstrahlung process was compared to the efficiency of the reconstruction-level cut at 3 GeV. Figure 3 shows the efficiency as a function of the isolation cut for such photons. The parton-level cut chosen was that which best matched the efficiency of the reconstruction-level cut at 3 GeV.

The isolation distributions for prompt and fake photon candidates from simulation, as well as the distribution of selected candidates in data, are shown in Figure 4 for reconstructed photon candidates passing the preselection and the loose identification criteria. The signal distribution is separated into two components: true isolated prompt photons ($E_T^{iso} < 4$ GeV), and prompt photons that fail the true isolation cut ($E_T^{iso} > 4$ GeV) described in the Introduction. The true isolation energy E_T^{iso} is determined in the signal MC samples by looping over the MC truth block and computing the total transverse energy of all partons inside a (η, ϕ) cone of radius 0.4 around the photon direction. These figures serve to illustrate the differences in the isolation energy distributions between signal and background in simulation. It's important to note, however, that possible differences between simulated and collision data imply that data-driven models of the isolation energy distributions for both signal and background are critical components of this analysis.

The parton-level isolation was developed to determine whether photons are truly isolated, both for
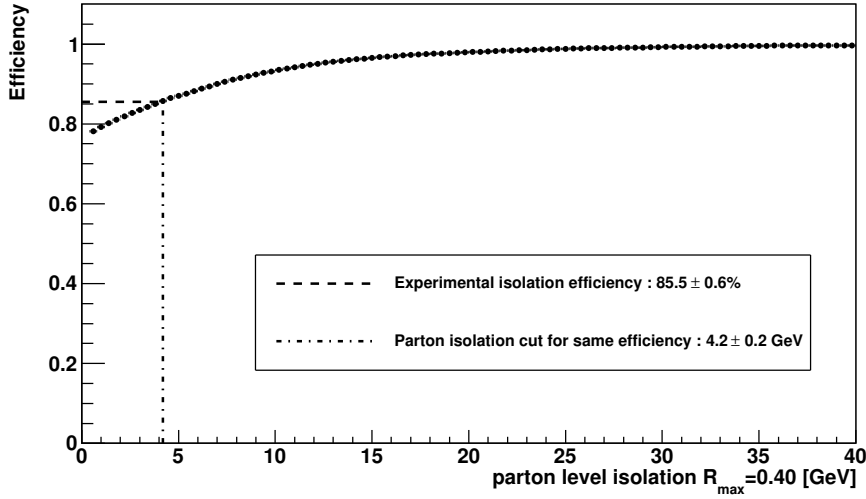
Figure 3: The efficiency as a function of different parton level isolation cuts, with comparison to the experimental isolation efficiency.

relating the experimental isolation cut to a cut in JETPHOX, and for determining the efficiency of the isolation cut for truly isolated photons. However, a parton-level isolation is unmeasureable, so it is more appropriate to determine the true isolation energy after hadronization, and then to correct the theory to account for the effects of hadronization (if necessary). In this case, a cut on the true, particle-level isolation is equivalent to the same cut on the parton-level isolation to within 1% in the efficiency, as long as the cut is within 1 GeV of the nominal cut of 4 GeV. For the specific effects of the parton/particle distinction, see Section 7.5

In the following, all photon candidates having reconstructed isolation energies lower than 3 GeV are considered as experimentally "isolated". This definition has an efficiency which is similar to that from the parton-level isolation cut, as shown in Section 3.2 of Ref. [27]. The small difference between the definition of isolation at the truth and reconstruction levels will be taken into account in the signal reconstruction efficiency (see Section 5).

The criterion that the reconstructed isolation energy be lower than 3 GeV is expected to be around 96% efficient for true isolated prompt photons that pass tight identification criteria, both for photons from the hard-scattering (96.5%) and from fragmentation (95.6%). The criterion is slightly less efficient for photons from parton bremsstrahlung and fragmentation because they have, on average, more nearby hadronic activity that gives rise to the asymmetric positive tail of the prompt photon signal distribution in Figure 4. The same criterion is expected to reject about 50% of background candidates with transverse energy greater than 15 GeV. An isolation "sideband" is defined as the control region containing photon candidates with isolation energies higher than 5 GeV.
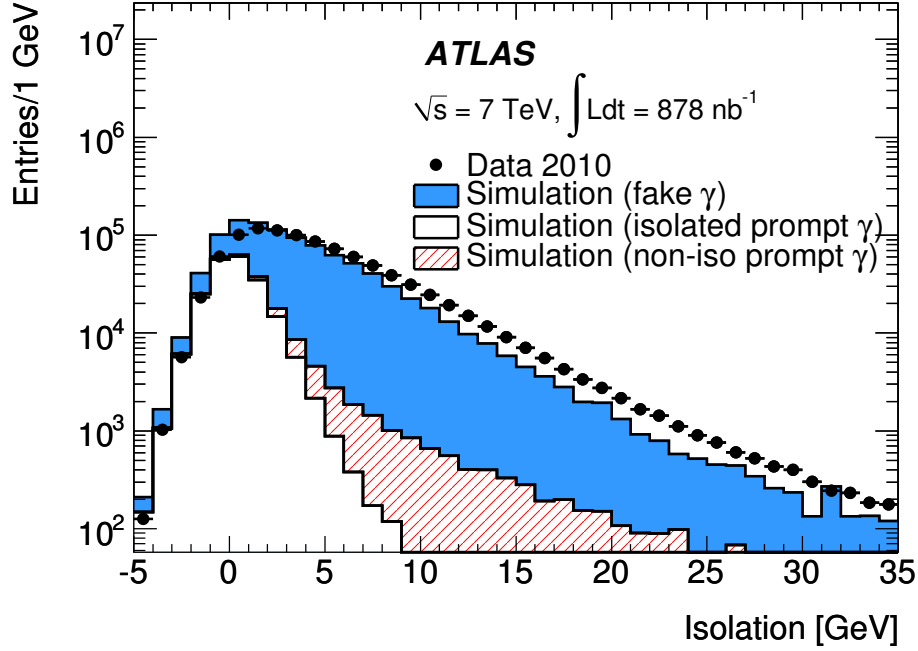
Figure 4: Distribution of the isolation energy of reconstructed photon candidates passing the preselection and the loose identification criteria. The data are represented by dots, the histograms represent the expectations from Monte Carlo simulations for true isolated prompt photons (hollow white histogram), non-isolated (at truth level) prompt photons (hatched red histogram) and fake photon candidates (filled blue histogram). The simulated prompt photon distribution (hollow+hatched histogram) is normalized to the data luminosity using the leading order PYTHIA cross section. The simulated background distribution (filled blue histogram) is normalized such that the sum of fake and prompt photons matches the observed data yield. The width of the isolation distribution for signal is driven by noise in the EM calorimeter, which is calibrated to be centered at zero. The isolation energies for well-isolated signal photons, even after removing any out-of-core leakage, will therefore have a negative component, corresponding to downward fluctuations in the calorimeter cells.

5 Signal efficiency

5.1 Reconstruction efficiency

The reconstruction efficiency is computed as a function of the true photon transverse energy, for a certain bin k of pseudorapidity. It is defined as the ratio between the number of true photons that are reconstructed in the pseudorapidity interval $\eta_{k,1} \leq |\eta^\gamma_{\text{reco}}| < \eta_{k,2}$ (and cluster not overlapping with bad quality calorimeter cells, *i.e.* passing the e/γ object quality criteria), and have experimental isolation energy lower than 3 GeV, and the number of true photons that have true pseudorapidity $\eta_{k,1} \leq |\eta^\gamma_{\text{true}}| < \eta_{k,2}$ and particle-level hadronic isolation lower than 4 GeV:

$$\varepsilon^{\text{reco},k}(E^\gamma_{\text{T,true}}) \equiv \frac{dN^\gamma(\eta_{k,1} \leq |\eta^\gamma_{\text{reco}}| < \eta_{k,2}, E^{\text{iso}}_{\text{T,reco}} < 3 \text{ GeV})/dE^\gamma_{\text{T,true}}}{dN^\gamma(\eta_{k,1} \leq |\eta^\gamma_{\text{true}}| < \eta_{k,2}, E^{\text{iso}}_{\text{T,true}} < 4 \text{ GeV})/dE^\gamma_{\text{T,true}}} \quad (2)$$

The nominal reconstruction efficiencies are calculated by using a luminosity-weighted mixture of direct photons produced in PYTHIA-simulated γ-jet events and fragmentation photons produced in simulated dijet events. The Pythia LO cross sections are used in order to compute the equivalent luminosity of each sample and scale it to a common luminosity. The reconstruction efficiencies as a function of the true photon transverse energy in the three pseudorapidity intervals under study are listed in Table 5. The average inefficiency of the reconstruction algorithms for isolated direct photons with true $15 \leq E_{\text{T}} < 100$ GeV and $|\eta| < 1.81$ is around 3-4%, dominated by the inefficiency at low E_{T}; the acceptance loss due to the dead calorimeter cells and the inefficiency of the object quality requirements is around 11%, and the inefficiency of the experimental isolation requirement is around 3-4% in the first two $|\eta|$ bins and around 11% in the pseudorapidity interval between 1.52 and 1.81.

Table 5: Isolated prompt photon reconstruction efficiency $\varepsilon^{\text{reco}}_k(E^\gamma_{\text{T}})$, defined as the ratio between the number of true prompt photons reconstructed in a certain interval k of pseudorapidity, passing e/γ object quality criteria and with reconstructed isolation energy lower than 3 GeV, and the number of true prompt photons that have true pseudorapidity in the same interval k and true parton-level hadronic isolation lower than 4 GeV. Statistical uncertainties are lower than 1.0% and are much lower than systematic uncertainties.

E_{T} min [GeV]	E_{T} max [GeV]	$0.00 \leq |\eta^\gamma| < 0.60$ [%]	$0.60 \leq |\eta^\gamma| < 1.37$ [%]	$1.52 \leq |\eta^\gamma| < 1.81$ [%]
15.0	20.0	83.1	83.5	79.2
20.0	25.0	83.7	84.4	78.7
25.0	30.0	84.2	84.7	78.8
30.0	35.0	84.3	85.1	78.5
35.0	40.0	84.3	84.2	78.2
40.0	50.0	84.1	83.9	76.3
50.0	60.0	83.5	83.7	76.1
60.0	100.0	83.9	82.7	73.8

The corresponding distributions, separately for direct and fragmentation photons, are shown in Figure 5.

The uncertainty on the nominal reconstruction efficiency originating from the difference between the efficiency for direct and fragmentation photons, and the unknown ratio of the two in the final sample of selected signal photons, is taken into account as a source of systematic uncertainty for the measured cross-section as described in Section 8.3.
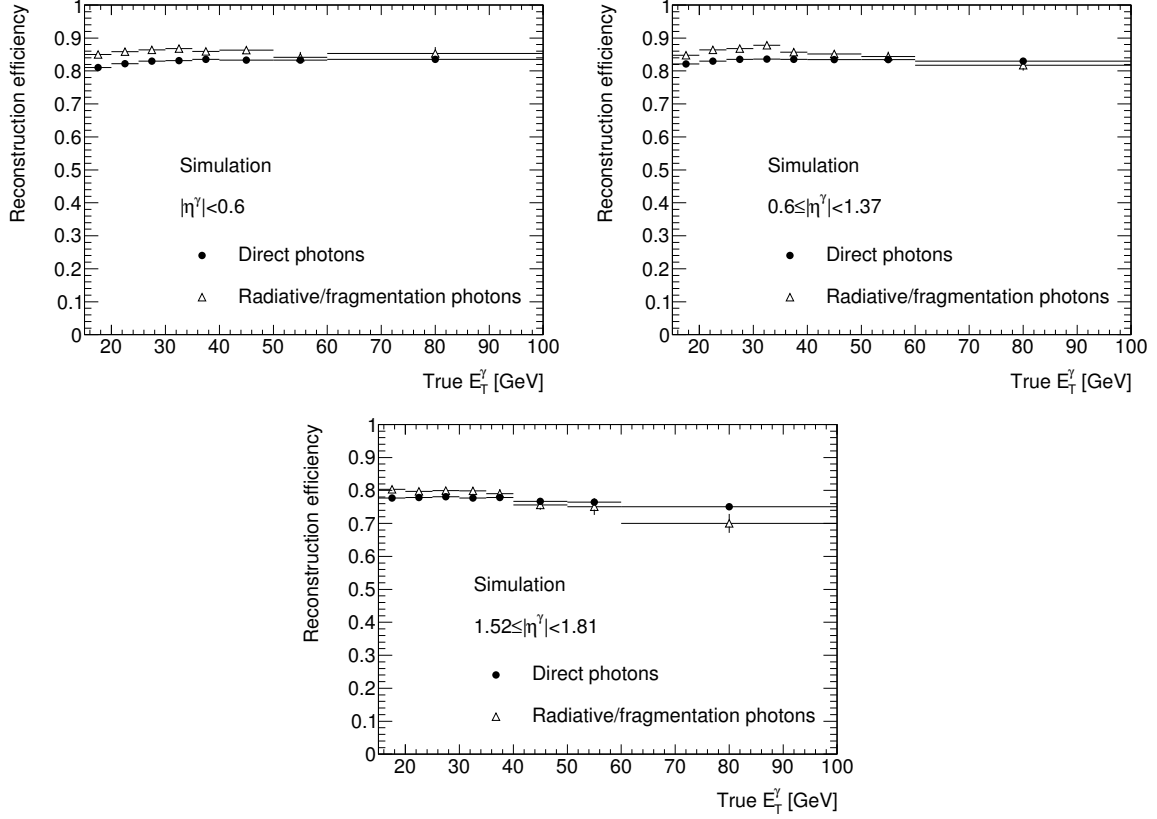
Figure 5: Reconstruction efficiency as a function of the true photon transverse energy. Top left: $|\eta^\gamma| < 0.6$. Top right: $0.6 \leq |\eta^\gamma| < 1.37$. Bottom left: $1.52 \leq |\eta^\gamma| < 1.81$.

The efficiency of the reconstructed transverse energy requirement (the efficiency of selecting true photons between 15 and 100 GeV when requiring a reconstructed transverse energy between 15 and 100 GeV) will be discussed in Section 7 in the context of the unfolding of the differential E_T spectrum of the selected prompt photon candidates.

5.2 Offline selection efficiency

The offline photon selection efficiency is computed as a function of the reconstructed photon transverse energy and for a certain bin k of pseudorapidity. It is defined as the efficiency for reconstructed true prompt photons, with reconstructed η in the pseudorapidity bin k and reconstructed isolation lower than 3 GeV, to pass the tight photon identification (tight-ID) criteria described in Section 4.3:

$$\varepsilon^{\mathrm{offl},k}(E^\gamma_{\mathrm{T,reco}}) \equiv \frac{dN^\gamma(\eta_{k,1} \leq |\eta^\gamma_{\mathrm{reco}}| < \eta_{k,2}, E^{\mathrm{iso}}_{\mathrm{T,reco}} < 3 \text{ GeV}, \text{tight} - \text{ID})/dE^\gamma_{\mathrm{T,reco}}}{dN^\gamma(\eta_{k,1} \leq |\eta^\gamma_{\mathrm{reco}}| < \eta_{k,2}, E^{\mathrm{iso}}_{\mathrm{T,reco}} < 3 \text{ GeV})/dE^\gamma_{\mathrm{T,reco}}} \tag{3}$$

The efficiencies are calculated using MC samples of prompt photons. The shower-shape variables of the simulated photons are adjusted by the observed differences between simulation and data, as described in [20]. The differences are often small, except in cases where the differences between data and MC are significant, as is seen in the lateral shower-shape variables in the second sampling. The efficiency in data is then taken as the efficiency for the modified MC photons to pass the tight shower-shape cuts.

As a cross-check of the MC-based efficiencies, electrons from W decays in collision data are used to compute a data-driven estimate of the efficiency for photons. The electrons are selected without making

any shower-shape selection cuts, relying on E_T^{miss} and kinematic constraints to produce a clean sample. The efficiencies of converted photons are taken from the efficiency for selected electrons to pass the tight photon selection criteria. For unconverted photons, the shower shape distributions measured for electrons in data are corrected for shifts – determined using simulated electron and unconverted photon samples – that take into account the differences between electron and unconverted photon clusters. Both methods are described below, with further information available in [20].

5.2.1 Shower Shape Correction Method

Shower-shape corrections are derived as described in section 4.3.3, and are used to modify the showers of photon candidates in simulation. The efficiency of reconstructed and isolated photon candidates to pass the robust tight cuts is then measured directly with simulated photons. The robust tight cuts reduce the uncertainties of this approach to the percent level in all η regions except for the outer endcap; in that region, the `g10_loose` trigger applied cuts that were too tight for all runs up to period E3. This inefficiency is unrecoverable for those data, which corresponds to over half of the integrated luminosity used in this analysis. This loss of efficiency, and the corresponding large uncertainties on the final estimated efficiency in that region, led to the decision to exclude $|\eta| > 1.81$ from the final measurement.

5.2.2 Electron Extrapolation Method

The electrons used to estimate the photon efficiency are selected from $W \rightarrow e\nu$ decays, with the following criteria:

- The event must fire the L1_EM14 trigger.

- There must be at least one isolated offline electron candidate with $E_T > 20$ GeV.

- The offline calorimeter based E_T^{miss} must be larger than 25 GeV,

- The calorimeter-based E_T^{miss} must be separated in ϕ from any objects (electrons or jets) with $E_T > 15$ GeV by at least 2.5 radians

- For low p_T electron candidates ($20 < E_T < 30$ [GeV]), the electron must pass all electron track-based identification criteria (i.e. E/p, TRT high threshold hits, and track/cluster matching)

For converted photons, the efficiency of the probe electrons to pass the tight photon selection criteria is taken as the efficiency of converted photons in data.

For unconverted photons, a combination of electrons from simulation, photons from simulation, and electrons in collision events are used to estimate the efficiencies. Shower-shape shifts for the electrons are derived from the differences between electrons and unconverted photons in simulation. The efficiency for unconverted photons in data is then estimated based on the efficiency for the shower-shape-shifted electrons in data.

5.2.3 Results

The offline efficiencies are determined after the shower shape corrections, and are listed in Table 6 as a function of the reconstructed photon transverse energy in the three pseudorapidity intervals under study. The corresponding distributions are shown in Figure 6.

The final systematic uncertainties on the reconstruction and identification efficiency, *excluding* those due to the electron-extrapolation results, are listed in table 7. A more complete description of the systematic uncertainties associated with this method is given in section 8.3, and in [20].

Table 6: Isolated prompt photon selection efficiency $\varepsilon_k^{\text{offl}}(E_T^\gamma)$, defined as the fraction of true prompt photons reconstructed in a certain interval k of pseudorapidity, passing e/γ object quality criteria, with reconstructed isolation energy lower than 3 GeV, that pass tight photon identification criteria.

E_T min [GeV]	E_T max [GeV]	$0.00 \leq |\eta^\gamma| < 0.60$ [%]	$0.60 \leq |\eta^\gamma| < 1.37$ [%]	$1.52 \leq |\eta^\gamma| < 1.81$ [%]
15.0	20.0	63.3	63.5	72.2
20.0	25.0	73.5	73.5	81.6
25.0	30.0	80.2	80.8	86.7
30.0	35.0	85.5	85.3	90.4
35.0	40.0	85.2	89.3	92.3
40.0	50.0	89.2	92.1	93.5
50.0	60.0	91.3	94.1	93.9
60.0	100.0	92.2	94.8	94.2

Table 7: Total systematic uncertainties on the reconstruction+offline selection efficiency, excluding the systematics associated with the comparison of the nominal results with those of the electron extrapolation method.

E_T min [GeV]	E_T max [GeV]	$0.00 \leq |\eta^\gamma| < 0.60$ [%]	$0.60 \leq |\eta^\gamma| < 1.37$ [%]	$1.52 \leq |\eta^\gamma| < 1.81$ [%]
15.0	20.0	7.6	7.9	9.4
20.0	25.0	6.3	7.0	8.7
25.0	30.0	5.6	5.9	6.9
30.0	35.0	4.8	5.0	6.1
35.0	40.0	4.4	4.8	5.4
40.0	50.0	3.8	4.1	5.2
50.0	60.0	3.2	2.9	5.0
60.0	100.0	2.8	2.8	4.3

The results of the electron extrapolations are shown in Figure 7 for converted photons, and in Figure 8 for unconverted photons. The observed efficiencies are consistent with the efficiencies estimated using the shower-shape correction method with simulated photons, within the statistical and systematic uncertainties on the methods.

5.3   Trigger marginal efficiency

The efficiency of the calorimeter trigger, relative to the photon reconstruction and offline selection, is defined as the probability of a true prompt photon to pass the `g10_loose` trigger selection, where the true prompt photon is reconstructed with experimental isolation lower than 3 GeV and passes tight photon identification criteria.

$$\varepsilon^{\text{trig},k}(E_{T,\text{reco}}^\gamma) \equiv \frac{dN^\gamma(\eta_{k,1} \leq |\eta_{\text{reco}}^\gamma| < \eta_{k,2}, E_{T,\text{reco}}^{\text{iso}} < 3 \text{ GeV}, \text{tight} - \text{ID}, \text{trigger})/dE_{T,\text{reco}}^\gamma}{dN^\gamma(\eta_{k,1} \leq |\eta_{\text{reco}}^\gamma| < \eta_{k,2}, E_{T,\text{reco}}^{\text{iso}} < 3 \text{ GeV}, \text{tight} - \text{ID})/dE_{T,\text{reco}}^\gamma} \tag{4}$$

The efficiency is estimated in two steps. First, using a prescaled sample of minimum bias triggers, the efficiency of a lower (≈ 3.5 GeV) threshold L1 calorimeter trigger (`L1_EM2`) is determined. The measured
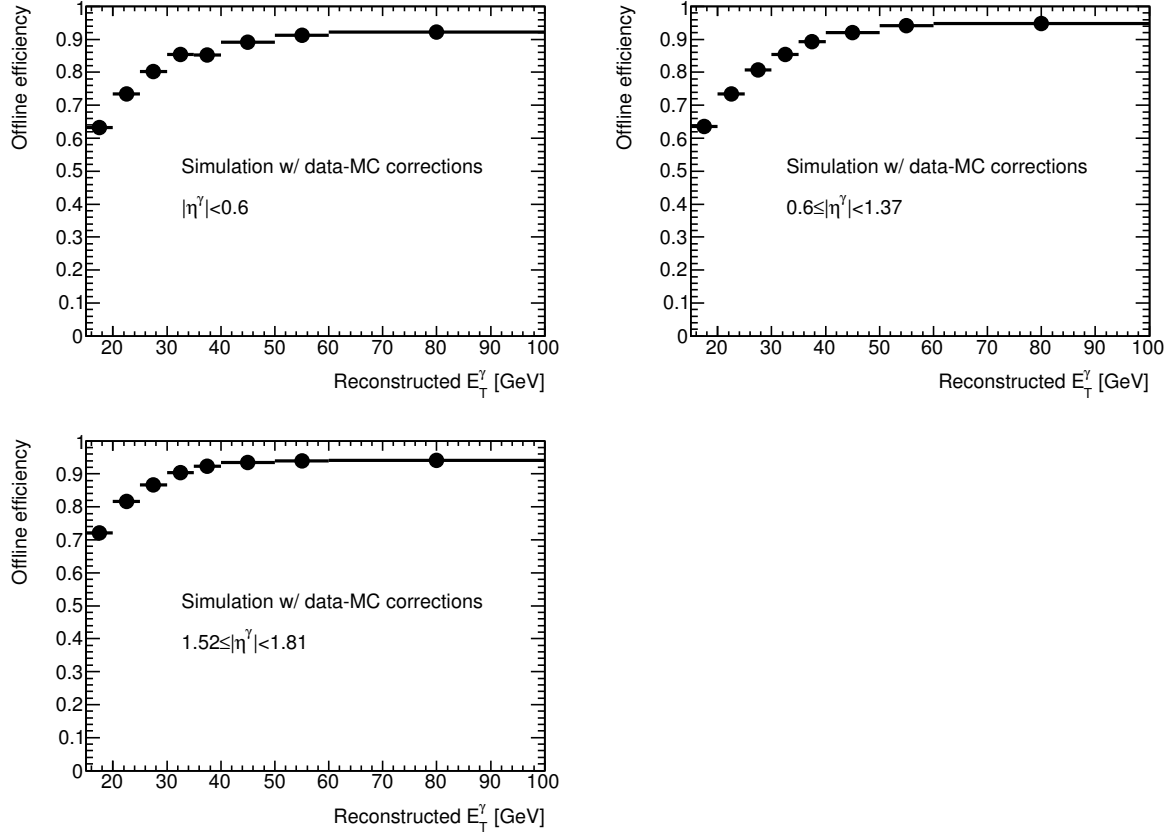
Figure 6: Offline selection efficiency as a function of the reconstructed photon transverse energy for prompt photons with reconstructed isolation energy lower than 3 GeV. Top left: $|\eta^\gamma| < 0.6$. Top right: $0.6 \le |\eta^\gamma| < 1.37$. Bottom left: $1.52 \le |\eta^\gamma| < 1.81$.

efficiency of L1_EM2 is 100% for all photon candidates with reconstructed E_T above 15 GeV passing tight identification criteria. Then, the efficiency of the trigger used in this analysis (the g10_loose, with nominal E_T threshold set to 10 GeV in the high-level trigger and at 5 GeV in the underlying level-1 trigger) is measured using the sample of events that pass the L1 calorimeter trigger with a 3.5 GeV threshold. The efficiencies with respect to the offline selection are computed for reconstructed photon candidates passing the tight identification criteria and with isolation energy below 3 GeV as a function of the transverse energy. The results are shown in Figure 9.

The trigger efficiencies for transverse energies above 15 GeV are summarized also in Table 8, for tight isolated photon candidates reconstructed within a cone of radius 0.15 centered on a trigger cell that has triggered the g10_loose selection. They are found to be consistent with the value

$$\varepsilon^{\text{trig}} = 99.5\%$$ (5)

in all the pseudorapidity intervals under study. This is the value used in the measurement.

Monte Carlo samples are used to check the possible bias introduced by using photon candidates from data, which are a mixture of prompt and fake photons instead of only prompt photons. This bias, obtained from the absolute difference of the trigger efficiency for pure signal simulated samples and a pure background simulated sample, is found to be smaller 0.5% for tight photon candidates (see Table 9) above 15 GeV. A comparison between the high-level trigger efficiency in data and in the mixture of signal and background predicted by the simulation is shown in Figure 10.
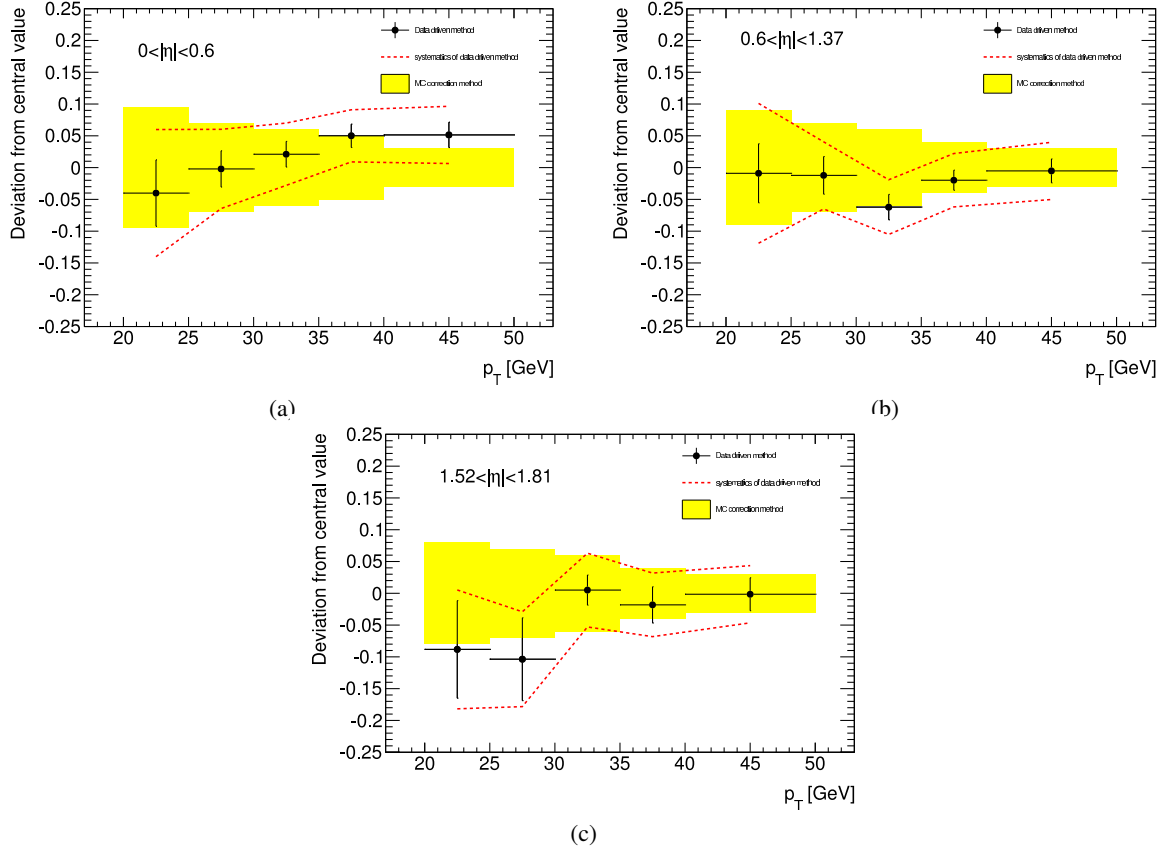
Figure 7: Comparison between the predicted converted photons efficiencies from electrons and the nominal modified tight efficiency for converted photons. The yellow bands account for the sum of the systematic errors. The errors on the black points are statistical only, while the red lines represent the quadratic sum of statistical and systematic errors on the efficiency extrapolated from the *W* electrons.
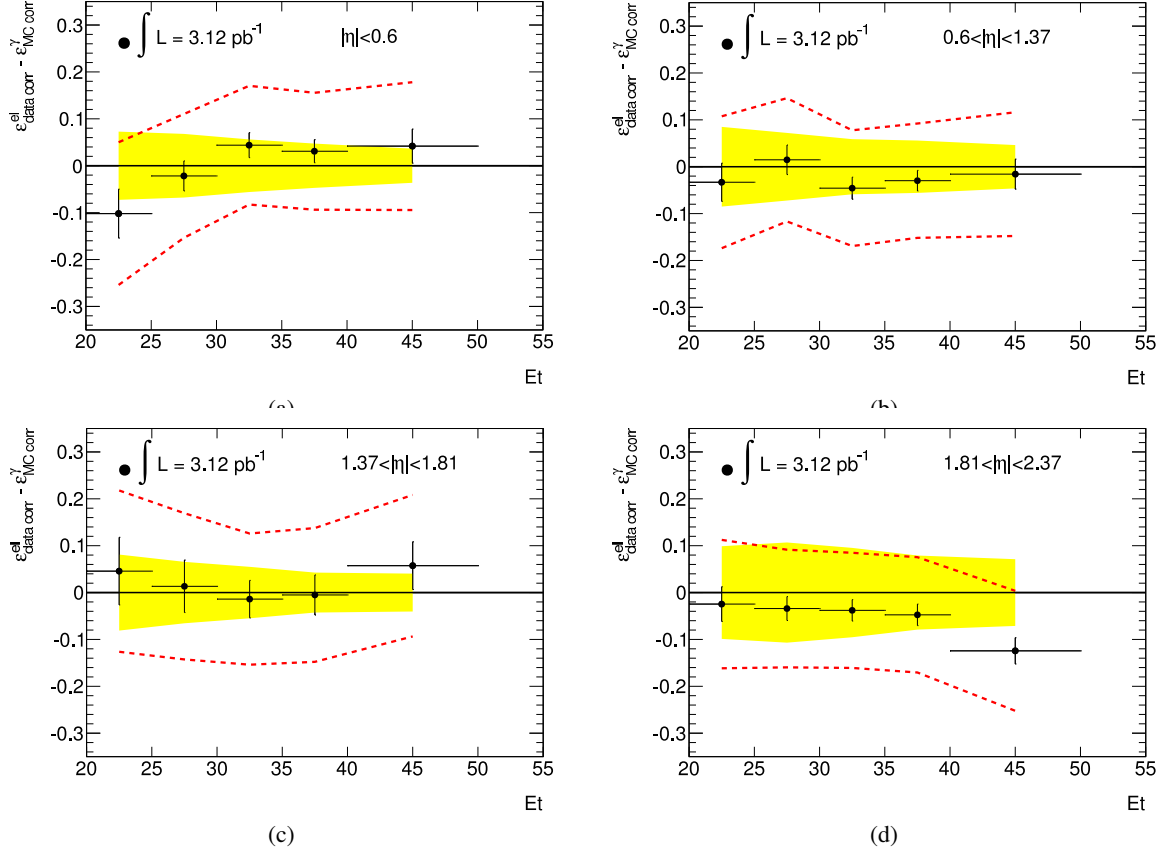
Figure 8: Comparison between the predicted unconverted photons efficiencies from electrons and the nominal modified tight efficiency for unconverted photons. The yellow bands are determined from the sum of the systematic errors. The errors on the black points are statistical only, while the red lines represent the quadratic sum of statistical and systematic errors.
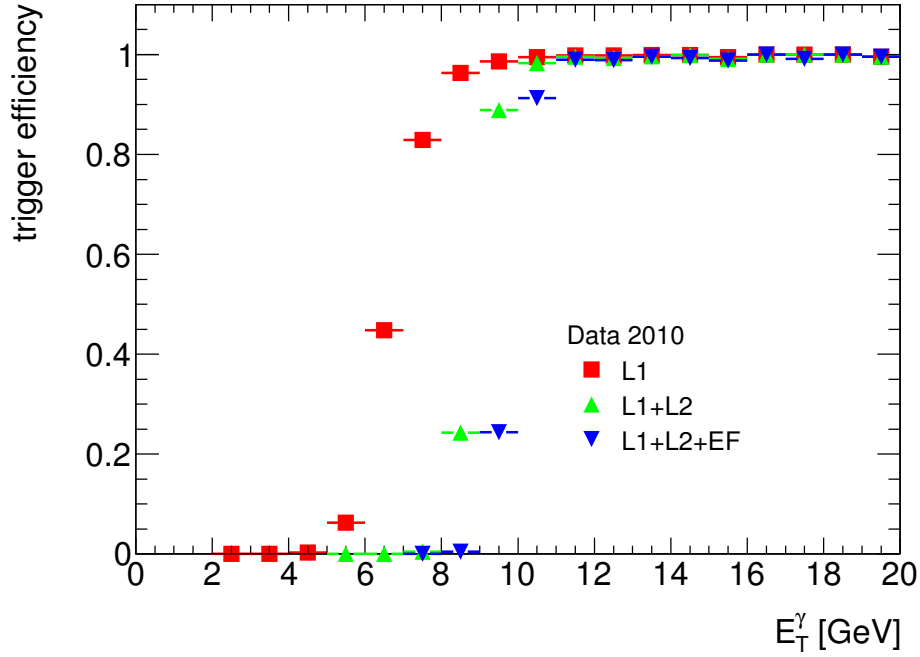
Figure 9: Photon trigger efficiency with respect to the offline photon selection as measured in data for the three levels of the `g10_loose` trigger chain, on photon candidates passing the tight identification criteria and with isolation energy lower than 3 GeV.

Table 8: Trigger efficiency with respect to the offline photon selection for photons with transverse energies greater than 15 GeV, as determined in data for the three levels of the `g10_loose` trigger chain. Only the statistical uncertainty is quoted. The systematic uncertainty is estimated to be 0.5% for tight photon candidates.

$|\eta|$ interval	$0.0 \leq |\eta| < 0.6$	$0.6 \leq |\eta| < 1.37$	$1.52 \leq |\eta| < 1.8$	$1.8 \leq |\eta| < 2.37$	All
Efficiency (L1) [%]	100.00±0.00	99.92±0.08	99.62±0.27	99.84±0.16	99.87±0.06
Efficiency (L2) [%]	100.00±0.00	99.83±0.12	99.62±0.27	99.68±0.22	99.81±0.08
Efficiency (EF) [%]	99.88±0.12	99.32±0.24	99.42±0.27	99.52±0.27	99.53±0.11

Table 9: Trigger efficiency with respect to the offline photon selection for photons with transverse energies greater than 15 GeV, as determined on simulated samples of direct, fragmentation and fake photons.

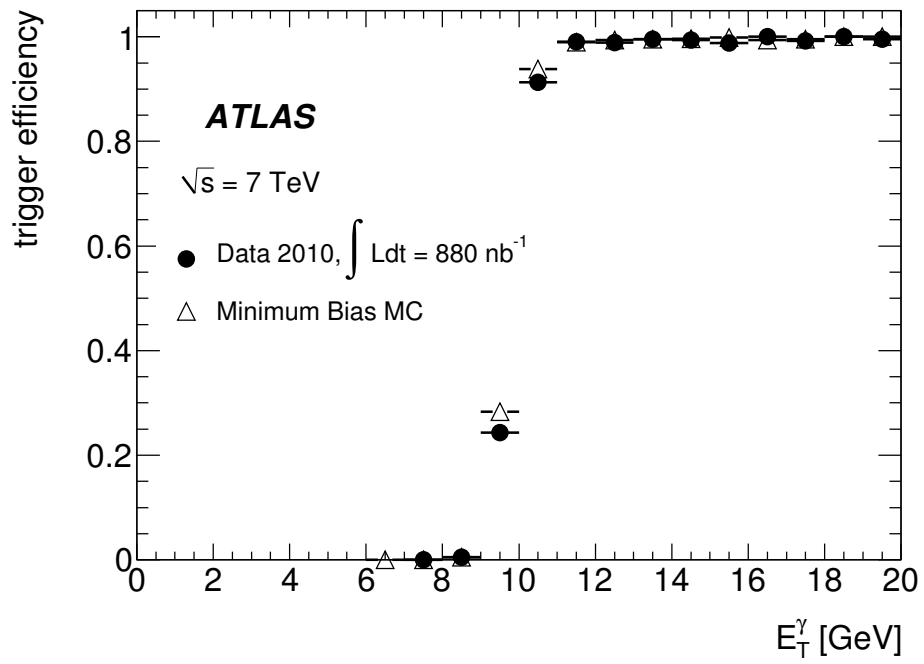| $|\eta|$ interval	$0.0 \leq |\eta| < 0.6$	$0.6 \leq |\eta| < 1.37$	$1.52 \leq |\eta| < 1.8$	$1.8 \leq |\eta| < 2.37$	All
Efficiency (direct γ)[%]	99.69±0.13	99.87±0.07	100.00±0.00	100.00±0.00	99.87±0.04
Efficiency (frag γ) [%]	99.62±0.38	100.00±0.00	100.00±0.00	100.00±0.00	99.90±0.10
Efficiency (fake γ) [%]	99.59±0.21	99.70±0.13	99.69±0.22	99.88±0.12	99.71±0.08

Figure 10: Photon trigger efficiency with respect to the offline photon selection, as measured in data (circles) and simulated background events (triangles) on photon candidates passing the tight identification criteria and with isolation energy lower than 3 GeV.

6 Background estimation

The photon identification strategy outlined in section 4 is optimized to provide a high efficiency for signal photons, for all relevant regions of η and across a large range of E_T, while rejecting a substantial fraction of the background. These selection criteria, however, do not reject *all* background. Thus, some estimate of the residual background left in the collection of signal candidates is necessary to properly compute the cross section.

Two methods have been developed to estimate the purity, P, of the signal candidates. Both of these methods rely relatively little on Monte Carlo models of the signal or background, instead deriving the relevant distributions from data, and using simulation only for second-order corrections to the results. In addition, both methods use a measurement of the isolation of the photon candidate to help determine the background contribution; the definition of isolation is described in more detail in section 4. Brief summaries of each method are provided below; for further details, see Ref. [11].

6.1 Extraction of the Isolation Distribution of the Background from Data

Both background subtraction techniques rely on a measurement of isolation. While the isolation for signal photons may be relatively well understood in simulation, it is generally not safe to rely on Monte Carlo generators to estimate the isolation distribution of the background. Therefore, the background isolation distribution is extracted directly from data by reversing several photon identification cuts. The specific choice of cuts to reverse is constrained by two requirements: the isolation distribution of the extracted background should be unbiased with respect to the background that passes the tight selection criteria, and the number of candidates in the extracted background sample should be sufficient to avoid large statistical variations, which may adversely impact the fit.

The variables which use the first sampling of the EM calorimeter are defined over a relatively small region at the core of the cluster excluded from the isolation measurement, which implies that they should not be strongly correlated with isolation. Two cuts in particular, F_{side} and $w_{s\,3}$, are defined over a particularly narrow range of strips, and are ideal choices for the reverse-cuts procedure. Two additional cuts (ΔE and E_{ratio}) have also been found to be relatively uncorrelated with isolation, and are also reversed. (The final strip cut, $w_{s\,tot}$, is defined over a wider range of strips, and in simulation was seen to be more strongly correlated with isolation.) In this analysis, a photon candidate need only fail one cut to satisfy the reverse-cuts procedure, but may fail any combination of the cuts being reversed.

6.2 Two-Dimensional Sideband Technique

The first technique for measuring the photon purity was also employed in [28], and uses a two-dimensional sideband (or ABCD) method, where three background control regions are used to estimate the amount of background in the signal region. In this case, the two dimensions are defined by isolation on one axis, and the "tightness" of the photon candidate on the other axis. The isolation axis is split into three bins, of which two are used in the measurement: a non-isolated bin (isolation > 5 GeV) and an isolated bin (isolation < 3 GeV). The intermediate region (3 < isolation < 5 GeV) is ignored. The second axis has only two bins: a bin with photon candidates that pass all of the tight selection criteria, and a bin for photons which fail the tight criteria, but pass the reverse-cuts criteria described above. There are thus three background-like regions and one signal-like region, each with some number of reconstructed candidates:

- N_A, the number of candidates that pass both the tight selection and the isolation cut (signal-like region)

- N_B, the number of candidates that pass the tight selection criteria, but are non-isolated

- N_C, the number of candidates that fail the tight selection criteria, but pass the isolation cut

- N_D, the number of candidates that fail the selection criteria and are non-isolated

An illustration of this two-dimensional plane is shown in Fig. 11. The method then makes the following two assumptions:

- The signal contamination in the three background regions is negligible

- The ratio of isolated to non-isolated background candidates in the non-tight bin $\left(\frac{N_D^{\mathrm{bkg}}}{N_C^{\mathrm{bkg}}}\right)$ is equal to the same ratio in the tight bin $\left(\frac{N_B^{\mathrm{bkg}}}{N_A^{\mathrm{bkg}}}\right)$.
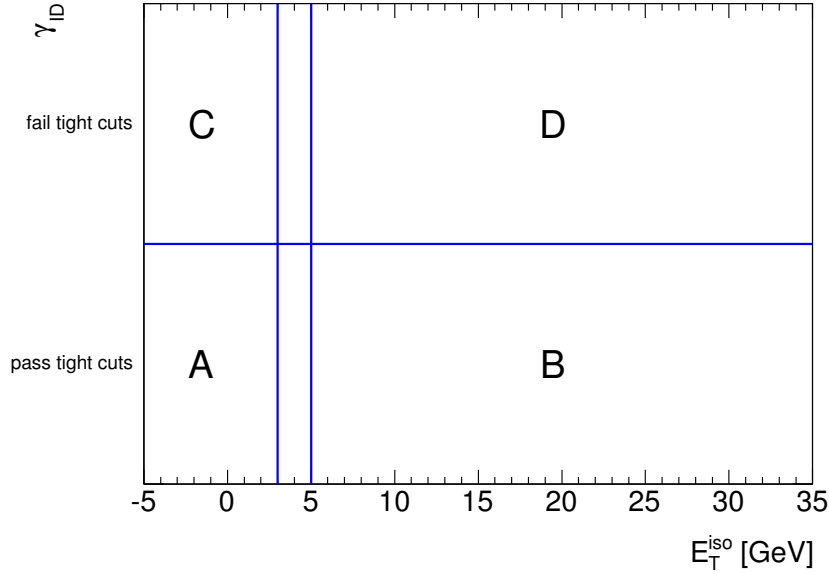

Figure 11: Illustration of the two-dimensional plane, defined by means of the isolation and a subset of the photon identification (ID) variables, used for estimating, from the observed yields N_B, N_C and N_D in the three control regions, the background yield in the signal region where the observed total yield is N_A.

Assuming that these assumptions hold, it then follows that the signal yield (N_A^{sig}) and purity (P) can be calculated with only those four numbers:

$$N_A^{\mathrm{sig}} = N_A - N_B \frac{N_C}{N_D} \tag{6}$$

$$P = 1 - \frac{N_B}{N_A} \frac{N_C}{N_D} \tag{7}$$

The assumption that the signal contamination in the background control regions is small is checked using the prompt photon Monte Carlo sample. As the signal leakage is always positive and non-zero, corrections are applied to limit its effects on the final result. The details of the corrections are described in [11], and are typically less than 5%.

The second assumption, that the isolation distribution of the background is not correlated with the reverse-cuts procedure, is harder to estimate. Monte Carlo samples have been used to extract the bias on

the purity introduced by the background, which in [28] was then used to correct the final result. However, in this analysis, which has a finer binning in transverse energy, the size of the simulated samples is not sufficient to extract meaningful corrections over the large statistical fluctuations. Therefore, the bias extracted from simulation is used to compute systematic errors on the final purities, but is not used to correct the central values.

To account for both effects, the purity equation would become:

$$N_A^{\text{sig}} \quad = \quad N_A - N_A^{\text{bkg}} = N_A - R^{\text{bkg}} \frac{(N_B - N_B^{\text{sig}})(N_C - N_C^{\text{sig}})}{N_D - N_D^{\text{sig}}} \tag{8}$$

$$= \quad N_A - R^{\text{bkg}} \frac{(N_B - c_B N_A^{\text{sig}})(N_C - c_C N_A^{\text{sig}})}{N_D - c_D N_A^{\text{sig}}}, \tag{9}$$

to be solved for the signal yield N_A^{sig}. Here $R^{\text{bkg}} = \frac{N_A^{\text{bkg}} N_D^{\text{bkg}}}{N_B^{\text{bkg}} N_C^{\text{bkg}}}$ and $c_X = \frac{N_X^{\text{sig}}}{N_A^{\text{sig}}}$, $X = (B, C, D)$. In the following analysis we set $R^{\text{bkg}} = 1$ (which correspond to neglecting correlations in background events between the isolation and the shower shape quantities used to define the 2D plane) while the values of c_B, c_C, c_D are taken from the simulated signal samples (see Ref. [11]).

6.3 Isolation Template Technique

The second technique relies on the same model of the background as the two-dimensional sideband method, but it also introduces a signal template. The tight photon sample is then fit to a sum of the signal and background templates, from which the signal yield and purity can be extracted. This is similar to the technique employed in [7], but relies less on simulation for models of signal and background.

Electrons from W and Z decays are used to construct the signal template. These electrons are selected using the standard selection criteria described in [19]. A single template is constructed for each region in $|\eta|$, exploiting the invariance of the corrected isolation in E_T to maximize the available statistics. [4] While these electrons have an isolation profile that, in simulation, is often very similar to that of signal photons, there can be some differences between the two, especially in regions where there is significant material upstream of the calorimeter. A simple shift of the signal template is applied to the electron distributions extracted from collision data to compensate for the differences between electrons and photons seen in MC. This shift is $|\eta|$ dependent, and ranges from 100 MeV (in the central barrel) to 600 MeV (in the endcap).

The background template is extracted from data for each (E_T, $|\eta|$) bin, using the same reverse-cuts procedure as in the 2-D sideband technique. An extended maximum-likelihood fit is then performed with RooFit in each bin, using the isolation histograms as the templates. This method has the advantage that it explicitly handles any overflow of the signal into the non-isolated region, but it still is sensitive to signal which leaks into the reverse-cuts background template. A correction based on Monte Carlo is applied to the final purity results to account for this effect. An example of template fit to the photon candidates selected in the simulation, for $0 \leq |\eta| < .6$ and $40 \leq E_T < 50$ GeV, is shown in Fig. 12. An example of template fit to the photon candidates selected in data, in the same pseudorapidity and transverse energy interval, is shown in Fig. 13.

---

[4]In data, there are some signs that the isolation corrections do not fully remove the E_T dependence for truly isolated objects; however, the effects of any lingering E_T dependence on the final purity measurement have been found to be small.
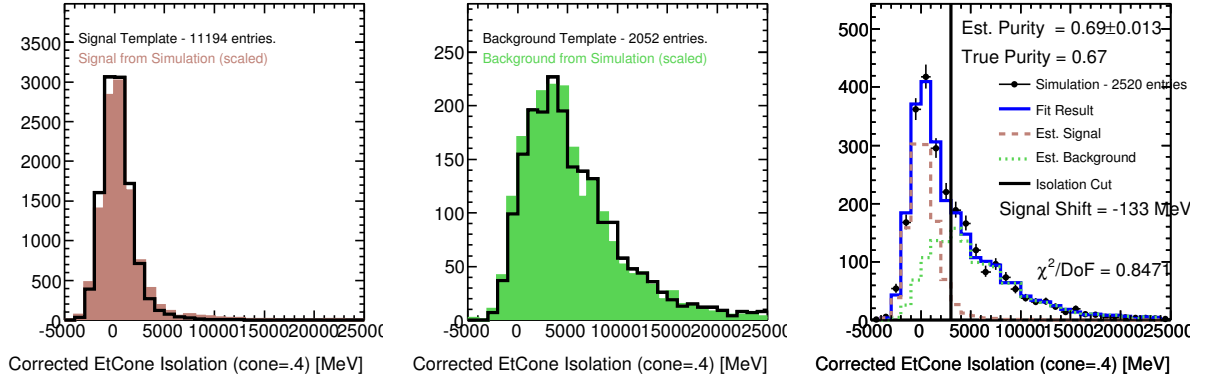
Figure 12: A sample of the purity fit using the isolation template technique in the region $0 \le |\eta| < .6$ and $40 \le E_T < 50$ GeV with simulated events. The left plot shows the signal template (from electrons) overlaid with the true signal in the test sample; the central plot shows the extracted background distribution (from reversing shower shape cuts) overlaid with the true background in the test sample; and the right plot shows the result of the fit in blue, overlaid with the input distribution in black. In this case, the estimated purity agrees with the true purity within the statistical uncertainty on the fit.
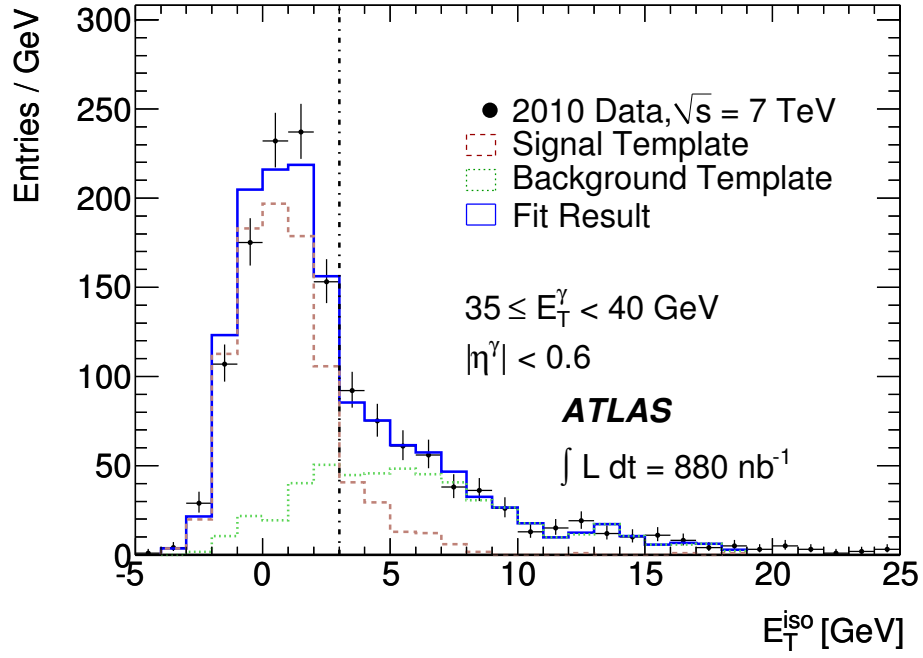
Figure 13: A sample of the purity fit using the isolation template technique in the region $0 \le |\eta| < .6$ and $40 \le E_T < 50$ GeV with real data. The signal template is derived from electrons selected as the products of W or Z decays, and is shown in red. The background template is derived from reversing shower shape cuts, and is shown in green. Both distributions are shown scaled to their estimated contribution in data, derived from the fit.

6.4 Results

6.4.1 Results from the 2D sideband method

The isolated prompt photon purity measured, with the 2D sideband method, as a function of the photon reconstructed transverse energy, is shown in Figure 14. The purity and the estimated signal yield in each pseudorapidity and E_T bin are also summarized in Tables 10-12. Both Figure 14 and Tables 10-12 include also the systematic uncertainties on the measured purity and signal yields. The evaluation of these uncertainties is described in detail in the next subsection.
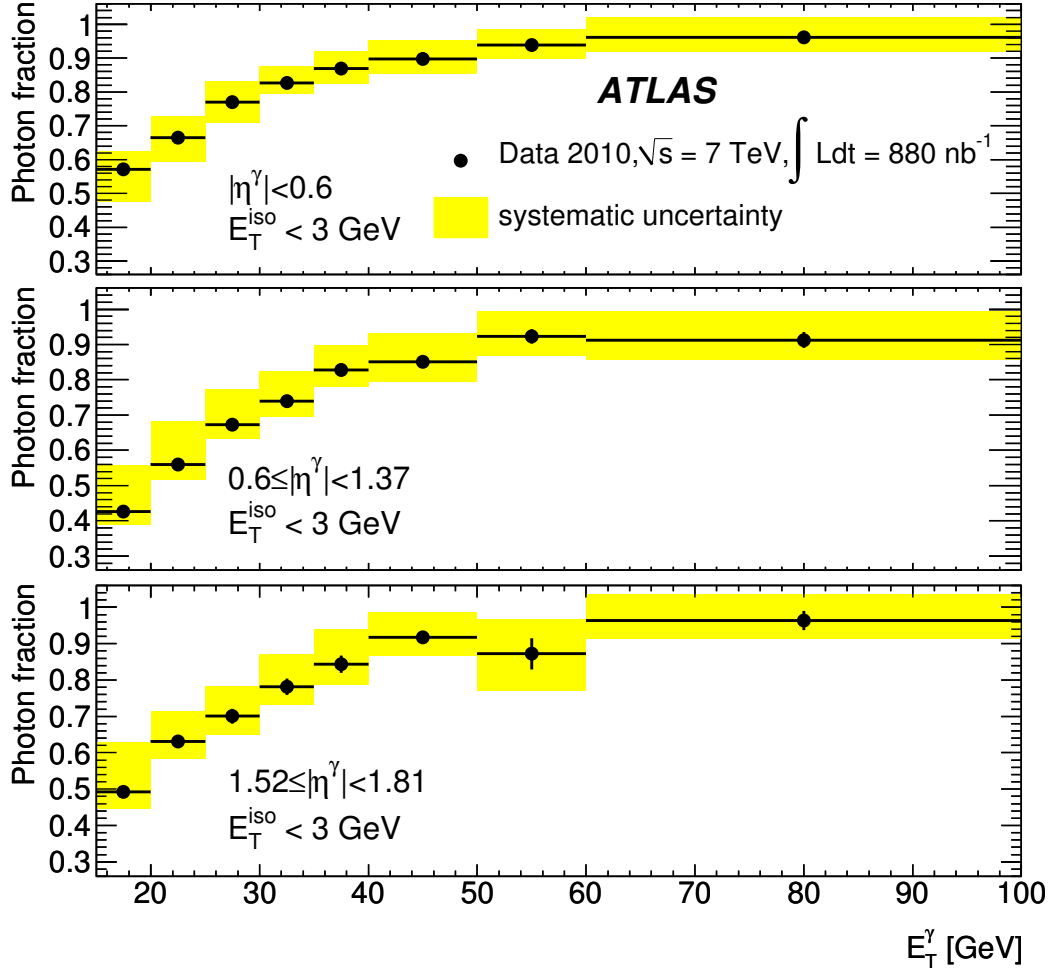

Figure 14: Fraction of isolated prompt photons as a function of the photon transverse energy, as obtained with the 2D sideband method.

Table 10: Observed signal yields and purities as obtained from the 2D sideband counting method. Photons are required to be reconstructed in the pseudorapidity range $0.00 \leq |\eta^\gamma| < 0.60$. The statistical uncertainty on the signal yield includes the contribution from Poisson fluctuations

E_T min [GeV]	E_T max [GeV]	N_{sig}	stat	syst	P [%]	stat [%]	syst [%]
15.0	20.0	11964	±254	$^{+1180}_{-1979}$	57.1	±1.0	$^{+5.6}_{-9.5}$
20.0	25.0	5014	±125	$^{+468}_{-530}$	66.5	±1.2	$^{+6.2}_{-7.1}$
25.0	30.0	2577	±73	$^{+202}_{-205}$	76.9	±1.2	$^{+6.1}_{-6.1}$
30.0	35.0	1461	±50	$^{+88}_{-57}$	82.7	±1.4	$^{+5.0}_{-3.2}$
35.0	40.0	815	±35	$^{+49}_{-41}$	86.9	±1.5	$^{+5.3}_{-4.4}$
40.0	50.0	767	±33	$^{+49}_{-37}$	89.7	±1.4	$^{+5.7}_{-4.2}$
50.0	60.0	329	±20	$^{+17}_{-14}$	93.8	±1.6	$^{+4.8}_{-3.9}$
60.0	100.0	329	±20	$^{+19}_{-15}$	96.2	±1.7	$^{+5.7}_{-4.4}$

Table 11: Observed signal yields and purities as obtained from the 2D sideband counting method. Photons are required to be reconstructed in the pseudorapidity range $0.60 \leq |\eta^\gamma| < 1.37$. The statistical uncertainty on the signal yield includes the contribution from Poisson fluctuations

E_T min [GeV]	E_T max [GeV]	N_{sig}	stat	syst	P [%]	stat [%]	syst [%]
15.0	20.0	12989	±395	$^{+4017}_{-1079}$	42.7	±1.2	$^{+13.1}_{-3.6}$
20.0	25.0	5782	±175	$^{+1252}_{-453}$	55.9	±1.4	$^{+12.2}_{-4.3}$
25.0	30.0	3057	±98	$^{+459}_{-180}$	67.3	±1.5	$^{+10.1}_{-4.0}$
30.0	35.0	1605	±63	$^{+188}_{-94}$	73.9	±1.8	$^{+8.6}_{-4.3}$
35.0	40.0	1024	±43	$^{+86}_{-59}$	82.8	±1.9	$^{+7.0}_{-4.7}$
40.0	50.0	982	±41	$^{+93}_{-67}$	85.2	±1.8	$^{+8.0}_{-5.9}$
50.0	60.0	420	±24	$^{+33}_{-25}$	92.3	±2.0	$^{+7.1}_{-5.5}$
60.0	100.0	373	±23	$^{+34}_{-23}$	91.2	±2.2	$^{+8.3}_{-5.6}$

Table 12: Observed signal yields and purities as obtained from the 2D sideband counting method. Photons are required to be reconstructed in the pseudorapidity range $1.52 \leq |\eta^{\gamma}| < 1.81$. The statistical uncertainty on the signal yield includes the contribution from Poisson fluctuations

E_{T} min	E_{T} max	N_{sig}	stat	syst	P	stat	syst
[GeV]	[GeV]				[%]	[%]	[%]
15.0	20.0	7224	±221	$^{+2010}_{-660}$	49.3	±1.3	$^{+13.7}_{-4.6}$
20.0	25.0	3038	±101	$^{+400}_{-228}$	63.1	±1.5	$^{+8.4}_{-4.7}$
25.0	30.0	1345	±59	$^{+159}_{-100}$	70.0	±2.0	$^{+8.3}_{-5.1}$
30.0	35.0	731	±38	$^{+83}_{-46}$	78.1	±2.3	$^{+9.0}_{-4.9}$
35.0	40.0	441	±27	$^{+51}_{-28}$	84.4	±2.4	$^{+9.6}_{-5.5}$
40.0	50.0	378	±22	$^{+27}_{-21}$	91.7	±1.8	$^{+6.7}_{-5.1}$
50.0	60.0	147	±16	$^{+16}_{-17}$	87.2	±4.3	$^{+9.5}_{-10.0}$
60.0	100.0	154	±12	$^{+12}_{-8}$	96.4	±2.6	$^{+7.3}_{-5.0}$

6.4.2 Results from the template method

The isolated prompt photon purity measured with the template fit method, as a function of the photon reconstructed transverse energy, is shown in Figure 15. The purity and the estimated signal yield in each pseudorapidity and E_T bin are also summarized in Tables 13-15. Both Figure 15 and Tables 13-15 include also the systematic uncertainties on the measured purity and signal yields. The evaluation of these uncertainties is described in detail in the next subsection.
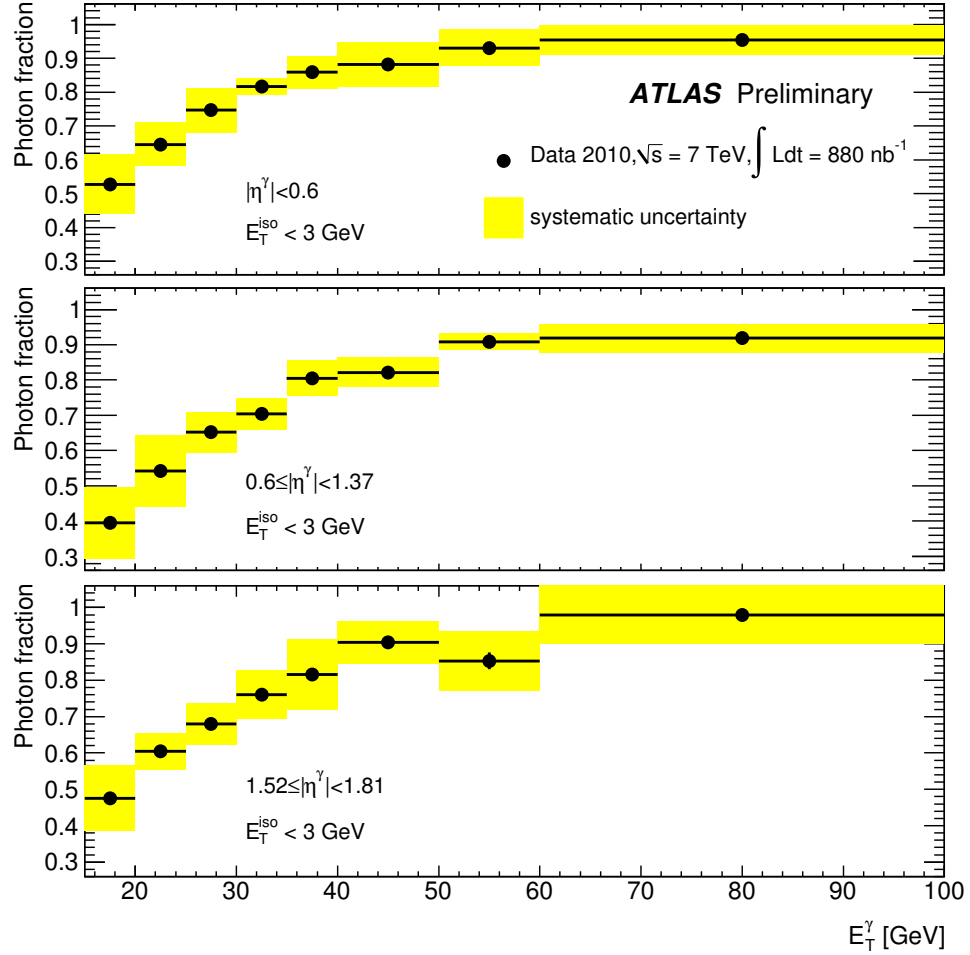

Figure 15: Fraction of isolated prompt photons as a function of the photon transverse energy, as obtained with the template fit method.

Table 13: Observed signal yields and purities as obtained from the template fit to the photon isolation energy distribution. Photons are required to be reconstructed in the pseudorapidity range $0.00 \leq |\eta^\gamma| < 0.60$. The statistical uncertainty on the signal yield includes the contribution from Poisson fluctuations

E_T min [GeV]	E_T max [GeV]	N_{sig}	stat	syst	P [%]	stat [%]	syst [%]
15.0	20.0	11042	±184	±1840	52.8	±0.6	±8.8
20.0	25.0	4865	±102	±490	64.5	±0.8	±6.5
25.0	30.0	2512	±66	±219	74.7	±0.9	±6.5
30.0	35.0	1435	±45	±42	81.6	±1.0	±2.4
35.0	40.0	807	±32	±45	85.9	±1.1	±4.8
40.0	50.0	771	±32	±58	88.2	±1.1	±6.6
50.0	60.0	325	±19	±19	93.1	±1.1	±5.4
60.0	100.0	333	±19	±15	95.4	±0.8	±4.3

Table 14: Observed signal yields and purities as obtained from the template fit to the photon isolation energy distribution. Photons are required to be reconstructed in the pseudorapidity range $0.60 \leq |\eta^\gamma| < 1.37$. The statistical uncertainty on the signal yield includes the contribution from Poisson fluctuations

E_T min [GeV]	E_T max [GeV]	N_{sig}	stat	syst	P [%]	stat [%]	syst [%]
15.0	20.0	12118	±228	±3094	39.6	±0.6	±10.1
20.0	25.0	5675	±121	±1057	54.2	±0.8	±10.1
25.0	30.0	2980	±76	±260	65.3	±0.9	±5.7
30.0	35.0	1539	±51	±96	70.5	±1.1	±4.4
35.0	40.0	1005	±38	±62	80.5	±1.1	±5.0
40.0	50.0	955	±36	±49	82.2	±1.1	±4.2
50.0	60.0	429	±23	±11	90.8	±1.0	±2.4
60.0	100.0	419	±22	±19	91.9	±1.0	±4.1

Table 15: Observed signal yields and purities as obtained from the template fit to the photon isolation energy distribution. Photons are required to be reconstructed in the pseudorapidity range $1.52 \leq |\eta^\gamma| < 1.81$. The statistical uncertainty on the signal yield includes the contribution from Poisson fluctuations

E_T min [GeV]	E_T max [GeV]	N_{sig}	stat	syst	P [%]	stat [%]	syst [%]
15.0	20.0	6909	±149	±1307	47.6	±0.8	±9.0
20.0	25.0	2873	±79	±243	60.4	±1.0	±5.1
25.0	30.0	1298	±48	±109	67.9	±1.3	±5.7
30.0	35.0	681	±32	±60	76.1	±1.5	±6.7
35.0	40.0	423	±24	±50	81.6	±1.5	±9.7
40.0	50.0	369	±21	±24	90.4	±1.0	±5.9
50.0	60.0	142	±13	±14	85.3	±2.3	±8.2
60.0	100.0	154	±12	±13	98.0	±0.6	±8.0

6.4.3 Comparison between the results from the two methods

The results on the prompt photon purity from the two alternative studies are compared in Fig. 16, which shows the difference between the values measured with the two-dimensional sideband technique and those obtained with the template fit method. The error bars represent the statistical uncertainty from the two-dimensional sideband technique only. No systematic uncertainty that affects independently the two methods (for instance, the uncertainty on the signal template determined from the independent sample of electrons from W/Z decays, which amounts to about 4% as described in the next section) is included in the plot.
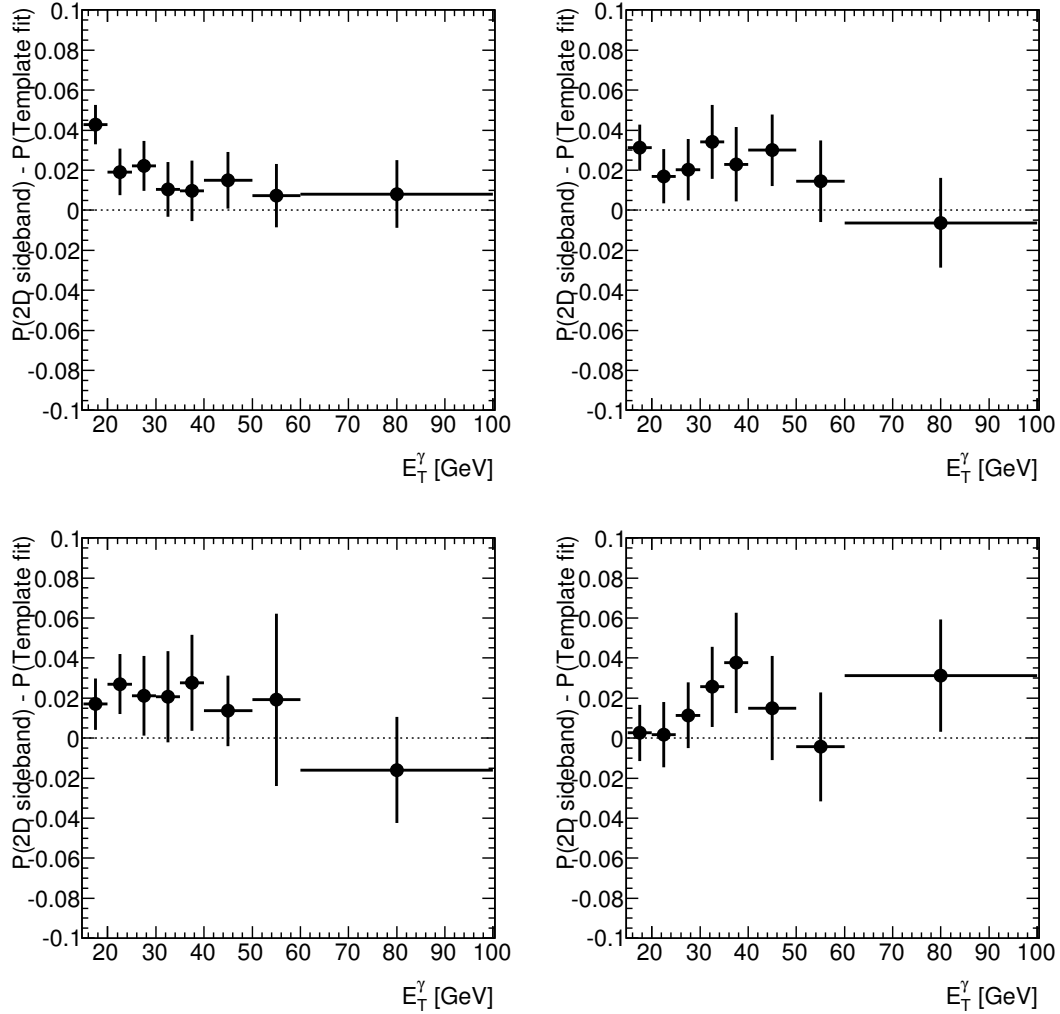

Figure 16: Difference between the purity estimated in data with the two-dimensional sideband technique and with the template fit method. The error bars represent the statistical uncertainty from the two-dimensional sideband technique only.

6.5 Systematic uncertainties

This section summarizes how the various contributions to the signal yield systematic uncertainty have been evaluated.

6.5.1 Systematic uncertainties on the two dimensional sidebands method

The following sources of systematic uncertainties affecting the precision of the purity and signal yield measurement using the 2-dimensional sideband technique are considered:

- **background isolation control region**: the purity is evaluated after changing the isolation control region definition. The minimum isolation energy required for candidates in the non-isolated control regions, which is set to 5 GeV in the nominal measurement, is changed to 4 and 6 GeV. This would be sensitive to uncertainties in the contribution of prompt photons from QED quark radiation, which are less isolated than photons originating from the hard process. Alternative measurements are also performed where a maximum value of the isolation energy is set to 10 or 15 GeV for candidates in the non-isolated control regions, in order to reduce the correlation between the isolation variable and the shower shape distributions that is seen in simulated events in candidates belonging to the upper tail of the isolation distribution. The largest positive change and largest negative change in signal yield and purity from these four alternative measurements are assigned as positive and negative systematic uncertainties to the measured central values;

- **background photon-ID control regions**: the measurement is repeated using a different number of shower shape variables to define the background control region, in order to check that the results do not depend strongly on the choice of the photon-ID control region. The purity and signal yield are computed using between two (F_{side} and w_{s3} only) and five (all the layer-1 variables) shower shape quantities to define the photon-ID control region. Again, the largest positive change and largest negative change in signal yield and purity from these three alternative measurements are assigned as positive and negative systematic uncertainties to the measured central values.

- **signal leakage into the photon-ID background control region**: An upper limit of 5% on the fraction of signal photons being misidentified and therefore contributing the yields N^C and N^D observed in the two background control regions is obtained from the data-driven estimates of the photon identification efficiency of the various tight selection criteria . Therefore, the purity measurement is repeated after varying the leakage coefficients c_2 and c_3 to take into account a $\pm 5\%$ absolute variation of the signal fraction, and take the changes in purity and signal yield as systematic uncertainties on the measured central values

- **signal leakage into the isolation background control region**: an additional source of uncertainty related to the signal subtraction originates from the different isolation distributions for the hard-scattering and bremsstrahlung signal photons, the latter being characterized by larger activity nearby and therefore by usually (slightly) larger values of the isolation energy. As a consequence, the fractions c_1 and c_3 of signal photons belonging to the non-isolated control regions and contributing to the observed yields N^B and M^B depend on the relative amount of prompt and bremsstrahlung photons in the selected sample. In the nominal measurement, the fraction of hard-scattering photons in the signal region is assumed to be 60% of the total prompt photon signal as determined from simulation. A systematic uncertainty on the purity due to this assumption is assigned by redoing the measurement after changing this fraction to 0% or 100%.

- **signal event simulation**: the purity measurement has been repeated using signal samples simulated with `HERWIG` instead of `PYTHIA` to estimate the fraction of signal leaking into the three background control regions

- **background correlations**: Non-negligible correlations between the isolation variable and the photon identification quantities used to select the candidates in the two-dimensional plane would affect the measured purity. If the correlation was precisely known, it could be taken into account in the

formulae relating the signal purity to the observed yields in the four regions of the two dimensional plane (see [11]). The simulation of background events shows some hints of non-negligible correlations, but because of the limited size of the simulated samples the uncertainties can be quite big in certain intervals of E_T and $|\eta|$ and the central values have large oscillations. Therefore, these correlations are ignored when calculating the final result, and used to assign a systematic uncertainty corresponding to this choice, computed after averaging over all the E_T bins in the same pseudorapidity range. Calling P_0 and $P_R \pm \sigma_{P_R}$ the purities evaluated without and with the correlation correction (where σ_{P_R} comes from the uncertainty on the correlation itelf), a weighted average is evaluated for all $\Delta P = (P_R - P_0) \pm \sigma_{P_R}$ in the same $|\eta|$ region, and the maximum between this average and its uncertainty is quoted as systematic. The effect is $< 0.6\%$ for each of the barrel regions, and $\sim 3.6\%$ for each of the endcap regions.

The various systematic uncertainty sources and the corresponding uncertainties on the signal yield are summarized in Tables 16- and 18.

Table 16: Systematic uncertainties, for different E_T intervals, on the estimated number of signal photons in the pseudorapidity range $0.00 \leq |\eta^\gamma| < 0.60$.

E_T min (GeV)	E_T max (GeV)	tight-ID control region	isolation control region	leakage in non-isolated region	HERWIG vs PYTHIA	leakage in non-ID region	bkg correlation
15	20	$^{+766}_{-1842}$	$^{+282}_{-348}$	$^{+587}_{-364}$	±156	$^{+592}_{-489}$	±84
20	25	$^{+306}_{-465}$	$^{+39}_{-43}$	$^{+286}_{-175}$	±76	$^{+189}_{-159}$	±30
25	30	$^{+118}_{-164}$	$^{+20}_{-55}$	$^{+142}_{-87}$	±10	$^{+76}_{-65}$	±13
30	35	$^{+37}_{-6}$	$^{+9}_{-7}$	$^{+65}_{-39}$	±0	$^{+46}_{-39}$	±7
35	40	$^{+15}_{-24}$	$^{+5}_{-6}$	$^{+39}_{-25}$	±6	$^{+24}_{-20}$	±4
40	50	$^{+10}_{-13}$	$^{+11}_{-10}$	$^{+39}_{-24}$	±12	$^{+22}_{-19}$	±3
50	60	$^{+5}_{-4}$	$^{+2}_{-4}$	$^{+12}_{-8}$	±4	$^{+9}_{-8}$	±1
60	100	$^{+1}_{-1}$	$^{+2}_{-1}$	$^{+12}_{-7}$	±6	$^{+14}_{-11}$	±1

Table 17: Systematic uncertainties, for different E_T intervals, on the estimated number of signal photons in the pseudorapidity range $0.60 \leq |\eta^\gamma| < 1.37$.

E_T min (GeV)	E_T max (GeV)	tight-ID control region	isolation control region	leakage in non-isolated region	HERWIG vs PYTHIA	leakage in non-ID region	bkg correlation
15	20	$+3762 \atop -198$	$+172 \atop -158$	$+769 \atop -469$	±322	$+1108 \atop -862$	±183
20	25	$+1144 \atop -250$	$+5 \atop -53$	$+323 \atop -198$	±58	$+381 \atop -306$	±62
25	30	$+396 \atop -2$	$+21 \atop -45$	$+136 \atop -84$	±20	$+183 \atop -149$	±27
30	35	$+141 \atop 0$	$+0 \atop -10$	$+76 \atop -48$	±10	$+96 \atop -78$	±13
35	40	$+42 \atop 0$	$+13 \atop -9$	$+36 \atop -23$	±12	$+63 \atop -51$	±7
40	50	$+53 \atop -1$	$+5 \atop -34$	$+44 \atop -27$	±13	$+60 \atop -49$	±7
50	60	$+9 \atop 0$	$+1 \atop -6$	$+10 \atop -6$	±4	$+29 \atop -23$	±3
60	100	$+18 \atop 0$	$+2 \atop -7$	$+14 \atop -9$	±7	$+23 \atop -19$	±2

Table 18: Systematic uncertainties, for different E_T intervals, on the estimated number of signal photons in the pseudorapidity range $1.52 \leq |\eta^\gamma| < 1.81$.

E_T min (GeV)	E_T max (GeV)	tight-ID control region	isolation control region	leakage in non-isolated region	HERWIG vs PYTHIA	leakage in non-ID region	bkg correlation
15	20	$+1854 \atop 0$	$+75 \atop -135$	$+437 \atop -266$	±84	$+426 \atop -346$	±469
20	25	$+301 \atop 0$	$+3 \atop -50$	$+147 \atop -90$	±60	$+143 \atop -118$	±154
25	30	$+109 \atop -28$	$+24 \atop -27$	$+69 \atop -42$	±2	$+65 \atop -53$	±61
30	35	$+63 \atop 0$	$+2 \atop -4$	$+26 \atop -16$	±3	$+37 \atop -30$	±30
35	40	$+38 \atop 0$	$+1 \atop -6$	$+19 \atop -13$	±5	$+21 \atop -17$	±17
40	50	$+15 \atop -0$	$+3 \atop -7$	$+8 \atop -5$	±2	$+17 \atop -14$	±13
50	60	$+2 \atop -10$	$+1 \atop -3$	$+10 \atop -7$	±6	$+9 \atop -7$	±5
60	100	$+7 \atop 0$	$+0 \atop -0$	$+2 \atop -1$	±0	$+7 \atop -6$	±5

6.5.2 Systematic uncertainties on the template fits

There are several broad categories of systematic uncertainties for this technique, including:

- uncertainties due to the definition of the background template

- uncertainties due to the definition of the signal template

- uncertainties due to the choice of fitter and the details of the fit

Detailed studies using simulated and collision data were performed to estimate the uncertainties from each of the sources above. For the tests with simulated data, a realistic sample containing signal and background events across the full E_T and η range covered in this analysis was constructed from the QCD samples described in section 3.2. For tests with collision data, several details were varied to test the stability of the results.

The full systematic uncertainties on the purities and signal yields are listed in Tables 13 - 15.

Uncertainty from the background template   The uncertainties originating in the background template dominate the total uncertainty on the template fit method for all E_T and η regions. Simulated samples are used to check the pull on the purities due to the background templates extracted from the reversed-cuts sample. In these tests, the signal template is taken from the truth-matched signal in the test sample. The pulls are largely symmetric about zero over the full η and E_T acceptance, ranging from 6% (absolute) at low E_T, down to 2% (absolute) at high E_T.

Another check is performed with collision data, where the choice of cuts to reverse is changed to create a different background template. In the nominal prescription, four strip cuts are reversed: F_{side}, w_{s3}, ΔE, and E_{ratio}. The validity of this choice is tested with two additional sets of cuts. In one set, only F_{side} and w_{s3} are reversed. In another set, all of the cuts in the nominal case are reversed, with the addition of the cut on $w_{s\,tot}$. The spread in the resulting purities gives uncertainties between 2% and 8%, depending on E_T and η.

The final uncertainties associated with the background template are then estimated from these two checks, and range from 3% to just over 8%.

Uncertainty from the signal template   The uncertainty due to choice of signal template is evaluated using simulated data. In these tests, the background template is taken from truth-matched background in the test sample, and a simulated sample of electrons from W and Z decays are used to construct the signal template. The resulting deviations in the estimated purities from the true purities are found to be less than 3% for all E_T and η bins, with some estimates deviating by more than the associated statistical uncertainty. A further uncertainty may come from the mixture of photons from hard process and from fragmentation: choosing only hard photons would give a sharper template, leading to a purity underestimated by $\sim -2.5\%$, while choosing fragmentation photons only would yield a broader template and a purity overestimate by $\sim +2.5\%$. A total systematic uncertainty of 4% is assigned to cover the uncertainty from the signal template. Systematic uncertainties originating from the uncertainty on the electron-vs-photon correction from the Monte Carlo sample that was used (Herwig vs Pythia, nominal vs distorted geometry) were neglected.

Uncertainty from the fitter and details of the fit   The fitter is tested in simulation, by constructing the signal and background templates from the truth-matched signal and background in the test sample. This represents the ideal case, where the signal and background in the test data are perfectly modeled by the templates. In this situation, the technique measures purities within a fraction of a percent of truth for all E_T and η, with similarly sized statistical uncertainties. As any discrepancies are consistent with zero,

and without any systematic bias, zero uncertainty is assigned due to the fitter. Other details, such as the choice of bin size, have also been found to have negligible uncertainties.

6.6 Electron background subtraction

Prompt electrons with low isolation energy and passing the calorimeter-based tight photon identification criteria may bias the estimated photon yield if their fake rate is too high. The main electron production mechanisms in ATLAS are semileptonic hadron decays (mostly from hadrons containing heavy flavor quarks) and decays of electroweak bosons and τ leptons (the largest contribution being from W decays). Electrons from the former are often produced in association with jets, and therefore have large isolation energy. They tend to populate all the various signal and background regions of the two-dimensional plane exploited in the purity measurement described in Section 6.2; their presence does not therefore bias the measurement as they do not invalidate the basic assumptions of that technique. On the other hand, electrons from W, Z and τ decays are more isolated and more similar to signal photons. Their yield therefore contributes to the estimated signal yield of Section 6.2, from which it is then subtracted before the cross section measurement. The fraction of electrons reconstructed as signal photons in the final data sample is estimated by using the $e\gamma$ invariant mass peak observed in ATLAS at the Z mass to determine the probability of misidentifying an electron as a photon, as a function of the electron transverse energy and pseudorapidity. This probability, multiplied by the integrated luminosity of the data sample (880 nb^{-1}) and by the production cross section of W, Z and τ in pp collisions at $\sqrt{s} = 7$ TeV times the branching ratio for the decay into an electron, yields the expected number of electrons being identified as isolated photon candidates in our sample. The fraction of photon candidates estimated to come from isolated electrons is on average around 0.5%, however it depends significantly on the transverse energies, with a maximum value of (2.5% ± 0.8%) for transverse energies between 40 and 50 GeV, due to the kinematic distribution of electrons from W and Z decays. The uncertainty on the electron fraction ranges between 0.3% and 0.9%. More details are provided in [11].

7 Cross section measurement

7.1 Principle of the cross section measurement

The average differential cross section for the production of isolated prompt photons in a certain bin i of (true) E_T (integrated over one true $|\eta|$ bin k) is:

$$\left\langle \frac{d\sigma_i^{\mathrm{isol},k}}{dE_T^{\mathrm{true}}} \right\rangle = \frac{1}{\int \mathcal{L}dt} \frac{N_i^{\gamma,\mathrm{true},\mathrm{isol},k}}{\Delta E_{\mathrm{T},i}^{\mathrm{true}}} \tag{10}$$

where $N_i^{\gamma,\mathrm{true},\mathrm{isol},k}$ is the number of true prompt photons, with parton-level isolation lower than 4 GeV, in bin k of true $|\eta|$ and in bin i of E_T^{true}, whose width is $\Delta E_{\mathrm{T},i}^{\mathrm{true}}$. $\int \mathcal{L}dt = (8.8 \pm 1.0) \times 10^2$ nb^{-1} is the integrated luminosity of the sample under study.

Taking into account the reconstruction efficiency, defined in Eq. 2, the offline selection efficiency, defined in Eq. 3, and the trigger efficiency of Eq. 5, the relation between the number of prompt photons $N_i^{\gamma,\mathrm{reco},\mathrm{isol},k}$, reconstructed in a bin i of reconstructed transverse energy and in a bin k of reconstructed $|\eta|$, with experimental isolation lower than 3 GeV, and the differential cross section in the various bins j of true E_T is given by

$$N_i^{\gamma,\mathrm{reco},\mathrm{isol},k} = \left(\int \mathcal{L}dt \right) \varepsilon^{\mathrm{trig}} \varepsilon_i^{\mathrm{offl},k} \sum_j R_{ij}^k \varepsilon_j^{\mathrm{reco},k} \Delta E_{\mathrm{T},j}^{\mathrm{true}} \left\langle \frac{d\sigma_j^{\mathrm{isol},k}}{dE_T^{\mathrm{true}}} \right\rangle \tag{11}$$

where the ε_l means the average of the efficiency ε in a certain bin l of transverse energy (see Tables 5 and 6), and R_{ij}^k is the *transverse energy response matrix* in the k-th $|\eta|$ bin. The elements of R_{ij}^k represent the probability for a prompt photon of true transverse energy in bin j, reconstructed in the k-th $|\eta|$ bin and having experimental isolation lower than 3 GeV, to have reconstructed transverse energy in bin i. Due to resolution effects and to the uncertainty on the energy scale of the electromagnetic calorimeter, the response matrix is not simply a diagonal matrix with 1's in the diagonal cells and 0's in all the other cells; i.e., $R_{ij}^k \neq \delta_{ij}$. The response matrix can be determined from the simulation of signal events: in this case, the matrix is obtained by weighting the direct and the fragmentation photon samples according to their PYTHIA LO cross sections. One would be tempted to invert the response matrix and apply it to the number of observed events in order to extract the cross section:

$$\left\langle \frac{d\sigma_i^{\mathrm{isol},k}}{dE_T^{\mathrm{true}}} \right\rangle = \frac{1}{\left(\int \mathcal{L}dt \right) \varepsilon^{\mathrm{trig}} \varepsilon_i^{\mathrm{reco},k} \Delta E_{\mathrm{T},i}^{\mathrm{true}}} \sum_j (R^k)_{ij}^{-1} \frac{N_j^{\gamma,\mathrm{reco},\mathrm{isol},k}}{\varepsilon_j^{\mathrm{offl},k}} \tag{12}$$

The problem with this approach is that the response matrix, determined from a simulated sample of limited size, may be singular; even in the case when the matrix can be inverted, the method may be sensitive to large statistical fluctuations, especially in the non-diagonal cells of the response matrix, which may lead to large negative terms of the inverse $(R^k)^{-1}$ and, in extreme cases, to negative numbers of unfolded events. [29]

The simplest solution to this *unfolding* problem consists in the so-called *bin-by-bin* correction: a *generalized efficiency* is evaluated from simulated signal events, and the ratio between the number of prompt photons falling in a certain bin of the reconstructed transverse energy and the number of prompt photons in the same bin of the true transverse energy is calculated. This efficiency is then used to estimate the number of true events from the number of events observed in that bin. One can therefore write:

$$\left\langle \frac{d\sigma_i^{\mathrm{isol},k}}{dE_T^{\mathrm{true}}} \right\rangle = \frac{1}{\left(\int \mathcal{L}dt \right) \varepsilon^{\mathrm{trig}} \varepsilon_i^{\mathrm{reco},k} \Delta E_{\mathrm{T},i}^{\mathrm{true}}} \sum_j U_{ij}^k \frac{N_j^{\gamma,\mathrm{reco},\mathrm{isol},k}}{\varepsilon_j^{\mathrm{offl},k}} \tag{13}$$

where

$$U_{ij}^k = u_i^k \delta_{ij} \qquad (14)$$

is a diagonal matrix and the entries u^k are the inverse of these generalized efficiencies. This method works well if the bin-to-bin migrations are small, and the standard deviation of the transverse energy smearing is smaller than the bin size. Given the electromagnetic calorimeter energy resolution and the width of the bins in this analysis (5 to 40 GeV), this choice seems reasonable and will be used to evaluate the nominal cross section results in the following.

One of the negative aspects of this approach is that the generalized efficiencies are evaluated purely from simulation. The systematic uncertainties listed in Table 7 have been evaluated including also the contribution to the energy reconstruction from the various sources of uncertainty (including material effects and cross-talk).

An alternative approach is used to cross-check the bin-by-bin unfolding results and assign some systematic uncertainties. In this approach, the cross section is measured using a more elaborate technique [30], based on an iterative unfolding procedure inspired by Bayes' theorem. Using Bayes' theorem, one can write:

$$N_i^{\text{true}} \;=\; \sum_j N_j^{\text{reco}} P(N_i^{\text{true}}|N_j^{\text{reco}}) \qquad (15)$$

$$=\; \sum_j N_j^{\text{reco}} \frac{P(N_j^{\text{reco}}|N_i^{\text{true}})P_0(N_i^{\text{true}})}{\sum_l P(N_j^{\text{reco}}|N_l^{\text{true}})P_0(N_l^{\text{true}})} \qquad (16)$$

$$=\; \sum_j U_{ij} N_j^{\text{reco}} \qquad (17)$$

where U_{ij} is the unfolding matrix

$$U_{ij} = \frac{P(N_j^{\text{reco}}|N_i^{\text{true}})P_0(N_i^{\text{true}})}{\sum_l P(N_j^{\text{reco}}|N_l^{\text{true}})P_0(N_l^{\text{true}})}, \qquad (18)$$

$P(N_j^{\text{reco}}|N_i^{\text{true}})$ is easily identified with the response matrix R_{ij}, and $P_0(N_l^{\text{true}})$ is the *a priori* or initial probability of a signal candidate to have true transverse energy in bin l. Since the unfolding matrix depends on this initial probability, which is exactly the quantity of interest, the formula may seem sterile; in practice, one can start using as first guess of P_0 the true E_T distribution from simulation and then apply the Bayes formula iteratively, replacing at each nth step the *a priori* probability with the unfolded probability $\frac{N_i^{\text{true}}}{\sum_l N_l^{\text{true}}}$ obtained in the $n^{\text{th}} - 1$ step. After a few iterations (3-4) the procedure converges to a situation where the resulting unfolded distribution does not different significantly from the input one.

7.2 Response matrices

The E_T response matrices in the four pseudorapidity regions under study, for true prompt photons that are reconstructed in one of the four $|\eta|$ bins ($\eta_1 \le |\eta_{\text{reco}}^\gamma| < \eta_2$), in the fiducial region defined by the object quality criteria and have experimental isolation energy lower than 3 GeV, are evaluated from simulated signal events, using a cross-section weighted mixture of the direct and fragmentation samples. Various samples with different true E_T photon filter thresholds are combined to have a good statistics in all the transverse energy bins. Overlap between these samples are removed by requiring explicitly that the true photon transverse energy be:

- lower than 20 GeV in the samples with a 7 GeV filter threshold

- between 20 GeV and 40 GeV in the samples with a 17 GeV threshold

- between 40 GeV and 100 GeV in the samples with a 35 GeV threshold

- above 100 GeV in the samples with a 70 GeV threshold

The response matrices obtained in this way are shown in Figure 17.
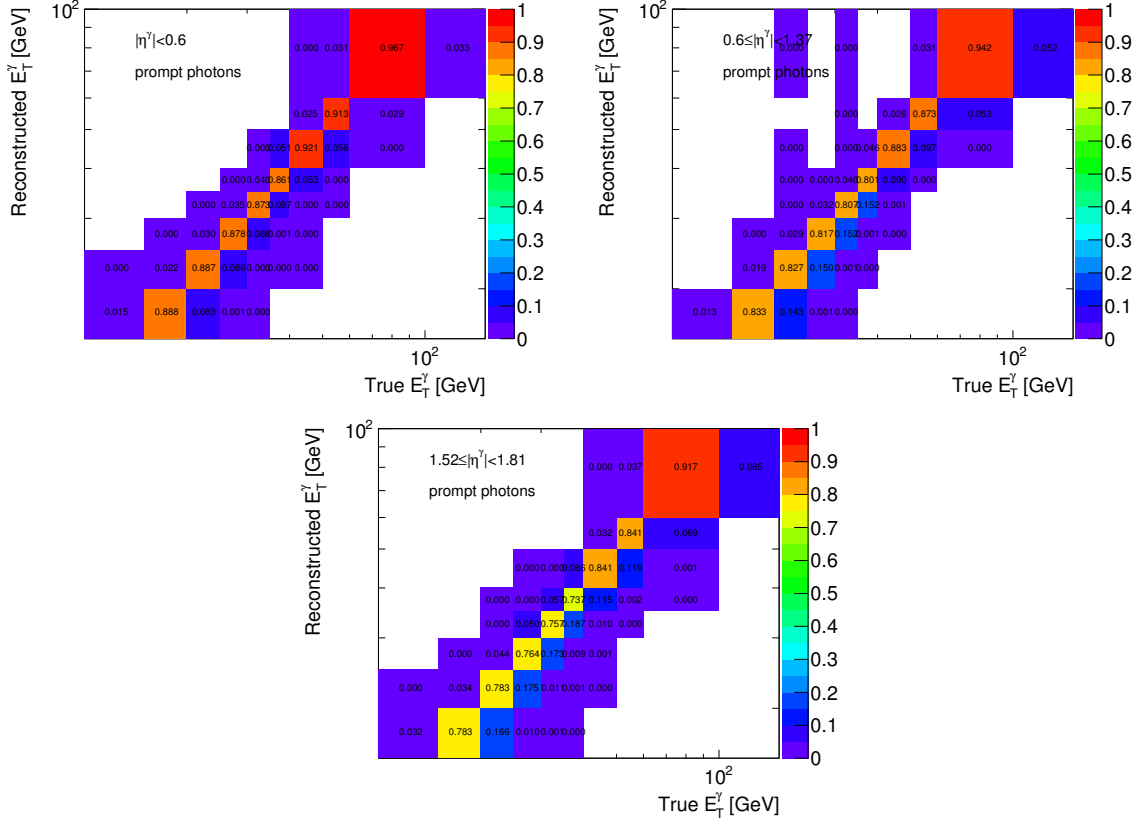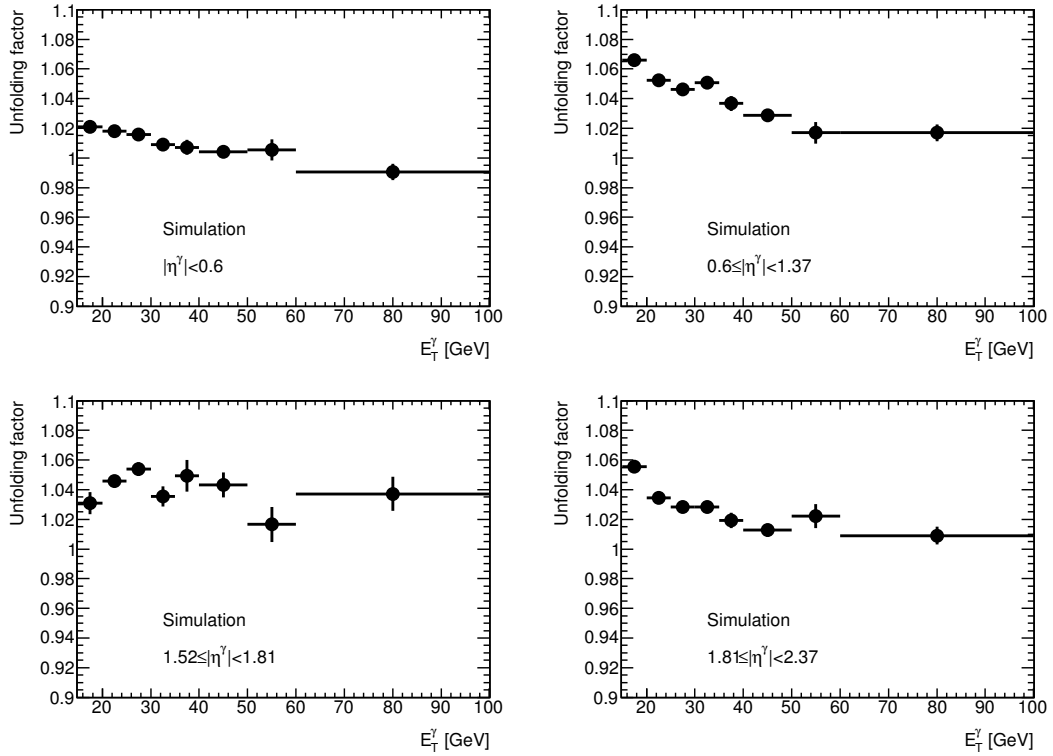

Figure 17: Transverse energy response matrices as determined from a simulation of prompt photons. Top left: $|\eta^\gamma| < 0.6$. Top right: $0.6 \leq |\eta^\gamma| < 1.37$. Bottom: $1.52 \leq |\eta^\gamma| < 1.81$.

7.3 Bin-by-bin unfolding matrices

The bin-by-bin unfolding matrices are the diagonal matrices of the inverse of the generalized efficiencies, $U_{ij}^k = u_i^k \delta_{ij}$. They are determined from the signal Monte Carlo simulation, mixing the various samples as described previously, and computing the ratios

$$u_i^k = \frac{N^\gamma(\eta_{k,1} \leq |\eta_{\text{reco}}^\gamma| < \eta_{k,2}, E_{\text{T,reco}}^{\text{iso}} < 3 \text{ GeV}, E_{\text{T},i,1} \leq E_{\text{T,true}} < E_{\text{T},i,2})}{N^\gamma(\eta_{k,1} \leq |\eta_{\text{reco}}^\gamma| < \eta_{k,2}, E_{\text{T,reco}}^{\text{iso}} < 3 \text{ GeV}, E_{\text{T},i,1} \leq E_{\text{T,reco}} < E_{\text{T},i,2})} \tag{19}$$

The values of the unfolding coefficients u_i^k for all the E_T and pseudorapidity ranges under study are summarized in Table 19.

The four bin-by-bin unfolding matrices are shown in Figure 18.

7.4 Bayesian unfolding matrices

The unfolding matrices U_{ij} of Eq. 18, determined with the iterative Bayesian procedure after four iterations using as starting probability distribution the observed prompt photon spectrum in the simulation,

Table 19: Isolated prompt photon transverse energy bin-by-bin unfolding coefficients. They are defined as the ratio between the number of true prompt photons reconstructed in a certain interval k of pseudorapidity, passing e/γ object quality criteria and with reconstructed isolation energy lower than 3 GeV, with true E_T in a certain bin i, and the number of true prompt photons (passing the same pseudorapidity and isolation requirements) with reconstructed transverse energy in the same bin.

E_T min [GeV]	E_T max [GeV]	$0.00 \leq |\eta^\gamma| < 0.60$	$0.60 \leq |\eta^\gamma| < 1.37$	$1.52 \leq |\eta^\gamma| < 1.81$	$1.81 \leq |\eta^\gamma| < 2.37$
15.0	20.0	1.021 ± 0.003	1.066 ± 0.004	1.031 ± 0.007	1.055 ± 0.004
20.0	25.0	1.018 ± 0.001	1.052 ± 0.002	1.046 ± 0.003	1.035 ± 0.001
25.0	30.0	1.016 ± 0.002	1.046 ± 0.002	1.054 ± 0.005	1.028 ± 0.002
30.0	35.0	1.009 ± 0.003	1.051 ± 0.004	1.035 ± 0.007	1.028 ± 0.004
35.0	40.0	1.007 ± 0.005	1.037 ± 0.005	1.049 ± 0.011	1.019 ± 0.005
40.0	50.0	1.004 ± 0.004	1.029 ± 0.004	1.043 ± 0.008	1.013 ± 0.004
50.0	60.0	1.006 ± 0.007	1.017 ± 0.007	1.017 ± 0.012	1.022 ± 0.008
60.0	100.0	0.991 ± 0.006	1.017 ± 0.006	1.037 ± 0.011	1.009 ± 0.006

Figure 18: Bin-by-bin transverse energy unfolding coefficients as determined from a simulation of prompt photons. Top left: $|\eta^\gamma| < 0.6$. Top right: $0.6 \leq |\eta^\gamma| < 1.37$. Bottom: $1.52 \leq |\eta^\gamma| < 1.81$

are shown in Figure 19.

The coefficients of the unfolding matrices and the resulting cross sections are found to be stable to better than 1% after three iterations, as can be seen in Figure 20.

The cross sections determined with the iterative procedure are consistent with those obtained with the simple bin-by-bin unfolding, with differences within 2%, as can be seen in Figure 21 where the cross
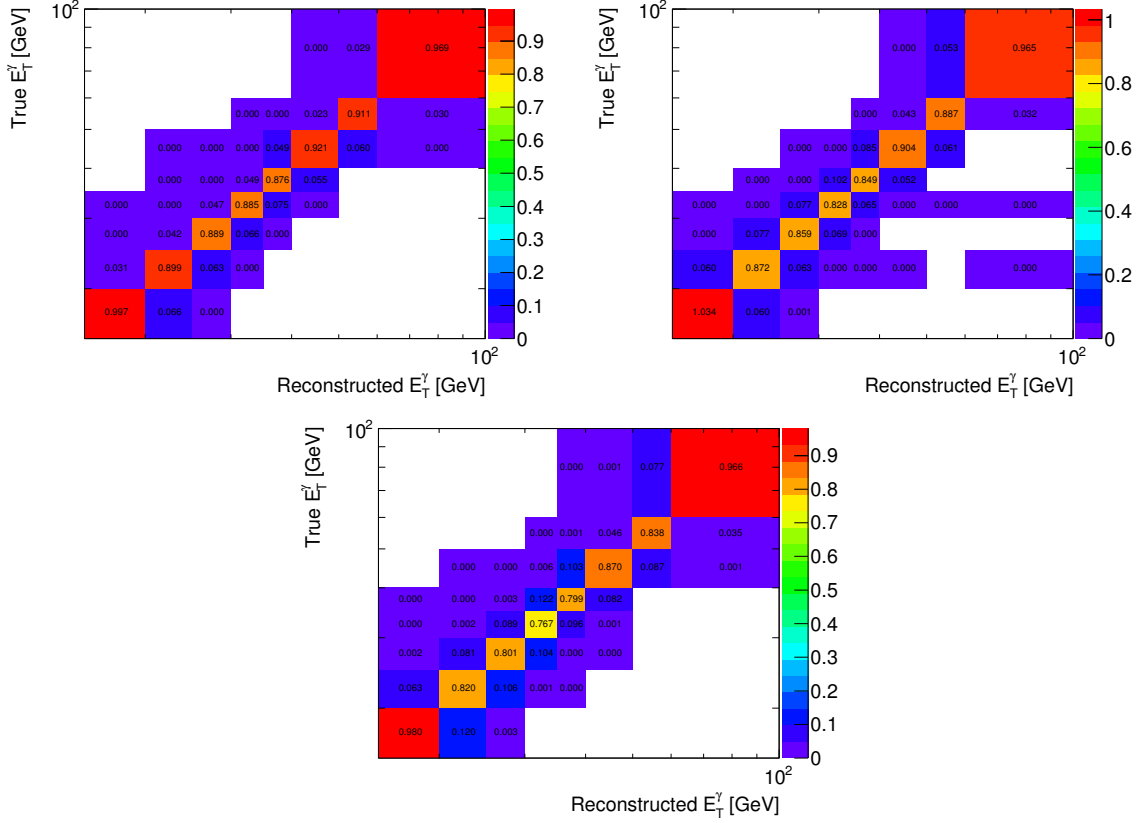
45

Figure 19: Transverse energy unfolding matrices as determined with the iterative approach after four iterations, using as initial probability distribution the one obtained from a simulation of prompt photons. Top left: $|\eta^\gamma| < 0.6$. Top right: $0.6 \leq |\eta^\gamma| < 1.37$. Bottom: $1.52 \leq |\eta^\gamma| < 1.81$.

sections are divided by the central values determined with the bin-by-bin unfolding.

7.5 Parton vs. particle isolation

The unfolding factors also correct for the inefficiency of the reconstructed isolation requirement to retain photons that are truly isolated. To check the impact of applying the isolation requirement at the parton- or particle-level, the cross section was computed separately for each case. Figure 22 shows the ratio of the measured differential cross section computed using a particle-level isolation requirement to that using a parton-level isolation requirement. The differences in all regions of transverse energy and pseudorapidity are small, at the 1% level, which indicates the robustness of the isolation prescription to the effects of hadronization.

7.6 Cross section results

The cross section results, including systematic uncertainties, are shown in the next Section.
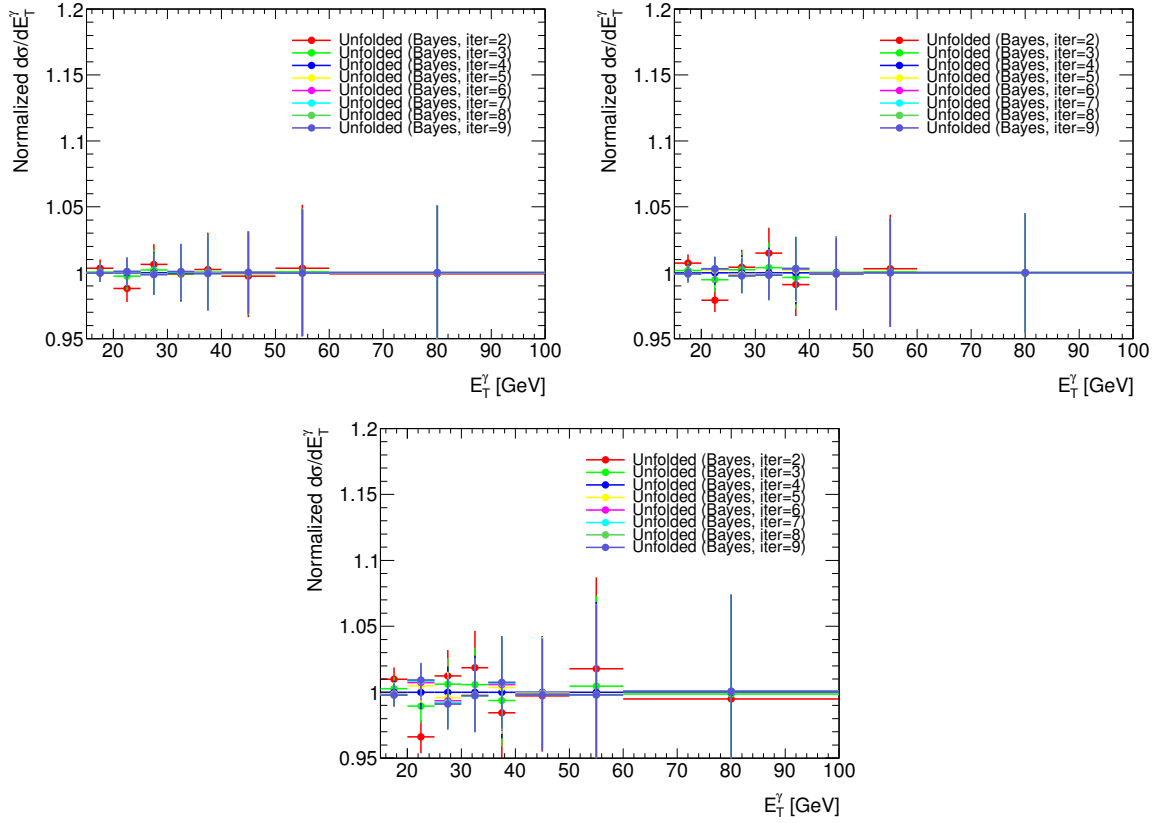
Figure 20: Ratio between the measured cross section, with the iterative approach, after a number of iterations variable between 2 and 9, and the nominal result after four iterations. Top left: $|\eta^\gamma| < 0.6$. Top right: $0.6 \leq |\eta^\gamma| < 1.37$. Bottom: $1.52 \leq |\eta^\gamma| < 1.81$.
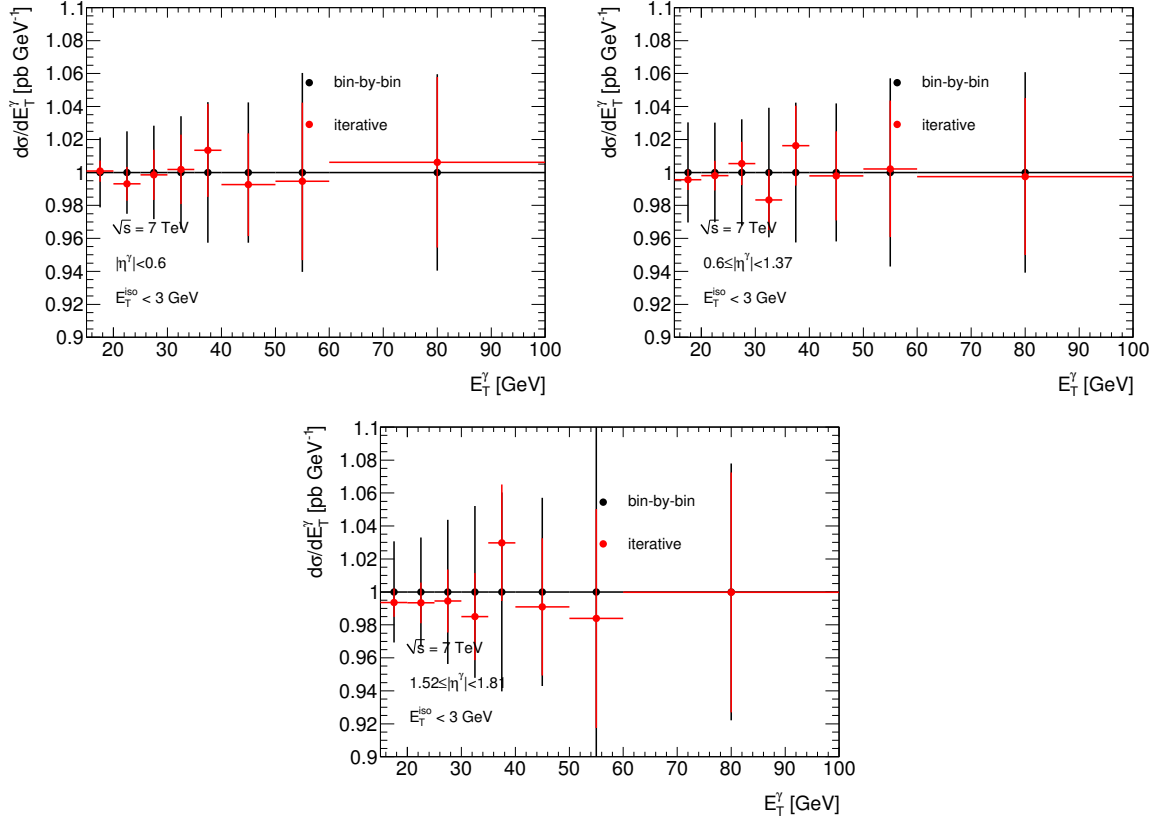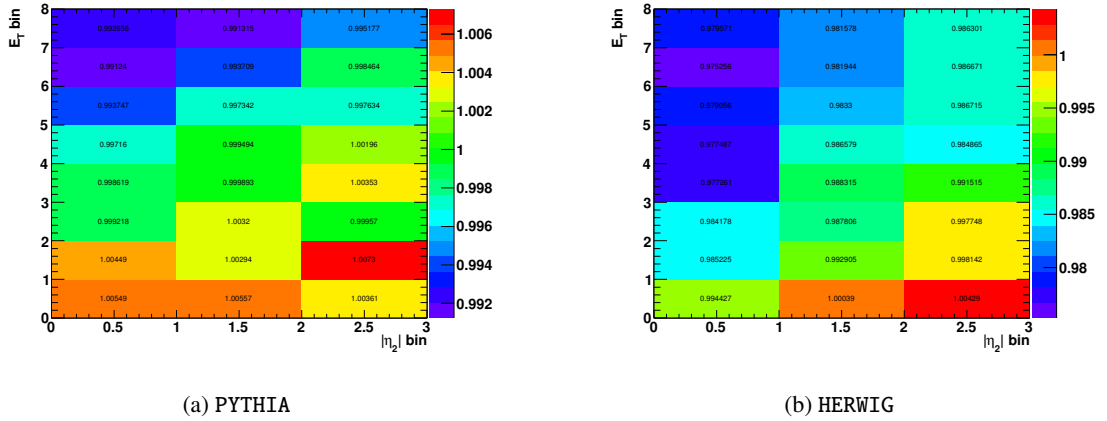
Figure 21: Measured cross sections, with the iterative and the bin-by-bin unfolding approaches, normalized to the central values obtained with the bin-by-bin unfolding. Uncertainties are purely statistical. Top left: $|\eta^\gamma| < 0.6$. Top right: $0.6 \le |\eta^\gamma| < 1.37$. Bottom: $1.52 \le |\eta^\gamma| < 1.81$.

(a) PYTHIA

(b) HERWIG

Figure 22: Ratio of the measured differential cross section using a parton-level isolation requirement of 4 GeV to that using a particle-level isolation cut at 4 GeV, with unfolding factors computed using prompt photons from PYTHIA (left) and HERWIG (right). In all cases the differences are less than 1% for PYTHIA, and less than 3% for HERWIG.

8 Cross section systematic uncertainties

8.1 Purity Estimates

The systematic uncertainties originated from the estimation of the number of signal events, either from the two-dimensional sideband method or from the template-fit method, are described in detail in sections 6.5.1 and 6.5.2. The values are listed in Tables 10–12 and in Tables 13–15. The uncertainty from the electron contamination is added in quadrature to the uncertainty on the signal photon yield. The potential biases due to the PYTHIA fragmentation model were evaluated by varying the background rates of π^0's, η's, and ω's by 50%; the effects are completely covered by systematics associated with the construction of the background template from the reverse-cuts procedure. The total signal yield relative uncertainties are propagated into the cross-section measurement assuming no correlation between them and the uncertainties related to the unfolding, efficiency, energy scale, or luminosity.

8.2 Luminosity

The integrated luminosities are calculated during runs by measuring interaction rates using several ATLAS devices at small angles to the beam direction, with the absolute calibration obtained from Van der Meer scans. The relative systematic uncertainty on the luminosity measurement is estimated to be 11% [31] and translates directly into a 11% relative uncertainty on the cross-section.

8.3 Reconstruction, Identification, Trigger

The systematic uncertainties on the reconstruction and identification efficiencies are evaluated together, as described in detail in [20]. The resulting uncertainties are listed in section 5.2.3. Of the uncertainties which contribute to this measurement, the largest effects are due to material effects (ranging from 1-8% absolute uncertainties, largest at low E_T^γ) and the uncertainty associated with the shower-shape-corrected efficiency estimates from simulation (ranging from 1-5% absolute uncertainties, largest at low E_T).

No additional systematic uncertainty comes from the comparison of the efficiencies estimated with the electron-extrapolation method with the efficiencies from the nominal, shifted shower-shape efficiencies from photon Monte Carlo. The agreement between the electron-extrapolated and MC efficiencies, after accounting for all of the associated uncertainties, in the three η regions under investigation in this analysis, is good enough that the results are used only as a cross-check.

The uncertainty on the trigger efficiency (0.5%) is nearly negligible.

8.4 Unfolding coefficients

The unfolding coefficients used to correct the measured cross-section for E_T bin-bin migrations are taken from the simulations. There are four sources of uncertainties on the unfolding coefficients:

- the uncertainty due to the limited statistics of the simulated samples from which they are determined

- the dependence on the E_T^γ distribution predicted by PYTHIA

- the energy scale uncertainty

- the uncertainty on the energy resolution, which may affect bin-to-bin migrations between adjacent E_T bins

The uncertainty from the limited Monte Carlo statistics is evaluated by propagating the statistical uncertainty on the unfolding coefficients ($\sigma^{\text{stat}}(u_i^k)$) to a relative systematic uncertainty $\sigma^{\text{stat}}(u_i^k)/u_i^k$ on the measured cross-section in the E_T bin i and $|\eta|$ bin k.

The uncertainty from the PYTHIA E_T distribution can be estimated by repeating the cross-section measurement with the iterative procedure outlined in Section 7.1, which uses the PYTHIA E_T distribution only in the first iteration, and then replaces it at each nth step with the unfolded spectrum (in data) from step $n − 1$. The differences between the two results are small as shown in Figure 21, and a conservative 2% uncertainty is assigned.

The energy-scale uncertainty is taken from test beam studies, where it is quoted as 3%. Preliminary studies with data indicate that the energy scale uncertainty is smaller than this [32], so this should be a conservative bound on the efficiency. Systematics associated with the energy scale are evaluated for reconstruction and photon identification efficiencies, where the effects are found to be negligible. The effects of the energy scale on the purity estimates are similarly small. The primary effect of the energy scale is to cause bin-to-bin migrations of reconstructed photons in the unfolding. We recompute the reconstruction efficiency and the transverse energy response matrices using simulated signal events after shifting the true photon energy by ±3% and compute the cross section. The difference with respect to the nominal value is taken as the systematic uncertainty on the cross section originating from the uncertainty on the photon energy scale. The unfolding coefficients obtained after shifting the energy scale by ±3% are shown in Figure 23.
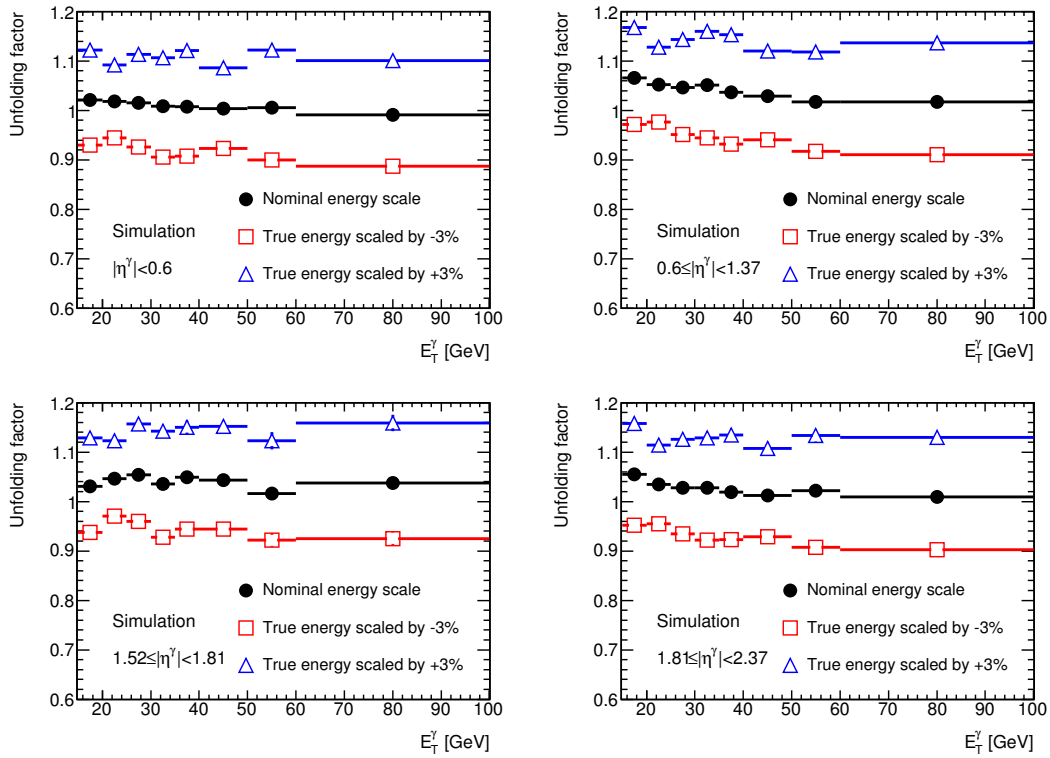

Figure 23: Bin-by-bin transverse energy unfolding factors as determined from a simulation of prompt photons: nominal energy scale (full black dots), and after shifting the true photon energy by −3% (red open squares) or +3% (blue open triangles).

The uncertainty from the energy resolution is evaluated in two ways. First, we evaluate the uncertainty from a possible underestimation in the simulation of the gaussian part of the resolution. We

consider a 10-20% relative increase of the sampling term (adding a $2\%/\sqrt{E}$ contribution to the energy resolution) and a 1.3% absolute increase to the constant term of the simulation in the barrel and a 2.9% increase in the endcap (in the simulation the constant term is 0.7%). These quantities are added in quadrature. Test beam studies indicated the sampling term to agree in data and MC within 10-20%, and $Z \to ee$ studies in data seem to indicate that a total of 1.5% (3.0%) in the barrel (endcap) is a reasonable upper limit for the constant term. We recompute the unfolding coefficients, running over the prompt photon sample and adding to the reconstructed photon E_T an additional shift which is randomly generated from a gaussian distribution with zero mean and width equal to $E_T \times (2\%/\sqrt{E_T} \oplus 1.3\%)$. The variation of the unfolding coefficients is found to be very small, less than 1% and consistent with zero within statistical uncertainties. Second, we evaluate the uncertainty on the unfolding coefficients arising from the non-gaussian tails of the $E_{T,\text{reco}}/E_{T,\text{true}}$ distribution. To this purpose we compare the unfolding coefficients obtained from the nominal simulation with those obtained using a simulation with additional material. We use the same geometry, ATLAS-GEO-10-08-00, used to study material-related systematic uncertainties on the photon efficiency; this geometry is estimated to represent a conservative upper limit of the additional material that may be present in ATLAS and not modeled in the nominal simulation. The main effect of the additional material is that part of the photon energy is deposited in the material before the calorimeter and therefore the reconstructed energy is smaller than the true one, since the calibration constants in the alternative geometry are the nominal ones. Therefore the unfolding factors increase: the increase is limited to 2% in the first pseudorapidity interval, $|\eta^\gamma| < 0.6$, where less material is present in ATLAS before the calorimeter, while it raises to 5% in the other two pseudorapidity ranges under study (see Figure 24). However, this increase is mostly an effect of the energy scale not being corrected at cal-
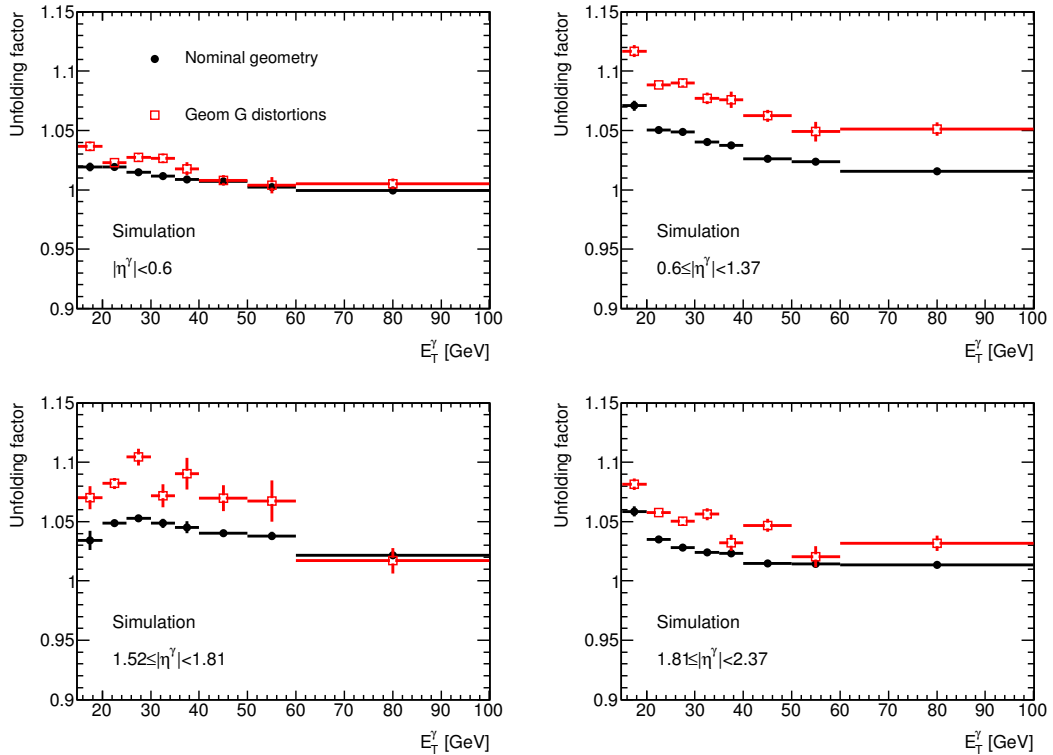

Figure 24: Bin-by-bin transverse energy unfolding factors as determined from a simulation of direct photons: nominal geometry (full black dots), and alternative geometry (ATLAS-GEO-10-08-00) with additional material in the inner detector, the calorymeter cryostat, and several services.

ibration level so with this check we are somehow counting twice the uncertainty on the unfolding factors due to the energy scale uncertainty. In order to remove this contribution, since we are only interested here in effects on the unfolding factors due to changes in the tails of the resolution, we repeat the check after correcting the reconstructed efficiencies using the mean shift in the energy resolution between the distorted and the nominal geometries. As shown in Figure 25, the unfolding factors vary by at most than 1% in all the pseudorapidity and transverse energy bins. When combined with the energy scale uncertainty, the uncertainty from the energy resolution therefore is negligible.
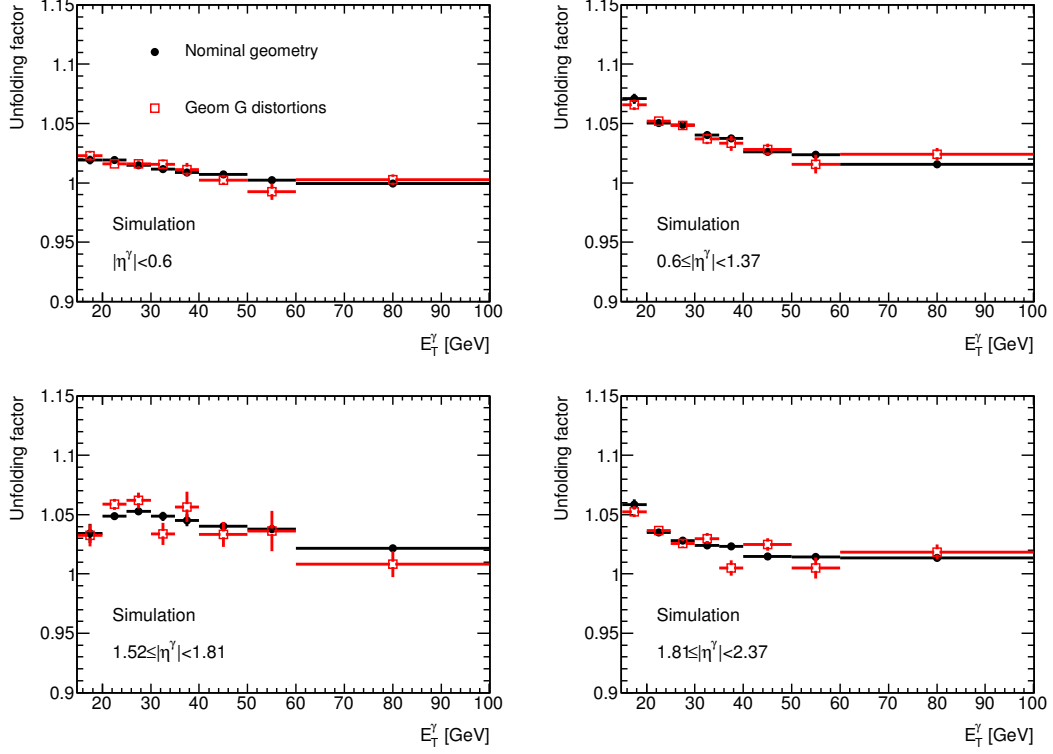
Figure 25: Bin-by-bin transverse energy unfolding factors as determined from a simulation of direct photons, after correcting the energy scale for the average energy loss in upstream material: nominal geometry (full black dots), and alternative geometry (ATLAS-GEO-10-08-00) with additional material in the inner detector, the calorymeter cryostat, and several services.

8.5   Signal yield stability over different run periods

Figure 26 shows the estimated signal yield for each run used in this analysis, divided by the integrated luminosity for that run. The estimated signal yield was computed by scaling each isolated, tight photon candidate in a given run by the average purity for all photons (in all runs) in the same bin of $(E_T, |\eta|)$. The signal yield per inverse nanobarn appears stable over the entire run range, with allowances for large uncertainties in runs with poor statistics.
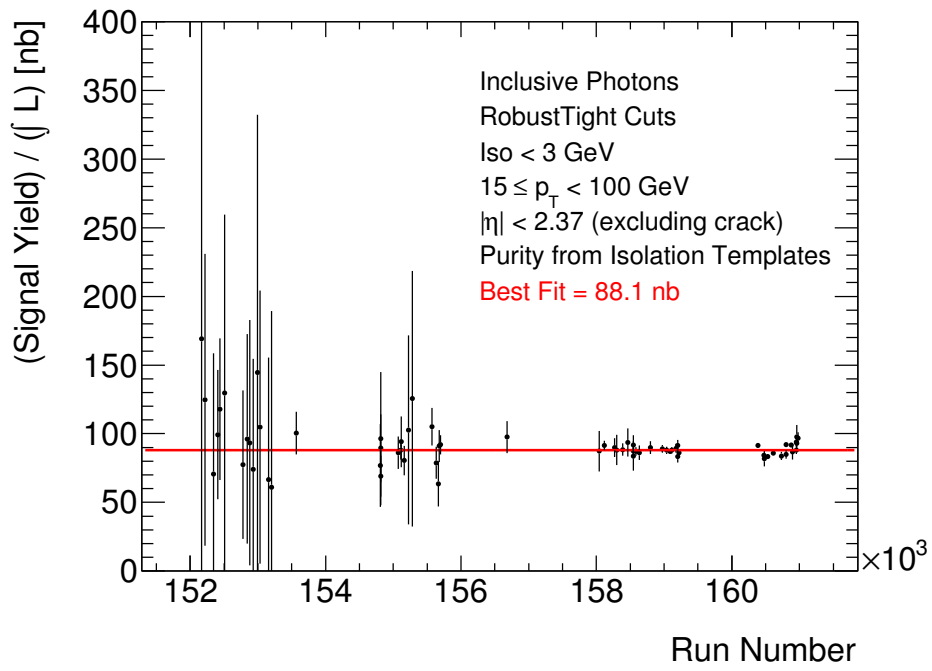
Figure 26: Background-subtracted estimates of signal candidates plotted by run number. The signal yield is computed with the isolation template method.

8.6 Cross section measurement after the inclusion of all systematic uncertainties

8.6.1 Results with the 2D sideband method

The final cross section measured using the two-dimensional sideband technique are listed in Tables 20-22. Correlated systematic uncertainties have been added linearly, uncorrelated uncertainties have been added in quadrature.

Table 20: The measured isolated prompt photon production cross section, for $0.00 \leq |\eta^\gamma| < 0.60$. The systematic uncertainties originating from the purity measurement, the photon selection, the photon energy scale, the unfolding procedure and the luminosity are shown. The total uncertainty includes both the statistical and all systematic uncertainties, except for the uncertainty on the luminosity. Results from the 2D sideband method.

E_T^γ	$\frac{d\sigma}{dE_T^\gamma}$	stat	syst (purity)	syst (efficiency)	syst (en. scale)	syst (unfolding)	syst (luminosity)	total uncertainty
[GeV]	[nb/GeV]	[nb/GeV]	[nb/GeV]	[nb/GeV]	[nb/GeV]	[nb/GeV]	[nb/GeV]	[nb/GeV]
[15, 20)	5.24	±0.11	$^{+0.52}_{-0.88}$	±0.81	$^{+0.51}_{-0.46}$	±0.11	±0.58	$^{+1.3}_{-1.4}$
[20, 25)	1.88	±0.05	$^{+0.18}_{-0.20}$	±0.21	$^{+0.14}_{-0.14}$	±0.04	±0.21	±0.36
[25, 30)	0.88	±0.03	±0.07	±0.08	$^{+0.09}_{-0.08}$	±0.02	±0.10	$^{+0.16}_{-0.15}$
[30, 35)	0.461	±0.016	$^{+0.029}_{-0.019}$	±0.035	$^{+0.045}_{-0.046}$	±0.009	±0.05	±0.07
[35, 40)	0.254	±0.011	$^{+0.017}_{-0.015}$	±0.019	$^{+0.027}_{-0.025}$	±0.005	±0.028	±0.04
[40, 50)	0.115	±0.005	$^{+0.008}_{-0.006}$	±0.007	$^{+0.009}_{-0.009}$	±0.0023	±0.013	$^{+0.017}_{-0.016}$
[50, 60)	0.050	±0.003	$^{+0.003}_{-0.002}$	±0.003	$^{+0.006}_{-0.005}$	±0.001	±0.005	$^{+0.008}_{-0.007}$
[60, 100)	0.0120	±0.0007	$^{+0.0007}_{-0.0005}$	±0.0006	$^{+0.0013}_{-0.0012}$	±0.0002	±0.0013	$^{+0.0019}_{-0.0018}$

Table 21: The measured isolated prompt photon production cross section, for $0.60 \leq |\eta^\gamma| < 1.37$. The systematic uncertainties originating from the purity measurement, the photon selection, the photon energy scale, the unfolding procedure and the luminosity are shown. The total uncertainty includes both the statistical and all systematic uncertainties, except for the uncertainty on the luminosity. Results from the 2D sideband method.

E_T^γ	$\frac{d\sigma}{dE_T^\gamma}$	stat	syst (purity)	syst (efficiency)	syst (en. scale)	syst (unfolding)	syst (luminosity)	total uncertainty
[GeV]	[nb/GeV]	[nb/GeV]	[nb/GeV]	[nb/GeV]	[nb/GeV]	[nb/GeV]	[nb/GeV]	[nb/GeV]
[15, 20)	5.9	±0.2	$^{+1.8}_{-0.5}$	±1.0	$^{+0.6}_{-0.5}$	±0.1	±0.6	$^{+2.3}_{-1.4}$
[20, 25)	2.23	±0.07	$^{+0.49}_{-0.18}$	±0.28	$^{+0.16}_{-0.16}$	±0.04	±0.24	$^{+0.6}_{-0.4}$
[25, 30)	1.05	±0.03	$^{+0.16}_{-0.06}$	±0.10	$^{+0.10}_{-0.10}$	±0.021	±0.12	$^{+0.24}_{-0.19}$
[30, 35)	0.52	±0.02	$^{+0.06}_{-0.03}$	±0.04	$^{+0.05}_{-0.05}$	±0.011	±0.06	$^{+0.11}_{-0.09}$
[35, 40)	0.313	±0.014	$^{+0.029}_{-0.021}$	±0.024	$^{+0.035}_{-0.032}$	±0.006	±0.034	$^{+0.06}_{-0.05}$
[40, 50)	0.146	±0.006	$^{+0.014}_{-0.011}$	±0.009	$^{+0.013}_{-0.013}$	±0.003	±0.016	$^{+0.025}_{-0.022}$
[50, 60)	0.062	±0.004	$^{+0.005}_{-0.004}$	±0.003	$^{+0.006}_{-0.006}$	±0.001	±0.007	$^{+0.010}_{-0.009}$
[60, 100)	0.0138	±0.0008	$^{+0.0013}_{-0.0009}$	±0.0007	$^{+0.0016}_{-0.0014}$	±0.0003	±0.0015	$^{+0.0025}_{-0.0022}$

Table 22: The measured isolated prompt photon production cross section, for $1.52 \leq |\eta^\gamma| < 1.81$. The systematic uncertainties originating from the purity measurement, the photon selection, the photon energy scale, the unfolding procedure and the luminosity are shown. The total uncertainty includes both the statistical and all systematic uncertainties, except for the uncertainty on the luminosity. Results from the 2D sideband method.

E_T^γ	$\frac{d\sigma}{dE_T^\gamma}$	stat	syst (purity)	syst (efficiency)	syst (en. scale)	syst (unfolding)	syst (luminosity)	total uncertainty
[GeV]	[nb/GeV]	[nb/GeV]	[nb/GeV]	[nb/GeV]	[nb/GeV]	[nb/GeV]	[nb/GeV]	[nb/GeV]
$[15, 20)$	2.9	±0.1	$^{+0.8}_{-0.3}$	±0.5	$^{+0.3}_{-0.3}$	±0.1	±0.3	$^{+1.1}_{-0.7}$
$[20, 25)$	1.12	±0.04	$^{+0.15}_{-0.08}$	±0.16	$^{+0.08}_{-0.08}$	±0.02	±0.12	$^{+0.27}_{-0.24}$
$[25, 30)$	0.47	±0.02	$^{+0.06}_{-0.04}$	±0.05	$^{+0.05}_{-0.04}$	±0.01	±0.05	$^{+0.11}_{-0.09}$
$[30, 35)$	0.240	±0.013	$^{+0.028}_{-0.016}$	±0.023	$^{+0.025}_{-0.026}$	±0.005	±0.026	$^{+0.052}_{-0.045}$
$[35, 40)$	0.142	±0.009	$^{+0.018}_{-0.010}$	±0.012	$^{+0.014}_{-0.013}$	±0.0032	±0.016	$^{+0.030}_{-0.026}$
$[40, 50)$	0.062	±0.004	$^{+0.005}_{-0.004}$	±0.005	$^{+0.006}_{-0.006}$	±0.0013	±0.007	$^{+0.011}_{-0.010}$
$[50, 60)$	0.0237	±0.0025	$^{+0.0026}_{-0.0028}$	±0.0019	$^{+0.0024}_{-0.0022}$	±0.0005	±0.003	±0.005
$[60, 100)$	0.0066	±0.0005	$^{+0.0005}_{-0.0003}$	±0.0005	$^{+0.0008}_{-0.0007}$	±0.0002	±0.0007	$^{+0.0013}_{-0.0012}$

8.6.2 Results with the template fit method

The final cross section measured using the two-dimensional sideband technique are listed in Tables 23-25. Correlated systematic uncertainties have been added linearly, uncorrelated uncertainties have been added in quadrature.

Table 23: Measured isolated prompt photon production cross section. The various systematic uncertainties originating from the purity measurement, the photon selection, the photon energy scale and the luminosity are shown. The total uncertainty includes the statistical one and all systematic uncertainties except the contribution from the luminosity uncertainty. Photons are required to be in the pseudorapidity range $0.00 \leq |\eta^\gamma| < 0.60$. Results from the template fit method.

E_T min	E_T max	$\frac{d\sigma}{dE_T^\gamma}$	stat	syst (purity)	syst (efficiency)	syst (escale)	syst (unfolding)	syst (lumi)	tot
[GeV]	[GeV]	[nb/GeV]	[nb/GeV]	[nb/GeV]	[nb/GeV]	[nb/GeV]	[nb/GeV]	[nb/GeV]	[nb/GeV]
15.0	20.0	4.8286	±0.0814	$^{+0.8164}_{-0.8164}$	$^{+0.7120}_{-0.7120}$	$^{+0.4701}_{-0.4198}$	±0.0980	±0.5317	$^{+1.1877}_{-1.1687}$
20.0	25.0	1.8276	±0.0386	$^{+0.1853}_{-0.1853}$	$^{+0.1905}_{-0.1905}$	$^{+0.1352}_{-0.1332}$	±0.0366	±0.2013	$^{+0.3029}_{-0.3020}$
25.0	30.0	0.8536	±0.0226	$^{+0.0756}_{-0.0756}$	$^{+0.0719}_{-0.0719}$	$^{+0.0837}_{-0.0770}$	±0.0172	±0.0940	$^{+0.1368}_{-0.1328}$
30.0	35.0	0.4525	±0.0144	$^{+0.0148}_{-0.0148}$	$^{+0.0304}_{-0.0304}$	$^{+0.0443}_{-0.0455}$	±0.0092	±0.0498	$^{+0.0583}_{-0.0592}$
35.0	40.0	0.2509	±0.0104	$^{+0.0163}_{-0.0163}$	$^{+0.0155}_{-0.0155}$	$^{+0.0271}_{-0.0246}$	±0.0052	±0.0276	$^{+0.0371}_{-0.0353}$
40.0	50.0	0.1158	±0.0048	$^{+0.0091}_{-0.0091}$	$^{+0.0059}_{-0.0059}$	$^{+0.0094}_{-0.0094}$	±0.0024	±0.0127	$^{+0.0153}_{-0.0153}$
50.0	60.0	0.0489	±0.0029	$^{+0.0028}_{-0.0028}$	$^{+0.0021}_{-0.0021}$	$^{+0.0057}_{-0.0052}$	±0.0010	±0.0054	$^{+0.0073}_{-0.0070}$
60.0	100.0	0.0122	±0.0007	$^{+0.0005}_{-0.0005}$	$^{+0.0004}_{-0.0004}$	$^{+0.0014}_{-0.0012}$	±0.0003	±0.0013	$^{+0.0017}_{-0.0016}$

Table 24: Measured isolated prompt photon production cross section. The various systematic uncertainties originating from the purity measurement, the photon selection, the photon energy scale and the luminosity are shown. The total uncertainty includes the statistical one and all systematic uncertainties except the contribution from the luminosity uncertainty. Photons are required to be in the pseudorapidity range $0.60 \leq |\eta^\gamma| < 1.37$. Results from the template fit method.

E_T min	E_T max	$\frac{d\sigma}{dE_T^\gamma}$	stat	syst (purity)	syst (efficiency)	syst (escale)	syst (unfolding)	syst (lumi)	tot
[GeV]	[GeV]	[nb/GeV]	[nb/GeV]	[nb/GeV]	[nb/GeV]	[nb/GeV]	[nb/GeV]	[nb/GeV]	[nb/GeV]
15.0	20.0	5.4598	±0.1048	+1.4205 −1.4205	+0.8662 −0.8662	+0.5479 −0.4837	±0.1109	±0.6012	+1.7583 −1.7393
20.0	25.0	2.1839	±0.0469	+0.4097 −0.4097	+0.2595 −0.2595	+0.1607 −0.1587	±0.0438	±0.2405	+0.5149 −0.5143
25.0	30.0	1.0277	±0.0264	+0.0917 −0.0917	+0.0927 −0.0927	+0.0965 −0.0958	±0.0207	±0.1132	+0.1657 −0.1653
30.0	35.0	0.5009	±0.0170	+0.0328 −0.0328	+0.0363 −0.0363	+0.0506 −0.0488	±0.0102	±0.0552	+0.0731 −0.0719
35.0	40.0	0.3065	±0.0118	+0.0220 −0.0220	+0.0203 −0.0203	+0.0344 −0.0311	±0.0063	±0.0338	+0.0475 −0.0452
40.0	50.0	0.1423	±0.0055	+0.0079 −0.0079	+0.0078 −0.0078	+0.0124 −0.0125	±0.0029	±0.0157	+0.0178 −0.0178
50.0	60.0	0.0631	±0.0033	+0.0017 −0.0017	+0.0024 −0.0024	+0.0064 −0.0060	±0.0013	±0.0069	+0.0079 −0.0076
60.0	100.0	0.0155	±0.0008	+0.0007 −0.0007	+0.0006 −0.0006	+0.0018 −0.0016	±0.0003	±0.0017	+0.0022 −0.0020

Table 25: Measured isolated prompt photon production cross section. The various systematic uncertainties originating from the purity measurement, the photon selection, the photon energy scale and the luminosity are shown. The total uncertainty includes the statistical one and all systematic uncertainties except the contribution from the luminosity uncertainty. Photons are required to be in the pseudorapidity range $1.52 \leq |\eta^\gamma| < 1.81$. Results from the template fit method.

E_T min	E_T max	$\frac{d\sigma}{dE_T^\gamma}$	stat	syst (purity)	syst (efficiency)	syst (escale)	syst (unfolding)	syst (lumi)	tot
[GeV]	[GeV]	[nb/GeV]	[nb/GeV]	[nb/GeV]	[nb/GeV]	[nb/GeV]	[nb/GeV]	[nb/GeV]	[nb/GeV]
15.0	20.0	2.8065	±0.0613	+0.5395 −0.5395	+0.4762 −0.4762	+0.2617 −0.2516	±0.0596	±0.3090	+0.7705 −0.7671
20.0	25.0	1.0625	±0.0296	+0.0903 −0.0903	+0.1506 −0.1506	+0.0773 −0.0765	±0.0214	±0.1170	+0.1954 −0.1950
25.0	30.0	0.4519	±0.0170	+0.0388 −0.0388	+0.0481 −0.0481	+0.0439 −0.0393	±0.0093	±0.0498	+0.0782 −0.0757
30.0	35.0	0.2238	±0.0107	+0.0203 −0.0203	+0.0199 −0.0199	+0.0234 −0.0241	±0.0047	±0.0246	+0.0386 −0.0391
35.0	40.0	0.1361	±0.0078	+0.0172 −0.0172	+0.0107 −0.0107	+0.0137 −0.0125	±0.0031	±0.0150	+0.0259 −0.0252
40.0	50.0	0.0605	±0.0035	+0.0042 −0.0042	+0.0046 −0.0046	+0.0058 −0.0057	±0.0013	±0.0067	+0.0093 −0.0092
50.0	60.0	0.0230	±0.0022	+0.0022 −0.0022	+0.0016 −0.0016	+0.0023 −0.0021	±0.0005	±0.0025	+0.0043 −0.0042
60.0	100.0	0.0065	±0.0005	+0.0005 −0.0005	+0.0004 −0.0004	+0.0008 −0.0007	±0.0001	±0.0007	+0.0012 −0.0011

9 Theoretical predictions

9.1 Isolated prompt photon production QCD cross section

The expected isolated prompt photon production cross section as a function of the photon transverse energy E_T^γ has been estimated, separately for the various photon pseudorapidity ranges under study, by means of the JETPHOX Monte Carlo program [4], which implements a full NLO QCD calculation of both the direct and fragmentation contributions to the total cross section. A parton level isolation cut, requiring a total transverse energy below 4 GeV from the partons produced with the photon inside a cone of radius $\Delta R = \sqrt{\Delta\eta^2 + \Delta\phi^2} = 0.4$ in $\eta \times \phi$ around the photon direction, has been used for this computation. The NLO photon fragmentation function [33] and the CTEQ 6.6 parton density functions [34] provided by the LHAPDF package [35] have been used. The nominal renormalization (μ_R), factorization (μ_F) and fragmentation (μ_f) scales have been set to the photon transverse energy E_T^γ. The resulting distributions are shown in Figs. 27. The expected cross sections with their uncertainties in the pseudorapidity ranges under study are summarized in Tables 26, 27, 28. The systematic uncertainties on the QCD cross sections are estimated in the following way:

- the scale uncertainty has been evaluated by varying the three scales independently between 0.5 and 2.0 times the nominal scale. This leads to a change of the predicted cross section between 20% at low E_T and 10% at high E_T.

- the uncertainty on the cross section from the PDF uncertainty has been obtained by varing the PDFs within the 68% C.L. intervals. The corresponding uncertainty on the cross section varies between 5% and 2% as E_T increases between 15 and 100 GeV.

- the uncertainty on the parton level isolation cut has been evaluated by varying the cut between 2 and 6 GeV. This changes the predicted cross section by 2% at most.

The NLO calculation provided by JETPHOX predicts a cross section at parton level, which does not include effects of hadronization nor the underlying event and pileup (*i.e.* multiple proton-proton interactions in the same bunch crossing). The non-perturbative effects on the cross section due to hadronization are evaluated using the simulated PYTHIA signal samples described in Section 3.2. They are estimated to be within 1% of unity for all E_T and η regions under study. To account for the effect of the underlying event and pileup on the measured isolation energy, a correction to the photon transverse isolation energy measured in data is applied, using a procedure described in Section 4.4.

For comparison the expected cross section using the MSTW 2008 PDFs are shown in Figure 28 and Tables 29, 30, 31. The central values obtained with the MSTW 2008 PDFs are between 3 and 5% higher than those predicted using the CTEQ 6.6 PDFs

More details on the estimate of the theoretical isolated prompt photon production cross section are available in [27].
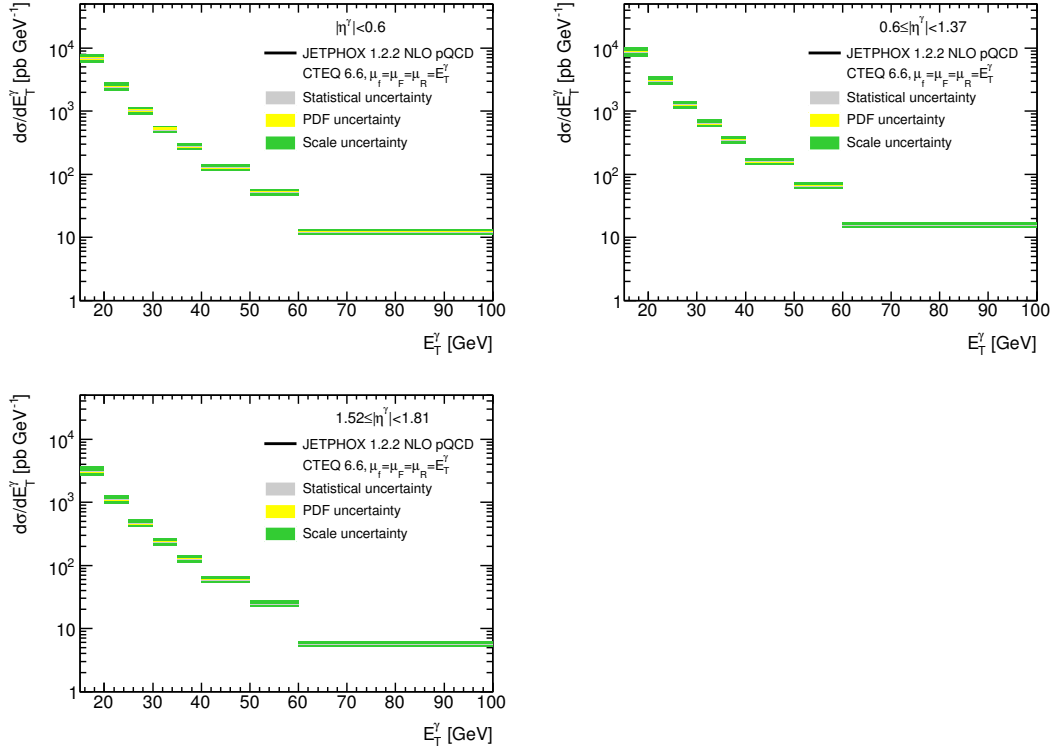
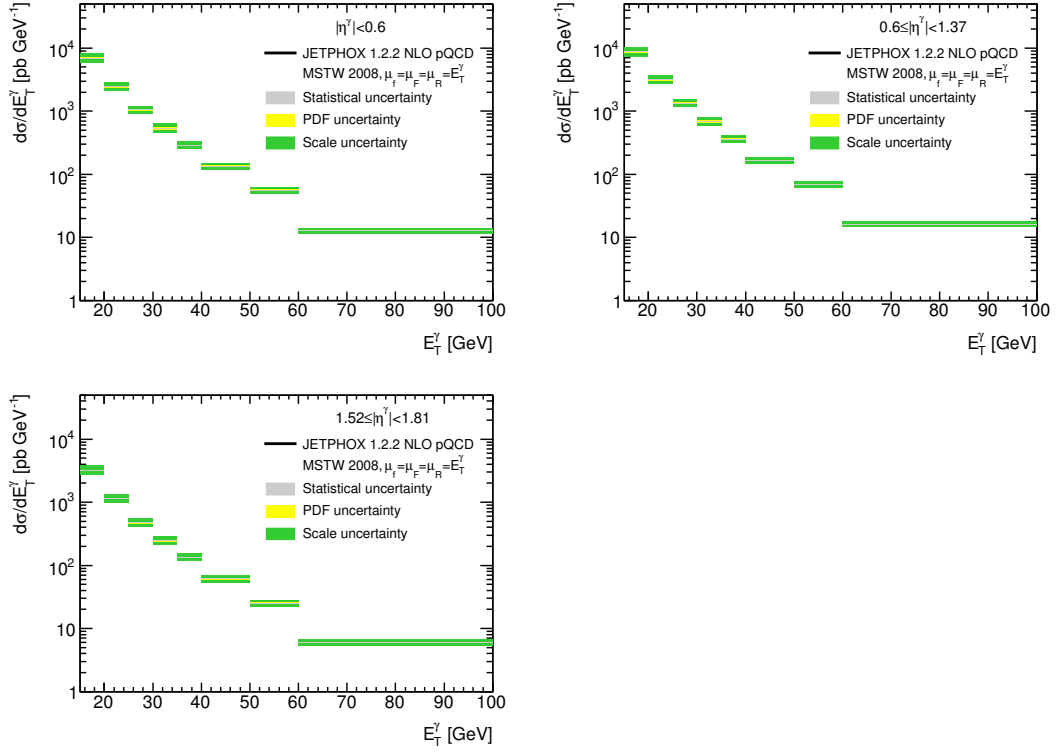Figure 27: Inclusive prompt photon production cross section expected from QCD using the next-to-leading order (NLO) JETPHOX computation, for photons with transverse energies above 15 GeV and in different pseudorapidity ranges. The CTEQ 6.6 PDFs have been used in the calculation. Top left: $|\eta^\gamma| < 0.6$. Top right: $0.6 \le |\eta^\gamma| < 1.37$. Bottom left: $1.52 \le |\eta^\gamma| < 1.81$.

Table 26: NLO pQCD isolated prompt photon production cross section computed with `JETPHOX` 1.2.2 using CTEQ 6.6 PDFs. Photons are required to be in the pseudorapidity range $0.00 \leq |\eta^\gamma| < 0.60$. The nominal factorization, fragmentation and renormalization scales are set to the photon transverse energy ($\mu_f = \mu_F = \mu_R = E_T^\gamma$). Scale errors are evaluated by varying the three scales independently between $0.5E_T^\gamma$ and $2.0E_T^\gamma$. PDF errors correspond to 68% CL PDF uncertainties.

E_T min [GeV]	E_T max [GeV]	$\frac{d\sigma}{dE_T^\gamma}$ [nb/GeV]	stat [nb/GeV]	scale [nb/GeV]	PDF [nb/GeV]	isolation [nb/GeV]	tot [nb/GeV]
15.0	20.0	6.7797	±0.0143	+1.3020 −0.9094	+0.3463 −0.1881	±0.1356	+1.3540 −0.9385
20.0	25.0	2.3839	±0.0086	+0.4329 −0.2930	+0.0992 −0.0587	±0.0477	+0.4466 −0.3026
25.0	30.0	1.0109	±0.0057	+0.1666 −0.1229	+0.0493 −0.0390	±0.0202	+0.1749 −0.1305
30.0	35.0	0.5045	±0.0040	+0.0841 −0.0441	+0.0558 −0.0045	±0.0101	+0.1015 −0.0455
35.0	40.0	0.2774	±0.0008	+0.0405 −0.0306	+0.0068 −0.0112	±0.0055	+0.0414 −0.0330
40.0	50.0	0.1273	±0.0008	+0.0167 −0.0133	+0.0047 −0.0035	±0.0025	+0.0175 −0.0140
50.0	60.0	0.0515	±0.0005	+0.0065 −0.0052	+0.0013 −0.0013	±0.0010	+0.0067 −0.0055
60.0	100.0	0.0121	±0.0002	+0.0014 −0.0011	+0.0003 −0.0003	±0.0002	+0.0014 −0.0012

Table 27: NLO pQCD isolated prompt photon production cross section computed with `JETPHOX` 1.2.2 using CTEQ 6.6 PDFs. Photons are required to be in the pseudorapidity range $0.60 \leq |\eta^\gamma| < 1.37$. The nominal factorization, fragmentation and renormalization scales are set to the photon transverse energy ($\mu_f = \mu_F = \mu_R = E_T^\gamma$). Scale errors are evaluated by varying the three scales independently between $0.5E_T^\gamma$ and $2.0E_T^\gamma$. PDF errors correspond to 68% CL PDF uncertainties.

E_T min [GeV]	E_T max [GeV]	$\frac{d\sigma}{dE_T^\gamma}$ [nb/GeV]	stat [nb/GeV]	scale [nb/GeV]	PDF [nb/GeV]	isolation [nb/GeV]	tot [nb/GeV]
15.0	20.0	8.5265	±0.0179	+1.6483 −1.2427	+0.2593 −0.3297	±0.1705	+1.6773 −1.2969
20.0	25.0	3.0013	±0.0107	+0.5360 −0.3827	+0.0980 −0.0882	±0.0600	+0.5481 −0.3973
25.0	30.0	1.2768	±0.0071	+0.1768 −0.1536	+0.0349 −0.0540	±0.0255	+0.1820 −0.1648
30.0	35.0	0.6409	±0.0050	+0.1058 −0.0815	+0.0216 −0.0213	±0.0128	+0.1088 −0.0852
35.0	40.0	0.3443	±0.0010	+0.0510 −0.0380	+0.0102 −0.0081	±0.0069	+0.0525 −0.0394
40.0	50.0	0.1609	±0.0009	+0.0213 −0.0179	+0.0023 −0.0062	±0.0032	+0.0217 −0.0193
50.0	60.0	0.0653	±0.0006	+0.0090 −0.0065	+0.0020 −0.0009	±0.0013	+0.0094 −0.0067
60.0	100.0	0.0154	±0.0003	+0.0018 −0.0015	+0.0003 −0.0003	±0.0003	+0.0019 −0.0015

Table 28: NLO pQCD isolated prompt photon production cross section computed with JETPHOX 1.2.2 using CTEQ 6.6 PDFs. Photons are required to be in the pseudorapidity range $1.52 \leq |\eta^\gamma| < 1.81$. The nominal factorization, fragmentation and renormalization scales are set to the photon transverse energy ($\mu_f = \mu_F = \mu_R = E_T^\gamma$). Scale errors are evaluated by varying the three scales independently between $0.5E_T^\gamma$ and $2.0E_T^\gamma$. PDF errors correspond to 68% CL PDF uncertainties.

E_T min	E_T max	$\frac{d\sigma}{dE_T^\gamma}$	stat	scale	PDF	isolation	tot
[GeV]	[GeV]	[nb/GeV]	[nb/GeV]	[nb/GeV]	[nb/GeV]	[nb/GeV]	[nb/GeV]
15.0	20.0	3.0809	±0.0064	+0.6079 −0.4352	+0.0898 −0.1037	±0.0616	+0.6176 −0.4515
20.0	25.0	1.0974	±0.0039	+0.1922 −0.1430	+0.0290 −0.0293	±0.0219	+0.1957 −0.1476
25.0	30.0	0.4609	±0.0026	+0.0727 −0.0583	+0.0121 −0.0110	±0.0092	+0.0742 −0.0600
30.0	35.0	0.2330	±0.0018	+0.0355 −0.0294	+0.0077 −0.0060	±0.0047	+0.0367 −0.0304
35.0	40.0	0.1259	±0.0003	+0.0193 −0.0148	+0.0030 −0.0031	±0.0025	+0.0197 −0.0153
40.0	50.0	0.0582	±0.0003	+0.0083 −0.0063	+0.0012 −0.0006	±0.0012	+0.0085 −0.0065
50.0	60.0	0.0243	±0.0002	+0.0032 −0.0025	+0.0002 −0.0007	±0.0005	+0.0033 −0.0027
60.0	100.0	0.0057	±0.0001	+0.0007 −0.0006	+0.0001 −0.0001	±0.0001	+0.0007 −0.0006

Table 29: NLO pQCD isolated prompt photon production cross section computed with JETPHOX 1.2.2 using MSTW 2008 PDFs. Photons are required to be in the pseudorapidity range $0.00 \leq |\eta^\gamma| < 0.60$. The nominal factorization, fragmentation and renormalization scales are set to the photon transverse energy ($\mu_f = \mu_F = \mu_R = E_T^\gamma$). Scale errors are evaluated by varying the three scales independently between $0.5E_T^\gamma$ and $2.0E_T^\gamma$. PDF errors correspond to 68% CL PDF uncertainties.

E_T min	E_T max	$\frac{d\sigma}{dE_T^\gamma}$	stat	scale	PDF	isolation	tot
[GeV]	[GeV]	[nb/GeV]	[nb/GeV]	[nb/GeV]	[nb/GeV]	[nb/GeV]	[nb/GeV]
15.0	20.0	6.9598	±0.0148	+1.3689 −1.0857	+0.1898 −0.1162	±0.1392	+1.3890 −1.1007
20.0	25.0	2.4806	±0.0090	+0.4436 −0.3413	+0.0243 −0.1082	±0.0496	+0.4470 −0.3615
25.0	30.0	1.0568	±0.0059	+0.1617 −0.1412	+0.0247 −0.0494	±0.0211	+0.1650 −0.1511
30.0	35.0	0.5365	±0.0042	+0.1069 −0.0729	+0.0309 −0.0157	±0.0107	+0.1118 −0.0753
35.0	40.0	0.2870	±0.0008	+0.0448 −0.0332	+0.0053 −0.0065	±0.0057	+0.0454 −0.0343
40.0	50.0	0.1341	±0.0008	+0.0175 −0.0148	+0.0013 −0.0041	±0.0027	+0.0178 −0.0156
50.0	60.0	0.0542	±0.0005	+0.0079 −0.0055	+0.0024 −0.0003	±0.0011	+0.0083 −0.0056
60.0	100.0	0.0128	±0.0002	+0.0015 −0.0012	+0.0001 −0.0002	±0.0003	+0.0015 −0.0013

Figure 28: Inclusive prompt photon production cross section expected from QCD using the next-to-leading order (NLO) `JETPHOX` computation, for photons with transverse energies above 15 GeV and in different pseudorapidity ranges. The MSTW 2008 PDFs have been used in the calculation. Top left: $|\eta^\gamma| < 0.6$. Top right: $0.6 \le |\eta^\gamma| < 1.37$. Bottom left: $1.52 \le |\eta^\gamma| < 1.81$.

Table 30: NLO pQCD isolated prompt photon production cross section computed with `JETPHOX` 1.2.2 using MSTW 2008 PDFs. Photons are required to be in the pseudorapidity range $0.60 \le |\eta^\gamma| < 1.37$. The nominal factorization, fragmentation and renormalization scales are set to the photon transverse energy ($\mu_f = \mu_F = \mu_R = E_T^\gamma$). Scale errors are evaluated by varying the three scales independently between $0.5E_T^\gamma$ and $2.0E_T^\gamma$. PDF errors correspond to 68% CL PDF uncertainties.

E_T min	E_T max	$\frac{d\sigma}{dE_T^\gamma}$	stat	scale	PDF	isolation	tot
[GeV]	[GeV]	[nb/GeV]	[nb/GeV]	[nb/GeV]	[nb/GeV]	[nb/GeV]	[nb/GeV]
15.0	20.0	8.7278	±0.0185	+1.7323 −1.3498	+0.1824 −0.2107	±0.1746	+1.7506 −1.3772
20.0	25.0	3.1223	±0.0112	+0.5681 −0.4068	+0.0414 −0.0695	±0.0624	+0.5731 −0.4174
25.0	30.0	1.3412	±0.0074	+0.2178 −0.1746	+0.0395 −0.0575	±0.0268	+0.2230 −0.1858
30.0	35.0	0.6733	±0.0053	+0.1132 −0.0871	+0.0412 −0.0177	±0.0135	+0.1212 −0.0899
35.0	40.0	0.3606	±0.0010	+0.0578 −0.0412	+0.0087 −0.0043	±0.0072	+0.0589 −0.0421
40.0	50.0	0.1680	±0.0010	+0.0228 −0.0192	+0.0011 −0.0052	±0.0034	+0.0231 −0.0201
50.0	60.0	0.0689	±0.0006	+0.0093 −0.0069	+0.0025 −0.0002	±0.0014	+0.0097 −0.0071
60.0	100.0	0.0162	±0.0003	+0.0020 −0.0016	+0.0001 −0.0002	±0.0003	+0.0020 −0.0016

Table 31: NLO pQCD isolated prompt photon production cross section computed with `JETPHOX` 1.2.2 using MSTW 2008 PDFs. Photons are required to be in the pseudorapidity range $1.52 \le |\eta^\gamma| < 1.81$. The nominal factorization, fragmentation and renormalization scales are set to the photon transverse energy ($\mu_f = \mu_F = \mu_R = E_T^\gamma$). Scale errors are evaluated by varying the three scales independently between $0.5E_T^\gamma$ and $2.0E_T^\gamma$. PDF errors correspond to 68% CL PDF uncertainties.

E_T min	E_T max	$\frac{d\sigma}{dE_T^\gamma}$	stat	scale	PDF	isolation	tot
[GeV]	[GeV]	[nb/GeV]	[nb/GeV]	[nb/GeV]	[nb/GeV]	[nb/GeV]	[nb/GeV]
15.0	20.0	3.1519	±0.0066	+0.6359 −0.4486	+0.0720 −0.0505	±0.0630	+0.6430 −0.4558
20.0	25.0	1.1332	±0.0040	+0.2095 −0.1567	+0.0213 −0.0259	±0.0227	+0.2118 −0.1604
25.0	30.0	0.4811	±0.0027	+0.0837 −0.0706	+0.0053 −0.0199	±0.0096	+0.0844 −0.0740
30.0	35.0	0.2446	±0.0019	+0.0460 −0.0319	+0.0083 −0.0058	±0.0049	+0.0470 −0.0327
35.0	40.0	0.1316	±0.0004	+0.0209 −0.0155	+0.0018 −0.0015	±0.0026	+0.0211 −0.0158
40.0	50.0	0.0611	±0.0004	+0.0091 −0.0073	+0.0005 −0.0013	±0.0012	+0.0092 −0.0075
50.0	60.0	0.0251	±0.0002	+0.0032 −0.0026	+0.0008 −0.0005	±0.0005	+0.0034 −0.0027
60.0	100.0	0.0059	±0.0001	+0.0008 −0.0006	+0.0001 −0.0000	±0.0001	+0.0008 −0.0006

9.2 Comparison between measurement and theory

9.2.1 2D sideband results

The measured E_T-differential cross-sections are plotted, with the theoretical cross-sections overlaid, for the different η regions, in figures 29, 30, and 31. Here the CTEQ66 PDFs have been used for computing the theoretical cross sections. Similar plots obtained by using the MSTW08 PDFs are shown in figures 32, 33, and 34. A ratio of data to theory is also plotted, showing the relative deviation of the measured cross section from the predicted cross section across the full E_T range on a linear scale. The error bars represent the combination of statistical and systematic uncertainties, but are dominated by systematic uncertainties in all regions. The luminosity uncertainty is plotted separately.
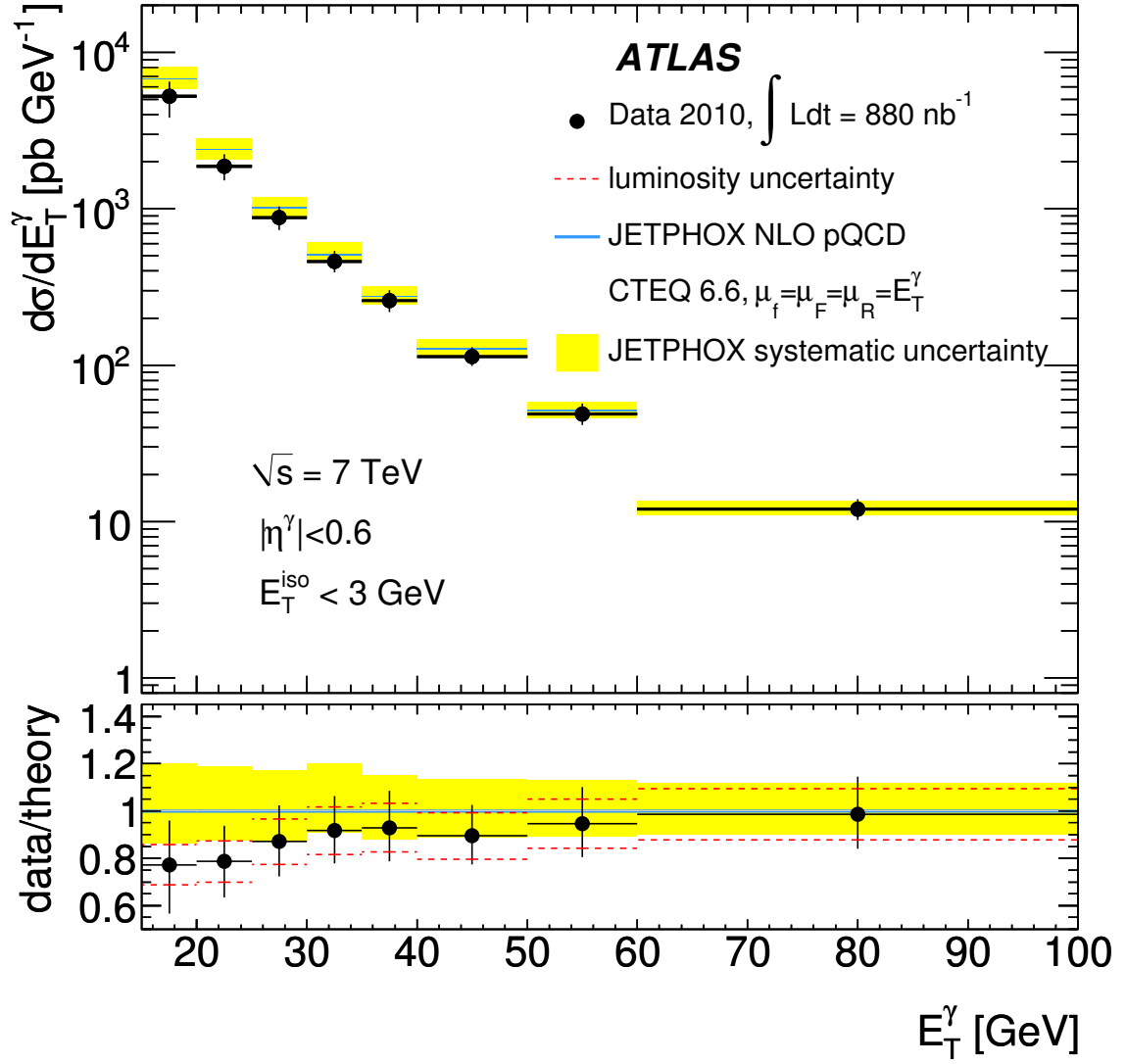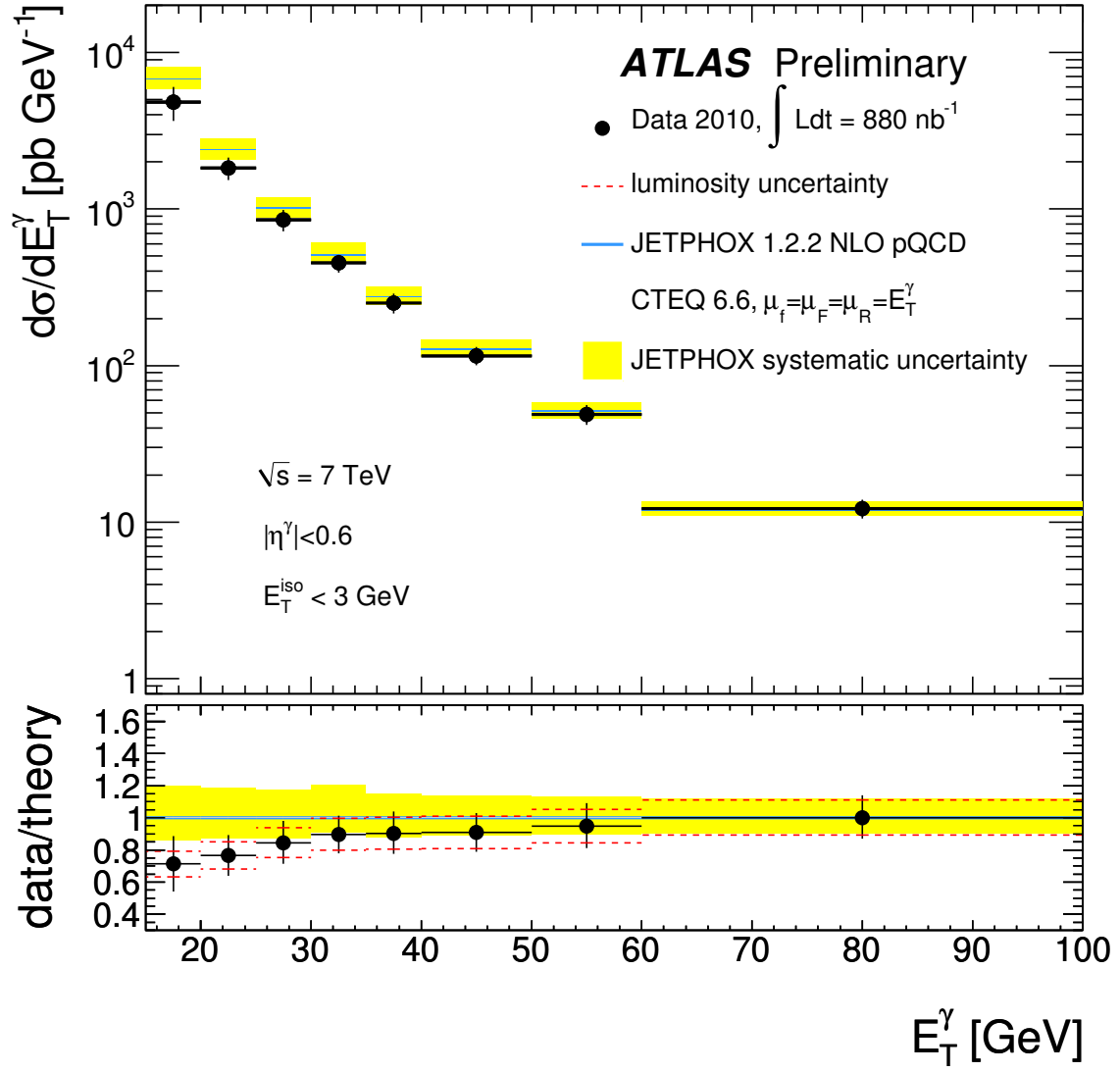
Figure 29: Measured vs expected inclusive prompt photon production cross section, for photons with transverse energies above 15 GeV and in the pseudorapidity range $|\eta^\gamma| < 0.6$. Results with the 2d sideband method. The CTEQ66 PDFs are used in the theoretical computation.
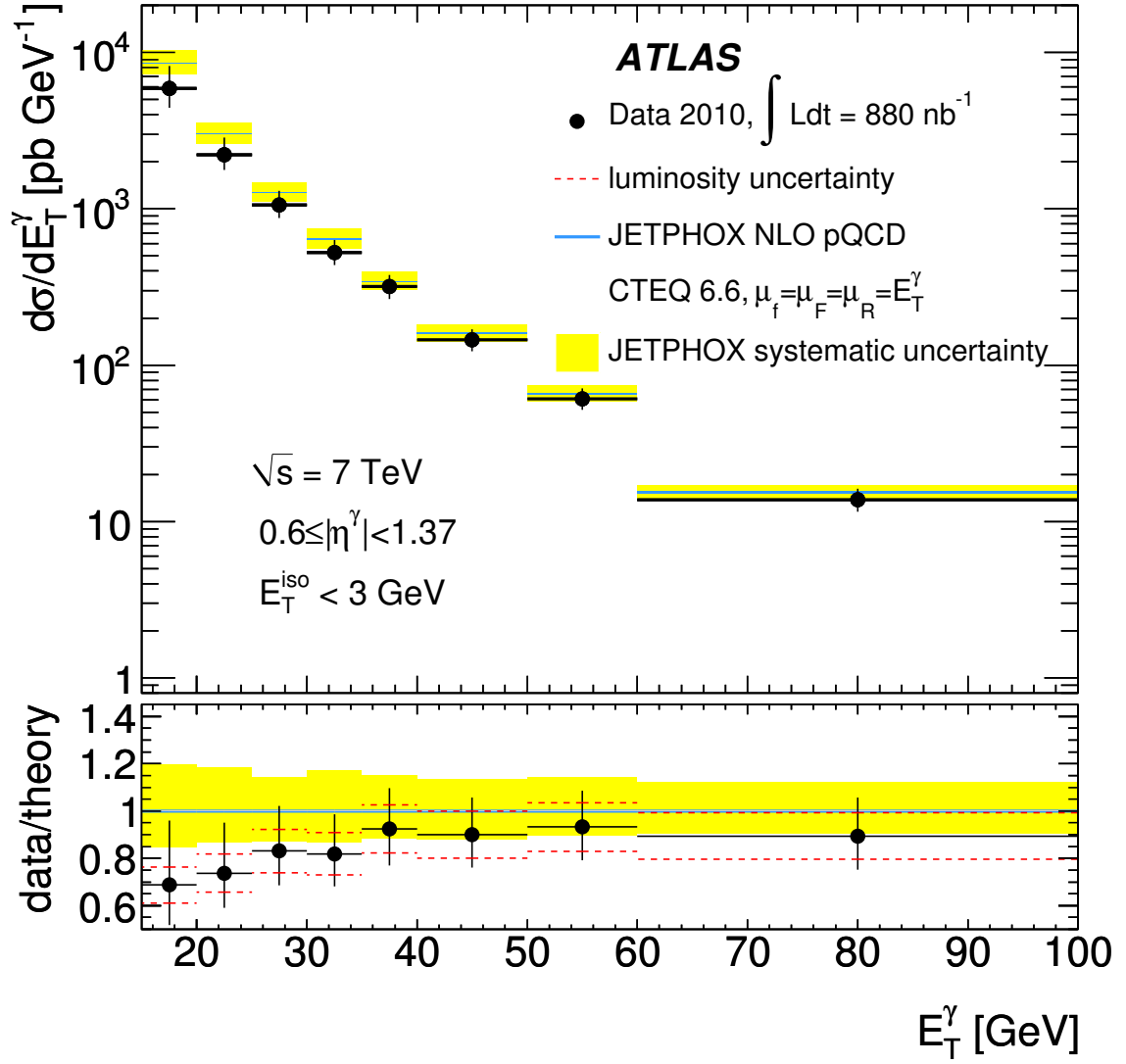
Figure 30: Measured vs expected inclusive prompt photon production cross section, for photons with transverse energies above 15 GeV and in the pseudorapidity range $0.6 \leq |\eta^{\gamma}| < 1.37$. Results with the 2d sideband method. The CTEQ PDFs are used in the theoretical computation.
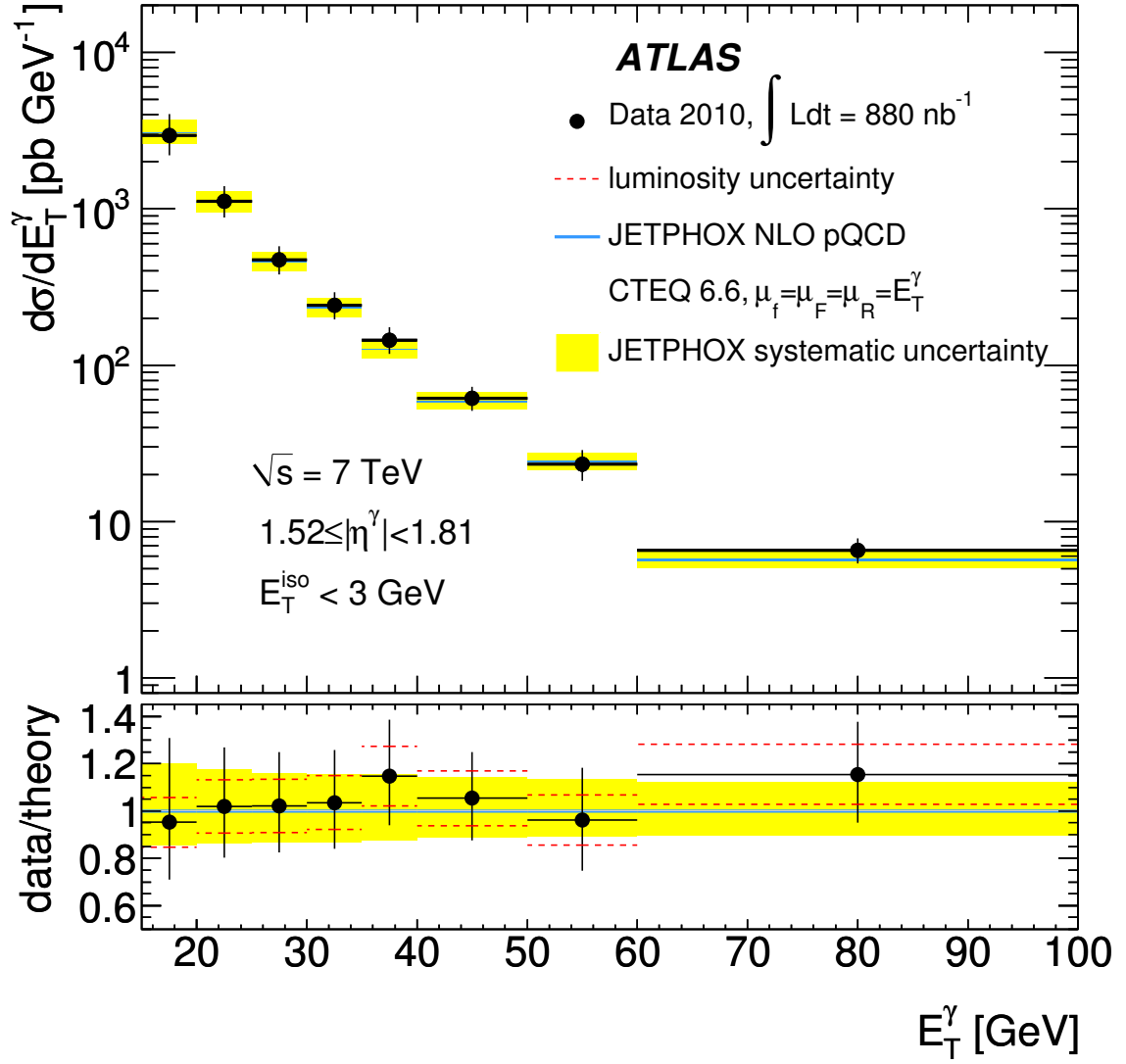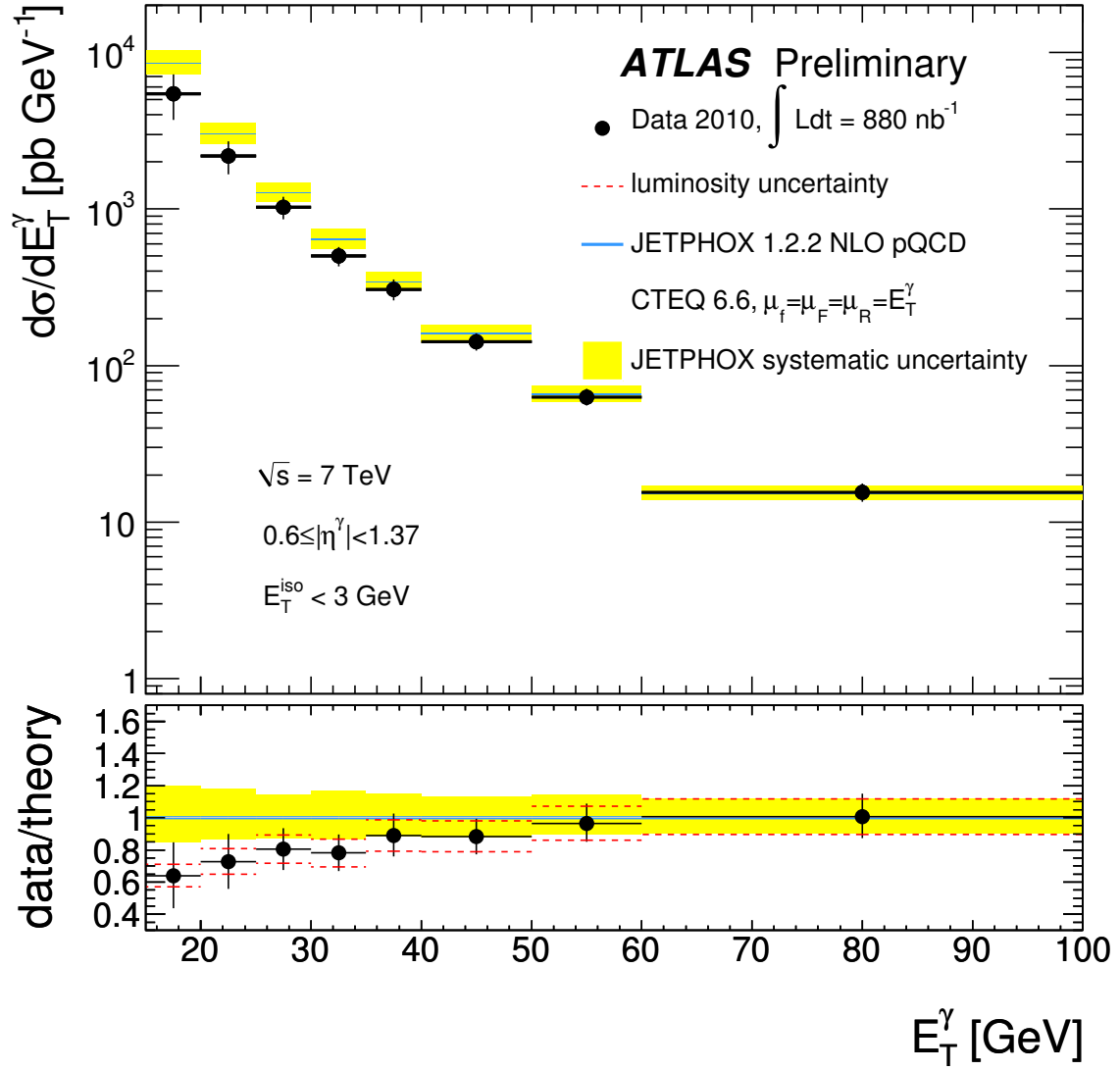
Figure 31: Measured vs expected inclusive prompt photon production cross section, for photons with transverse energies above 15 GeV and in the pseudorapidity range $1.52 \leq |\eta^\gamma| < 1.81$. Results with the 2d sideband method. The CTEQ66 PDFs are used in the theoretical computation.
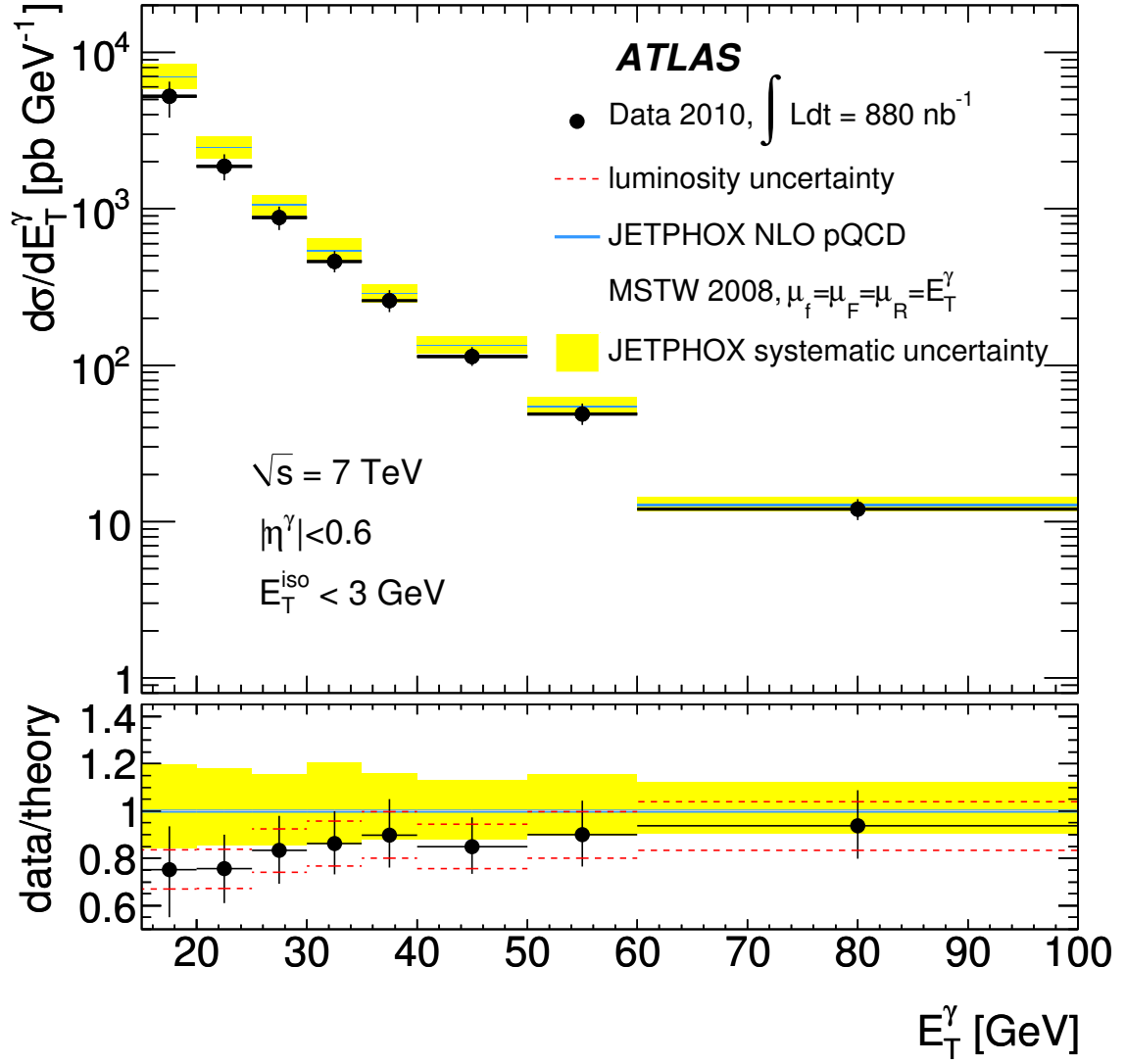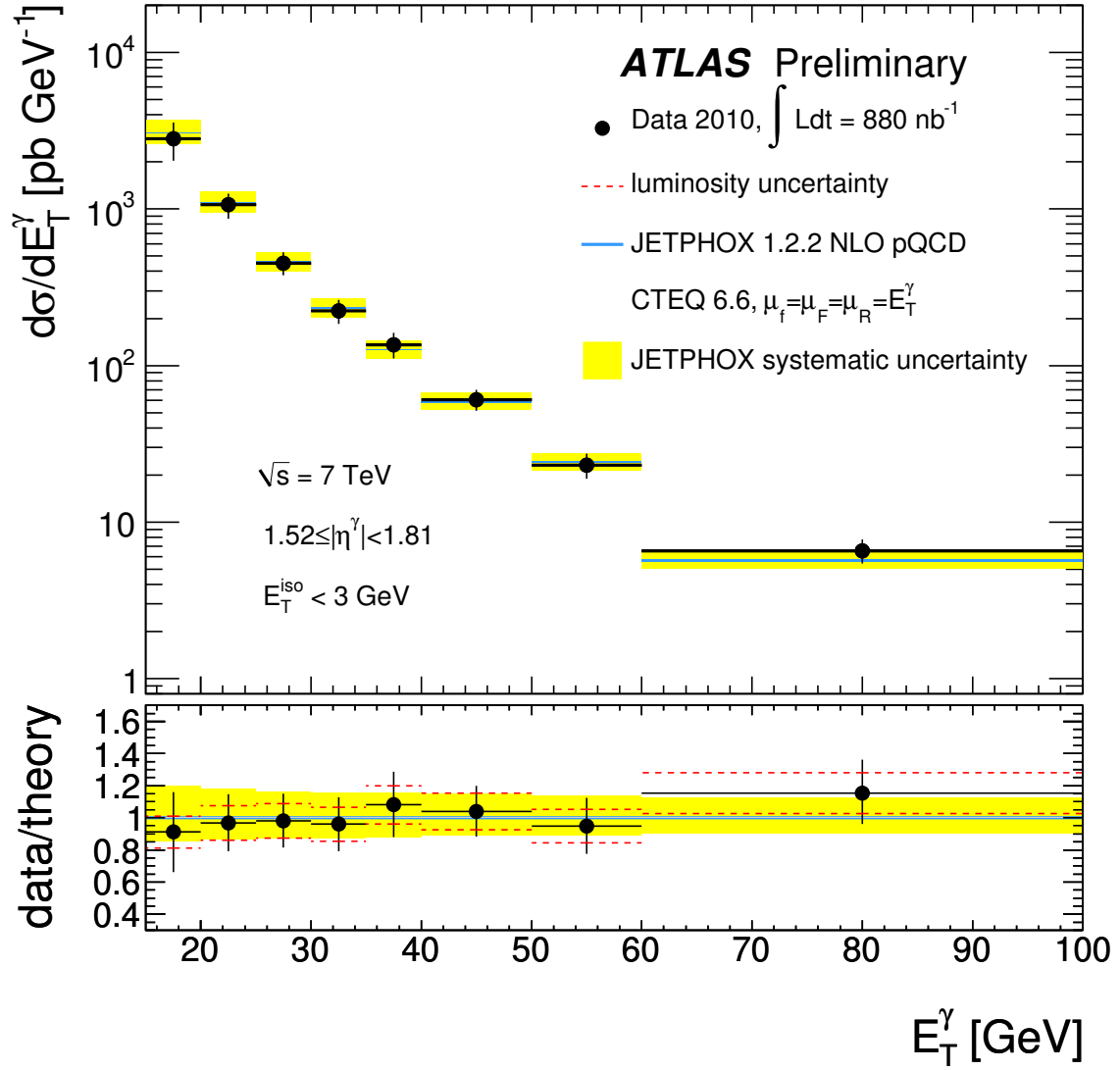
Figure 32: Measured vs expected inclusive prompt photon production cross section, for photons with transverse energies above 15 GeV and in the pseudorapidity range $|\eta^\gamma| < 0.6$. Results with the 2d sideband method. The MSTW08 PDFs are used in the theoretical computation.
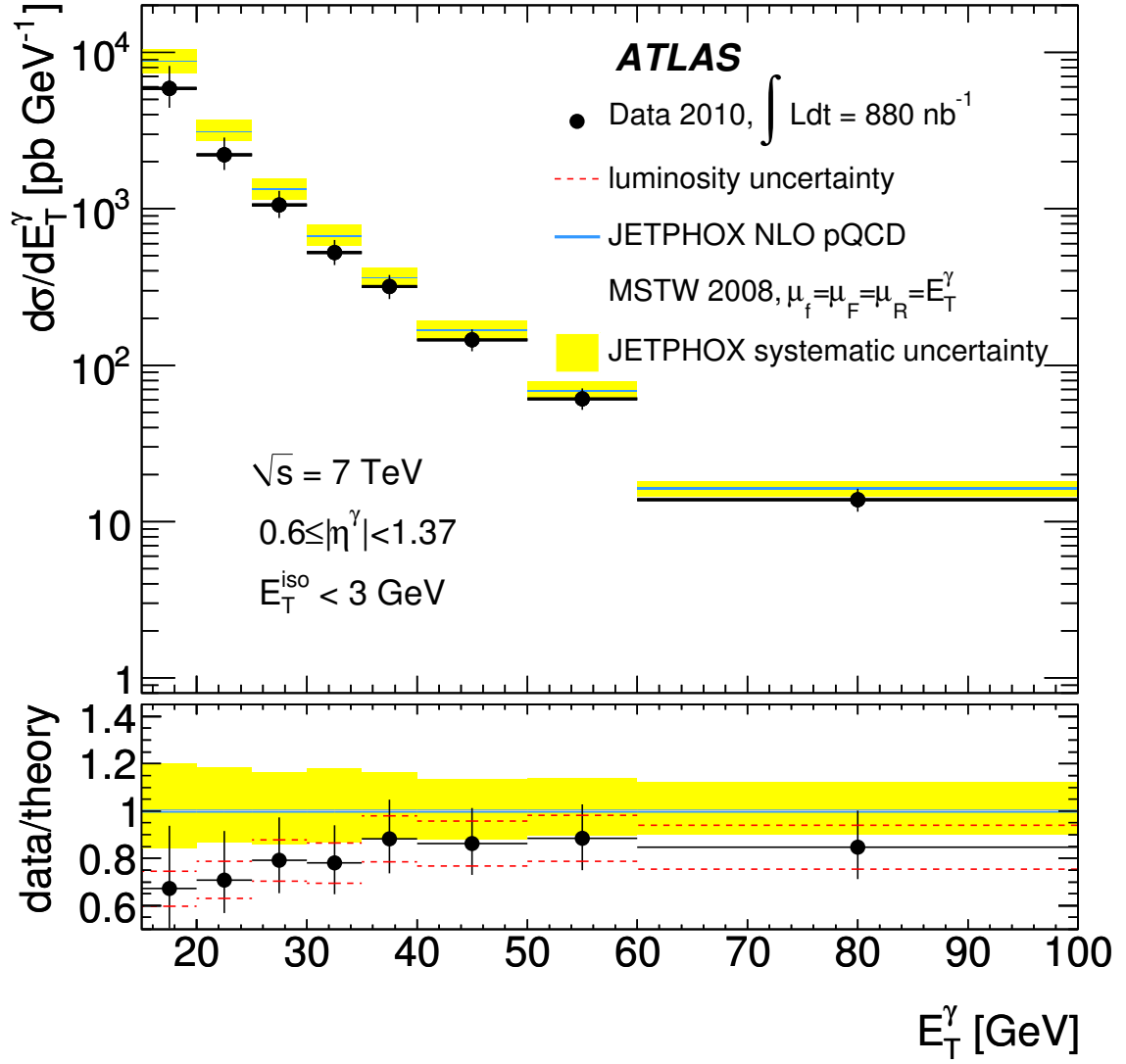
Figure 33: Measured vs expected inclusive prompt photon production cross section, for photons with transverse energies above 15 GeV and in the pseudorapidity range $0.6 \leq |\eta^\gamma| < 1.37$. Results with the 2d sideband method. The MSTW08 PDFs are used in the theoretical computation.
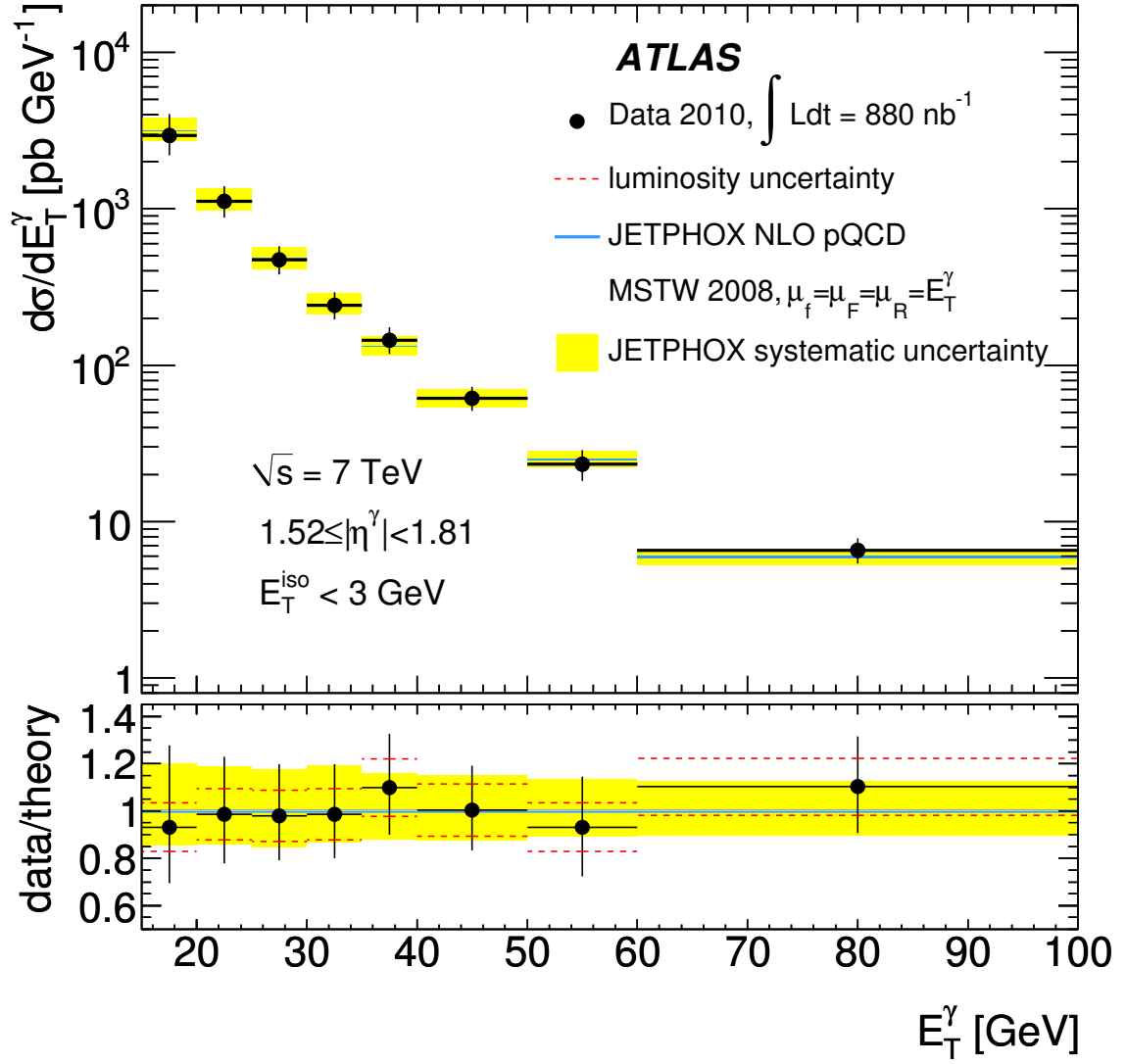
Figure 34: Measured vs expected inclusive prompt photon production cross section, for photons with transverse energies above 15 GeV and in the pseudorapidity range $1.52 \leq |\eta^\gamma| < 1.81$. Results with the 2d sideband method. The MSTW08 PDFs are used in the theoretical computation.

9.2.2 Template fit results

The measured E_{T}-differential cross-sections are plotted with the theoretical cross-sections for the different η regions in figures 35, 36, and 37. The CTEQ66 PDFs have been used for computing the theoretical cross sections. A ratio of data to theory is also plotted, showing the relative deviation of the measured cross section from the predicted cross section across the full E_{T} range on a linear scale. The error bars represent the combination of statistical and systematic uncertainties, but are dominated by the systematic ones in all regions. The luminosity uncertainty is plotted separately.

Figure 35: Measured vs expected inclusive prompt photon production cross section, for photons with transverse energies above 15 GeV and in the pseudorapidity range $|\eta^\gamma| < 0.6$. Results with the template fit method.

Figure 36: Measured vs expected inclusive prompt photon production cross section, for photons with transverse energies above 15 GeV and in the pseudorapidity range $0.6 \leq |\eta^\gamma| < 1.37$. Results with the template fit method.

Figure 37: Measured vs expected inclusive prompt photon production cross section, for photons with transverse energies above 15 GeV and in the pseudorapidity range $1.52 \leq |\eta^{\gamma}| < 1.81$. Results with the template fit method.

10 Discussion

In general, the measured cross sections are in agreement with the theoretical predictions for $E_T^\gamma > 25$ GeV. The large-E_T^γ regions are easier to probe experimentally, as the signal to background ratios after the tight selection criteria improve substantially. This leads to smaller relative systematic uncertainties, which should become even smaller in future measurements as an improved understanding of the detector allows for better estimates of both the efficiencies and purities.

For $E_T^\gamma < 25$ GeV, in the two pseudorapidity regions covered by the electromagnetic calorimeter barrel ($|\eta^\gamma| < 0.6$ and $0.6 \leq |\eta^\gamma| < 1.37$) the data seem to favor lower values of the cross section than those predicted by JETPHOX. Such low transverse energies at the LHC represent extremely small values of $x_T = E_T^\gamma/\sqrt{s}$, where NLO theoretical predictions are less well understood. For instance, in such a regime the appropriate values of the different scales are far from clear, and the uncertainties associated with these scales in the theoretical predictions may not be well modeled by simple variations of any one scale about the default value of E_T^γ [36]. As the low-E_T^γ region is exactly where the fragmentation component has the most significant impact on the total cross section, the total uncertainty associated with NLO predictions at low E_T^γ may be underestimated.

Finally, the experimental measurements at low E_T^γ have large associated systematic uncertainties that reduce the significance of the observed disagreement between data and theory. An improved measurement of the isolated prompt photon cross section, benefitting from an improved understanding of the ATLAS detector gained with a significantly larger data sample, is needed to further investigate these effects.

11 Conclusion

A measurement of the differential cross-section for the inclusive production of isolated prompt photons in pp collisions at a center-of-mass energy $\sqrt{s} = 7$ TeV has been performed, using 880 nb^{-1} of collision data collected with the ATLAS detector at the LHC. The results have been compared with next-to-leading order theoretical predictions. For $E_T^\gamma > 25$ GeV, where both the theoretical and experimental measurements benefit from smaller systematic uncertainties, the data and theory are in agreement. For $E_T^\gamma < 25$ GeV, the data appear to favor smaller values of the cross section for $E_T^\gamma < 25$ GeV than those predicted by theory. In this region the experimental measurements have large associated systematic uncertainties, while theoretical predictions of the inclusive cross section also become difficult at such low values of $x_T = E_T^\gamma/\sqrt{s}$. The measured prompt-photon cross section is more than a factor of thirty higher than that measured at the Tevatron, and a factor of 10^4 higher than for photoproduction at HERA, assuming a similar kinematic range in transverse momentum and pseudorapidity. This will allow the extension of the measurement up to energies in the TeV range after only a few years of data taking at the LHC.

References

[1] P. Aurenche, R. Baier, M. Fontannaz, and D. Schiff, *Prompt photon production at large p_T. Scheme invariant QCD predictions and comparison with experiment*, Nucl. Phys. **B297** (1988) 661.

[2] P. Aurenche, R. Baier, M. Fontannaz, J. F. Owens, and M. Werlen, *Gluon content of the nucleon probed with real and virtual photons*, Phys. Rev. **D39** (1989) 3275.

[3] R. E. Blair, S. Chekanov, G. Heinrich, A. Lipatov, and N. Zotov, *Direct photon production at HERA, the Tevatron and the LHC*, Proceedings of the HERA-LHC workshop (CERN-DESY), 2007-2008 (2008) p.681, `arXiv:0809.0846`.

[4] S. Catani et al., *Cross section of isolated prompt photons in hadron-hadron collisions*, JHEP **05** (2002) 028.

[5] P. Aurenche et al., *Recent critical study of photon production in hadronic collisions*, Phys. Rev. **D73** (2006) 094007.

[6] D0 Collaboration, V. M. Abazov et al., *Measurement of the isolated cross section in $p\bar{p}$ collisions at $\sqrt{s} = 1.96$ TeV*, Phys. Lett. **B639** (2006) 151.

[7] CDF Collaboration, T. Aaltonen et al., *Measurement of the inclusive isolated prompt photon cross section in $p\bar{p}$ collisions at $\sqrt{s} = 1.96$ TeV using the CDF detector*, Phys. Rev. **D80** (2009) 111106(R).

[8] ATLAS Collaboration, G. Aad et al., *The ATLAS Experiment at the CERN Large Hadron Collider*, JINST **3** (2008) S08003.

[9] ATLAS Collaboration, G. Aad et al., *Expected Performance of the ATLAS Experiment, Detector, Trigger and Physics: Calibration and Performance of the Electromagnetic Calorimeter*, CERN-OPEN-2008-020 (2008) 44–71, `arXiv:0901.0512 [hep-ex]`.

[10] ATLAS Collaboration, *Electron and photon reconstruction and identification in ATLAS: expected performance at high energy and results at 900 GeV*, ATLAS-CONF-2010-005 (2010) .

[11] ATLAS Collaboration, *Purity Estimates for the Inclusive Isolated Photons*, ATL-COM-PHYS-2010-804 (2010) .

[12] T. Sjöstrand et al., *High-Energy-Physics Event Generation with* `PYTHIA` *6.1*, Computer Phys. Commun. **135** (2001) 238.

[13] A. Sherstnev and R. S. Thorne, *Parton distributions for LO generators*, Eur. Phys. J. **C55** (2008) 553.

[14] ATLAS Collaboration, G. Aad et al., *ATLAS Monte Carlo tunes for MC09*, ATL-PHYS-PUB-2010-002 (2010) .

[15] GEANT4 Collaboration, S. Agostinelli et al., `GEANT4` *- a simulation toolkit*, Nucl. Instrum. Methods A **506** (2003) 250.

[16] ATLAS Collaboration, G. Aad et al., *The ATLAS Simulation Infrastructure*, ATLAS-SOFT-2010-01-004 (2010) , `arXiv:1005.4568 [physics.ins-det]`. Submitted to Eur. Phys. J. C.

[17] G. Corcella et al., `Herwig` *6.5*, JHEP **0101** (2001) 010.

[18] ATLAS Collaboration, G. Aad et al., *Expected Performance of the ATLAS Experiment, Detector, Trigger and Physics: Reconstruction of photon conversions*, CERN-OPEN-2008-020 (2008) 112–140, `arXiv:0901.0512 [hep-ex]`.

[19] M. Aharrouche et al., *W → ev and Z → ee cross-section measurements in pp collisions at $\sqrt{s} = 7$ TeV with the ATLAS Detector: Support note to publication*, ATL-COM-PHYS-2010-701 (2010) .

[20] ATLAS Collaboration, *Photon Identification for the Measurement of the Inclusive Isolated Photon Cross Section*, ATL-COM-PHYS-2010-803 (2010) .

[21] H. Abreu, B. Brelier, V. Dao, M. Delmastro, M. Fanti, J. Hartert, G. Marchiori, T. Koffas, J. Marchand, F. Martin, V. Perez Reale, K. Tackmann, N. Trinh, H. Wang, M. Wielers, S. Wu, and L. Yuan, *Photon performance in the ATLAS experiment*, Tech. Rep. ATL-COM-PHYS-2010-240, CERN, Geneva, May, 2010.

[22] M. Cacciari, G. P. Salam, and S. Sapeta, *On the characterisation of the underlying event*, JHEP **04** (2010) 065, arXiv:0912.4926 [hep-ph].

[23] S. D. Ellis and D. E. Soper, *Successive combination jet algorithm for hadron collisions*, Phys. Rev. D **48** (1993) 3160–3166.

[24] S. Catani, Y. L. Dokshitzer, M. H. Seymour, and B. R. Webber, *Longitudinally invariant K_t clustering algorithms for hadron hadron collisions*, Nucl. Phys. B **406** (1993) 187–224.

[25] M. Cacciari and G. P. Salam, *Dispelling the N^3 myth for the k_t jet-finder*, Phys. Lett. B **641** (2006) 57–61.

[26] G. Voronoi, *Nouvelles applications des paramtres continus la thorie des formes quadratiques.*, Journal für die Reine und Angewandte Mathematik **133** (1907) 97–178.

[27] B. Blair et al., *Theoretical Predictions for Measurements of the Inclusive Isolated Photon Cross Section in pp Collisions at $\sqrt{s}$ = 7 TeV*, ATL-COM-PHYS-2010-805 (2010) .

[28] ATLAS Collaboration, *Evidence for prompt photon production in pp collisions at $\sqrt{s}$ = 7 TeV with the ATLAS detector*, ATLAS-CONF-2010-077 (2010) .

[29] R. Barlow, *SLUO Lectures on Statistics and Numerical Methods in HEP Lecture 9: Unfolding*, Online at http://www-group.slac.stanford.edu/sluo/lectures/stat_lecture_files/sluolec9.pdf.

[30] G. D'Agostini, *A multidimensional unfolding method based on Bayes theorem*, Nucl. Instrum. Methods A **362** (1995) 487–498.

[31] ATLAS Collaboration, *Luminosity determination using the ATLAS detector*, ATLAS-CONF-2010-060 (2010) .

[32] ATLAS Collaboration, *Calibrated Z → ee Invariant Mass*, ATL-COM-PHYS-2010-734 (2010) .

[33] L. Bourhis, M. Fontannaz, J. P. Guillet, and M. Werlen, *Next-to-leading order determination of fragmentation functions*, Eur. Phys. J. **C19** (2001) 89–98, arXiv:hep-ph/0009101.

[34] J. Pumplin et al., *New Generation of Parton Distributions with Uncertainties from Global QCD Analysis*, JHEP **07** (2002) 012.

[35] R. M. Whalley, D. Bourilkov, and R. Group, *The Les Houches accord PDFs (LHAPDF) and LHAGLUE*, arXiv:hep-ph/0009101.

[36] J. P. Guillet and E. Pilon. Private communication, 2010.

[37] M. Cacciari, G. P. Salam, and G. Soyez, *The Catchment Area of Jets*, JHEP **04** (2008) 042.

A Isolation Corrections

The measurement of the prompt photon cross section presented in this note relies on an accurate measurement of the amount of hadronic activity close to the photon candidates. A good measurement of this isolation energy will allow for an improved rejection of background, as the dominant backgrounds to prompt photons will tend to have large isolation energies, while prompt photons themselves will often be well separated from additional hadronic activity.

Due to the power of an isolation cut when attempting to reduce the background, theoretical predictions of the inclusive prompt photon cross section typically allow for some optional cut on the isolation of true photons at the parton level. The `JetPhox` program, for instance, implements several kinds of isolation cuts. However, such programs typically compute the isolation energy at the parton level, while an experimental measurement of the isolation energies of real photons is only made after hadronization. Furthermore, `JetPhox` includes no model of the underlying event, and is incapable of including the effects of pileup, both of which will tend to skew the measured isolation energies towards higher values. Finally, the measurement of the isolation energy will be sensitive to detector resolution and smearing effects, which are certainly not included in any pure Monte Carlo prediction. All of these effects must be addressed when associating the experimental isolation with the isolation at the parton level.

Isolation energy measurements can either be track-based or calorimeter-based; in this paper, a definition based on calorimeter energies is used, as it also accounts for energy from neutrals, and is easier to associate with a theoretical prediction of the isolation energy. The energy is typically integrated over some cone in (η, ϕ) space around the photon candidate: theoretical predictions prefer larger cones (to reduce the sensitivity of the prediction to the details of soft gluon emission around the photon), while on the experimental side, a smaller cone is preferred (to avoid large effects from detector smearing and soft-physics). The cone radius used in this analysis, $dR = .4$, was chosen to balance these two constraints.

This appendix will describe the measurement of the isolation energy in the calorimeter, and the corrections made to that measurement to remove both detector effects and contributions from soft physics unrelated to the hard process.

A.1 Isolation Energy in the Calorimeters: EtCone Variables

In ATLAS, the most common measurements of the isolation energy for electrons and photons are the `EtCone` energies. These quantities are computed as part of the normal e/gamma reconstruction for electrons and photons, and consist of a sum of the transverse energies of all calorimeter cells (electromagnetic and hadronic) found within some radius dR. The radius of the cone, multiplied by 100, is appended as a suffix to the variable name; *e.g.*, the variable `EtCone40` uses a cone of radius $dR = \sqrt{\Delta\eta^2 + \Delta\phi^2} = .4$.

The transverse energy within the cone of radius dR is dominated by the transverse energy of the photon candidate itself. To remove this contribution, a grid of cells in the center of the cone, with an area corresponding to a 5×7 ($\eta \times \phi$) grid of cells in the second sampling of the electromagnetic calorimeter, is excluded from the sum. This subtraction only includes cells from the electromagnetic calorimeter; the contributions for all cells in the Tile Calorimeter are kept in the isolation energy sum.

The `EtCone40` distribution for reconstructed tight photons with $p_T > 20$ GeV, extracted from a sample of filtered dijets, is shown in Figure 38a. The direct, brem, and background components are shown separately: the prompt components have small values of isolation, while the background has a long tail towards high isolation energies.

A.2 Detector Effects

At the parton level, direct photons should have very little nearby hadronic energy. However, Figure 38a shows a distribution for direct photons that has a Gaussian core with a non-trivial width, and which is

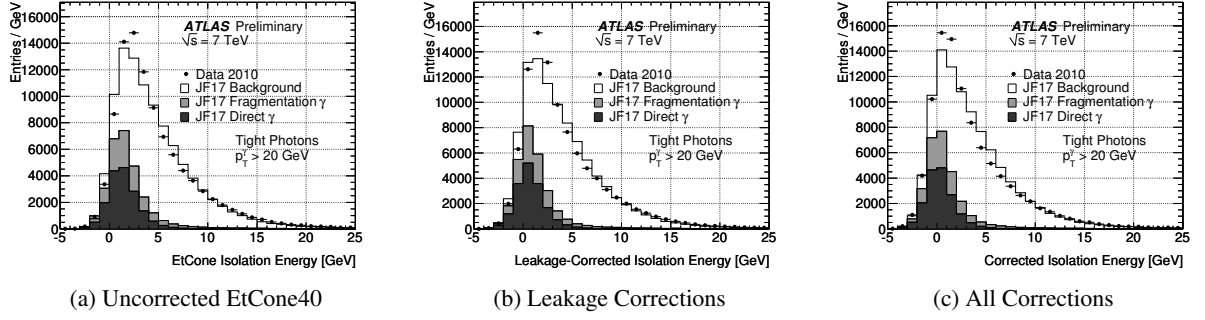| (a) Uncorrected EtCone40 | (b) Leakage Corrections | (c) All Corrections |

Figure 38: The EtCone40 isolation energy profile for direct, brem, and background photons which pass the tight identification criteria and have $p_T > 20$ GeV, extracted from filtered dijet events. Figure (a) shows the isolation profiles with no corrections applied; Figure (b) shows the isolation profiles after the out-of-core leakage corrections; Figure (c) shows the isolation profiles after both the leakage and jet-area corrections have been applied.

not centered at zero. This could be due to soft physics (underlying event or pileup) or detector resolution effects. To study the impact of detector effects on the isolation profile of signal photons, a study was carried out with single particle Monte Carlo samples, with photons spread over the entire η range, and covering photon transverse energies from 7 GeV to 500 GeV.

The `EtCone` variables approximate the contribution of the photon energy to the isolation cone by summing the cells in the middle of the isolation cone, and excluding that sum from the final estimate. This may be a reasonable approximation to first order, but the photon candidate will deposit some of its energy outside of this central core, leading to leakage effects which will scale with the p_T of the photon. The effect of this leakage is shown in Figure 39a, as a function of the photon p_T, and for three different regions in $|\eta|$. Figure 39b shows the leakage effect as a function of the cone size; the leakage is linearly related to both the radius of the cone and the p_T of the photon. Table 32 lists the scale factors extracted from plots like those in Figure 39a; the scale factors range from less than 1% to almost 6%, depending on $|\eta|$ and the size of the cone.

The isolation distributions for tight photons in simulation are shown again in Figure 38b, after correcting for these leakage effects. The distribution for direct photons has a slightly narrower width compared with Figure 38a, and a mean that has shifted closer to zero. The residual width in the distribution for direct photons is due to noise in the calorimeter, primarily in the electromagnetic calorimeter, which has a width of roughly 1.5 GeV for a cone of radius $dR = .4$. The noise distribution is centered at zero, and therefore leads to possible negative values of the isolation energy.

A.3 Effects from Soft Physics

The effects of the underlying event on the isolation cone, as well as any additional contributions from pileup, also need to be estimated. Compensations for such effects are sometimes made by subtracting some fixed value from the isolation energy based on the number of primary vertices in the event [7]. This, however, does not account for potentially large event-to-event fluctuations in the ambient energy. An alternative proposal for an event-by-event ambient energy correction was first introduced in [37], and is explained in more detail in [22].

In ATLAS, the algorithm for calculating the event-by-event corrections for soft physics is implemented as follows:

- First, a special jet collection is reconstructed. The jet p_T threshold is set to 0, and as the jet

(a) p_T effects, η regions

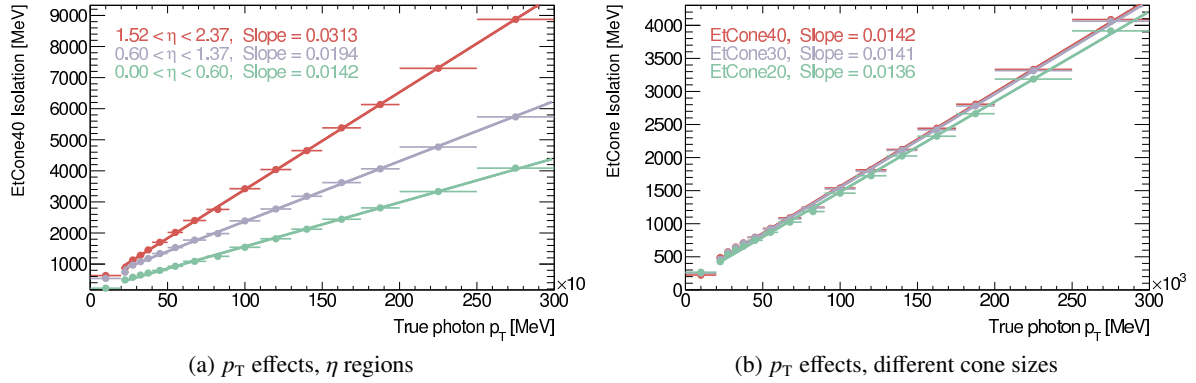(b) p_T effects, different cone sizes

Figure 39: The behavior of the cone isolation variable as a function of the photon p_T. Figure (a) shows the EtCone40 distribution for three different η regions, while (b) shows different cone sizes (.20, .30, and .40) for $|\eta| < .6$. Similar plots have been produced for all $|\eta|$ regions and cone sizes, with slopes ranging from 1.4% at low $|\eta|$ to 4.5% at high $|\eta|$. The slope represents the transverse energy leakage of the photon outside of the central core, less the transverse leakage outside of the outer cone. The fit is performed for $p_T > 20$ GeV.

	Isolation Cone Size						
	.10	.15	.20	.25	.30	.35	.40
$0.00 < \eta < 0.10$	.008	.013	.015	.015	.015	.015	.015
$0.10 < \eta < 0.60$	.008	.013	.014	.014	.014	.014	.014
$0.60 < \eta < 0.80$	.007	.012	.014	.014	.014	.014	.014
$0.80 < \eta < 1.15$	.008	.016	.018	.019	.019	.019	.019
$1.15 < \eta < 1.37$	.009	.018	.021	.022	.022	.022	.022
$1.37 < \eta < 1.52$	.010	.020	.023	.024	.025	.025	.026
$1.52 < \eta < 1.81$	.011	.020	.023	.024	.024	.025	.025
$1.81 < \eta < 2.01$	.012	.024	.027	.028	.029	.029	.029
$2.01 < \eta < 2.37$	.015	.030	.035	.036	.037	.038	.037
$2.37 < \eta < 2.47$	.018	.035	.041	.041	.044	.046	.046
$2.47 < \eta < 5.00$	.031	.040	.043	.044	.045	.045	.046

Table 32: Corrections applied to EtCone variables, for photons, to correct for p_T leakage outside of the subtracted core. The numbers in this table are multiplied by the photon p_T and subtracted from the EtCone isolation energy.

reconstruction proceeds, each jet is assigned an area based on a Voronoi segmentation of the (η, ϕ) space [37]. This analysis uses a k_T jet reconstruction algorithm, with a size parameter of .5, running on EM-scale topoclusters.

- A transverse energy density is calculated for each jet, equal to its transverse energy divided by its area.

- The detector is then divided into regions in η, and the reconstructed jets are each assigned to a region. The size of the regions must be large compared with the size of the jets to avoid boundary effects; in this case, the regions are $\eta < 1.5$ and $1.5 < \eta < 3.0$. This has the added effect of separating the barrel and endcap calorimeters.

- Within each region in η, the jets are ordered by their energy densities, and the median energy density is used as the estimate of the ambient energy for the entire region. There is no upper limit on the jet p_T used in this correction, as any such threshold would introduce an arbitrary scale. The choice of the median, as opposed to the mean, is motivated by the desire to avoid any effects from very energetic jets, which are likely not correlated with the soft physics being measured.

- This ambient energy density is then used to correct the isolation energy of photons, by multiplying the energy density by the active area of the isolation cone [5], and subtracting that contribution from the EtCone value.

The results of the ambient energy estimation for data and MC, in events where only one primary vertex is reconstructed, are shown in Figure 40a. The data and MC are not expected have the same distributions of ambient energy densities, but the comparison is still instructive. The same comparison for events with four primary vertices is shown in Figure 40b. The trend of the mean ambient energy density, as a function of the number of primary vertices, is shown in Figure 41. The average increase in the ambient energy density is roughly 400 MeV per vertex; for a cone of radius .4, this corresponds to an increase of roughly 200 MeV per vertex to the isolation energy. The trend of the mean ambient energy density as a function of the p_T of tight photon candidates is shown in Figure 42. There is some small increase in the estimated energy density as a function of the photon p_T. One possible cause of this effect is a residual pull of the ambient energy to larger values from the photon itself (which is also reconstructed as a jet, and used in the determination of the ambient energy). However, removing the one or two hardest jets in the event from the search for the median energy density does not remove the p_T dependence of the average computed energy densities (though it does reduce the average computed energy density for all p_T).

A.4 Results

The fully corrected EtCone40 distributions corresponding to the distributions in Figure 38a are shown in Figure 38c. These distributions include both the p_T-leakage and jet-area corrections. The distribution for direct photons is now almost centered at zero, without a significant change in the width of the core (this indicates that the jet-area corrections introduce no significant smearing effects on the isolation energy resolution).

The large signal-to-background ratio of photon candidates at high transverse energy allows for a check of the corrections on a signal-rich sample. The isolation distributions for photons with $E_T^\gamma > 50$ GeV, before and after corrections, are shown in Figure 43a. The corrections introduce a large shift towards lower isolation energies; this shift is dominated by the corrections for the out-of-core leakage

---

[5]The active area is defined as πR^2 minus the area corresponding to the 5×7 cells at the center of the cone, where R is the radius of the cone (typically $R = .4$).
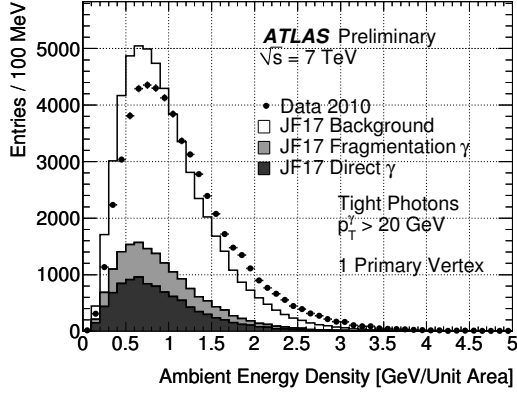
(a) 1 Primary Vertex
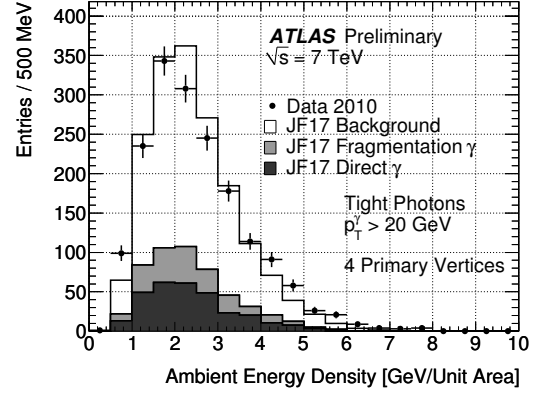
(b) 4 Primary Vertices

Figure 40: The energy density as computed by the area correction technique, for events containing tight photon candidates, and only one (a) or four (b) reconstructed primary vertices with three or more tracks.
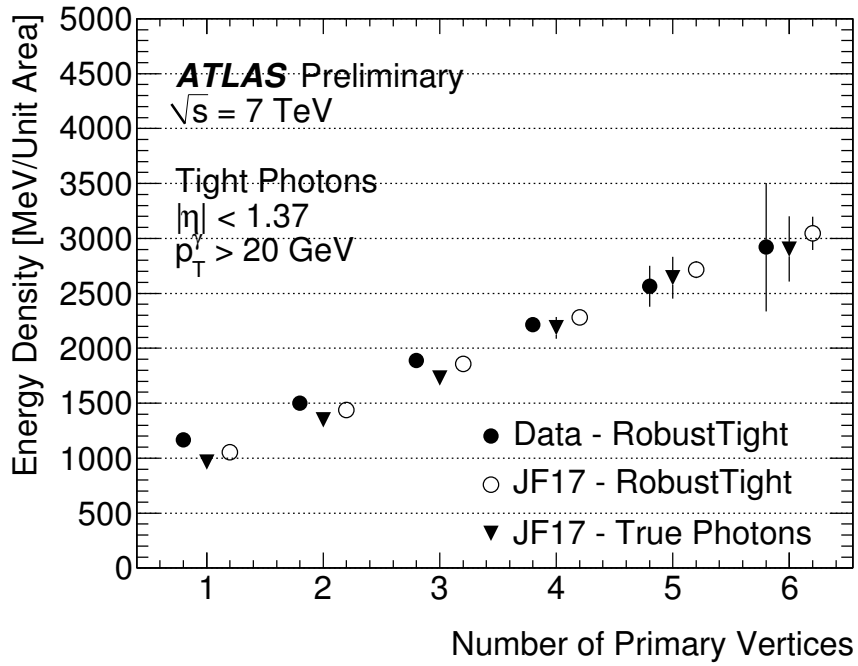

Figure 41: The mean of the energy density as a function of the number of reconstructed primary vertices with three or more associated tracks.
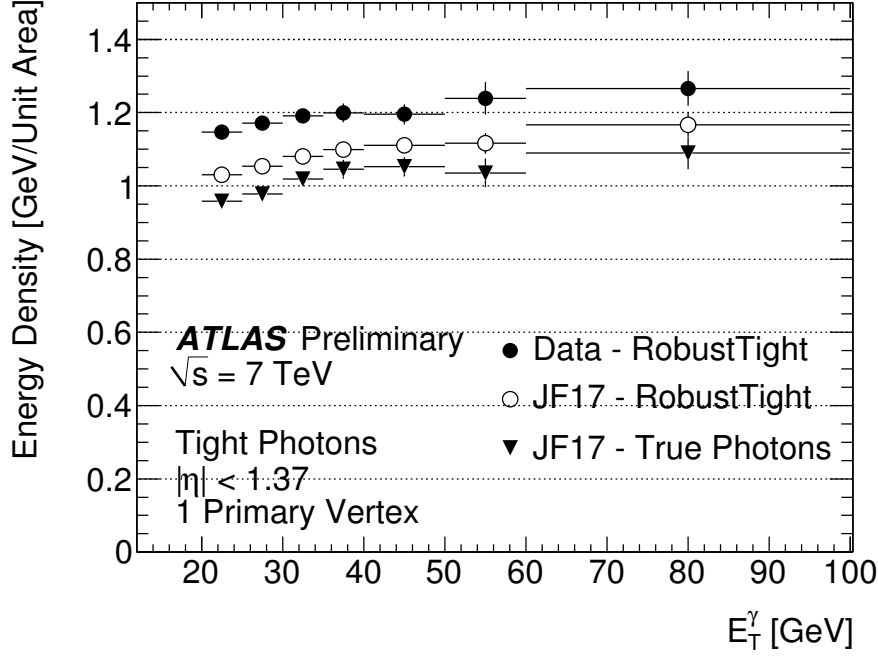
Figure 42: The ambient energy density calculated with the jet-area method as a function of the p_T of the photon candidate, for events with one reconstructed primary vertex. The photon candidates are also restricted to the barrel region of the calorimeter.

of the photon. The signal/background separation improves slightly as a result of the shift, as the signal concentrates at low isolation energies, and the background is less affected. A similar comparison can be made with electrons from W and Z decays, and is shown in Figure 43b. In this case, the sample is already expected to be very pure, so the effects on the residual background are less apparent. The effect of the corrections on the signal is not as large as it is on high-p_T photons due to the softer p_T spectrum of the electron sample (which leads to smaller leakage corrections).

Figure 44 shows the effects of the underlying event corrections in different MC models, by calculating the ambient energy densities for PYTHIA and HERWIG filtered dijet events, and the corresponding corrected isolation distributions. The collision data show an excess over MC in the signal-like region of the isolation distribution, consistent with the larger purities seen in collision data than in MC. The ambient energy densities are not identical between the three cases, but even though there are obvious shape differences, none of the distributions appear to show pathological behavior, or exhibit any signs of significant differences in the tails of the distributions that would cause large effects on the measured cross section.

A.5 Effect on the Measured Cross Section

To evaluate the impact of the underlying event correction on the cross section, the signal yields are estimated with the corrected and uncorrected isolation energies. The yields are estimated using the two-template-fit method for events with a single reconstructed primary vertex, after applying all of the other selection criteria described in this note. The yields, with and without corrections, are shown in Figure 45 for all pseudorapidity regions. The yields in both cases are evaluated after a 3 GeV cut on the isolation energy. Because the corrections are uniformly positive, this means that the effective cut on the
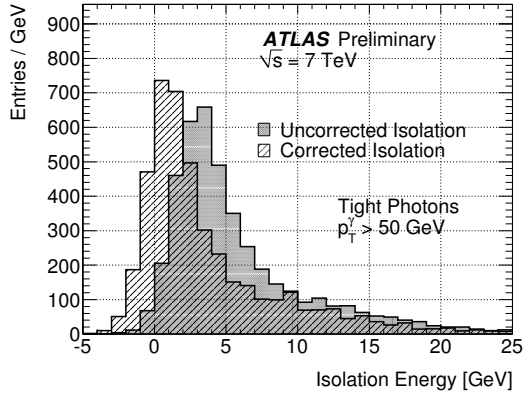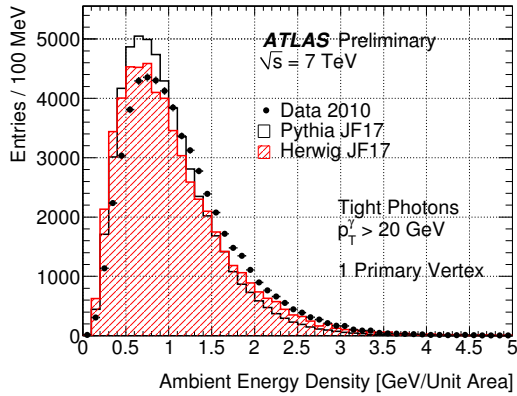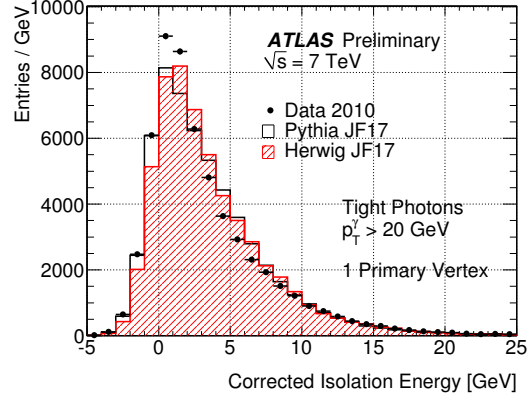
(a) High p_T Photons
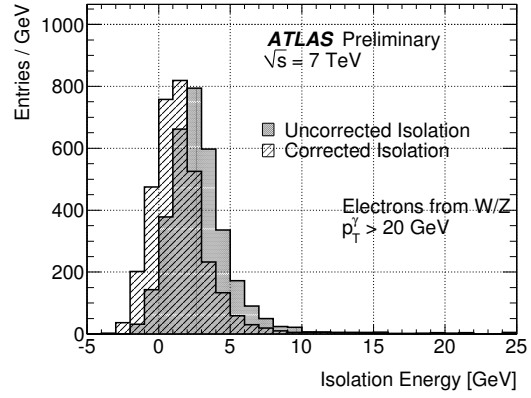
(b) Electrons from W and Z Decays

Figure 43: The isolation energies of high p_T photons (a) and electrons from W and Z decays (b), before and after the isolation corrections are applied, measured in collision events. The total shift for the high-p_T photons is dominated by the corrections for out-of-core leakage.

(a) Ambient Energy

(b) Corrected Isolation

Figure 44: The energy density as computed by the area correction technique (a), and the fully corrected isolation profile (b), for events containing tight photon candidates, and only one reconstructed primary vertex with three or more tracks, for photon candidates in Pythia, Herwig, and collision data.

(a) Uncorrected Isolation, 3 GeV Cut   (b) Uncorrected Isolation, 3.54 GeV Cut   (c) Corrected Isolation, 3 GeV Cut
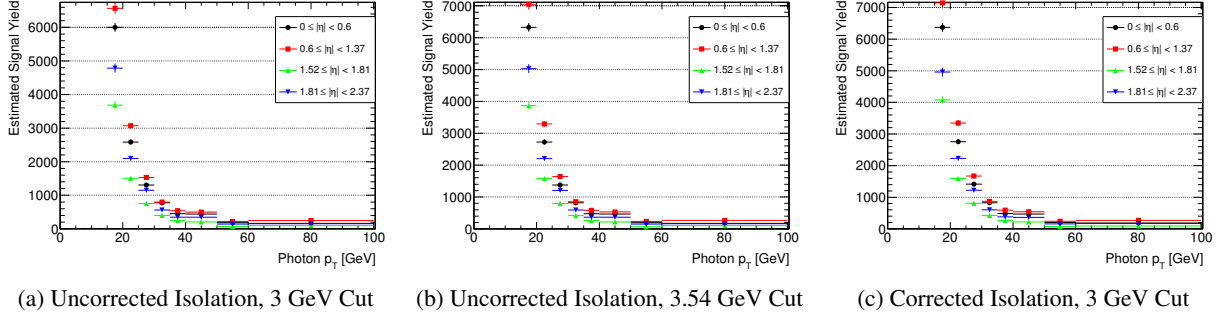
Figure 45: The estimated signal yields for photon candidates passing all the nominal selection criteria, in events with one reconstructed primary vertex. The three cases represent the signal yields estimated after: an isolation cut of 3 GeV on the uncorrected isolation energy (a); a cut of 3.54 GeV on the uncorrected isolation energy (b); and a cut of 3 GeV on the corrected isolation energy (c). Plot (c) corresponds to the nominal analysis presented in this note, with only the additional requirement that there be a single primary vertex. Cases (a) and (b) serve to show the expected signal yields when not correcting for the underlying event. In case (b), the 540 MeV added to the cut represents the mean underlying event correction for events with a single primary vertex, as seen in data.

uncorrected isolation energies is tighter than the same cut on the corrected energies. Figure 46 shows the signal yields with no corrections, normalized to the corresponding yields with corrections. The error bars correspond to statistical uncertainties only. The overall impact of the corrections appears to be a 7% increase in the signal yield, with no apparent trend in E_T^γ or η^γ.

As an additional check, the same test was carried out, but comparing a cut of 3540 MeV on the uncorrected isolation with a cut of 3000 MeV on the corrected isolation. The additional 540 MeV represents the mean correction applied to tight photons in collision events with a single reconstructed primary vertex. The results, normalized to the yields with the corrections, are shown in Figure 47. The yields are consistent within statistical uncertainties between the two cases, implying that the impact of the event-by-event corrections is equivalent to the impact of single correction applied to all photon candidates.

The same exercise can be carried out in MC samples, where the truth-level cross sections are known, and the backgrounds can be removed. The results are shown in Figures 48, 49, 50, and 51. In Pythia, the mean correction for the underlying event is 444 MeV, while in Herwig the mean correction is 554 MeV; this difference is indicative of the differences between the corresponding models of the underlying event. As seen with data, the underlying event corrections show no apparent E_T^γ or η^γ dependence, and show that the event-by-event corrections are completely equivalent to an average correction applied to all candidates.
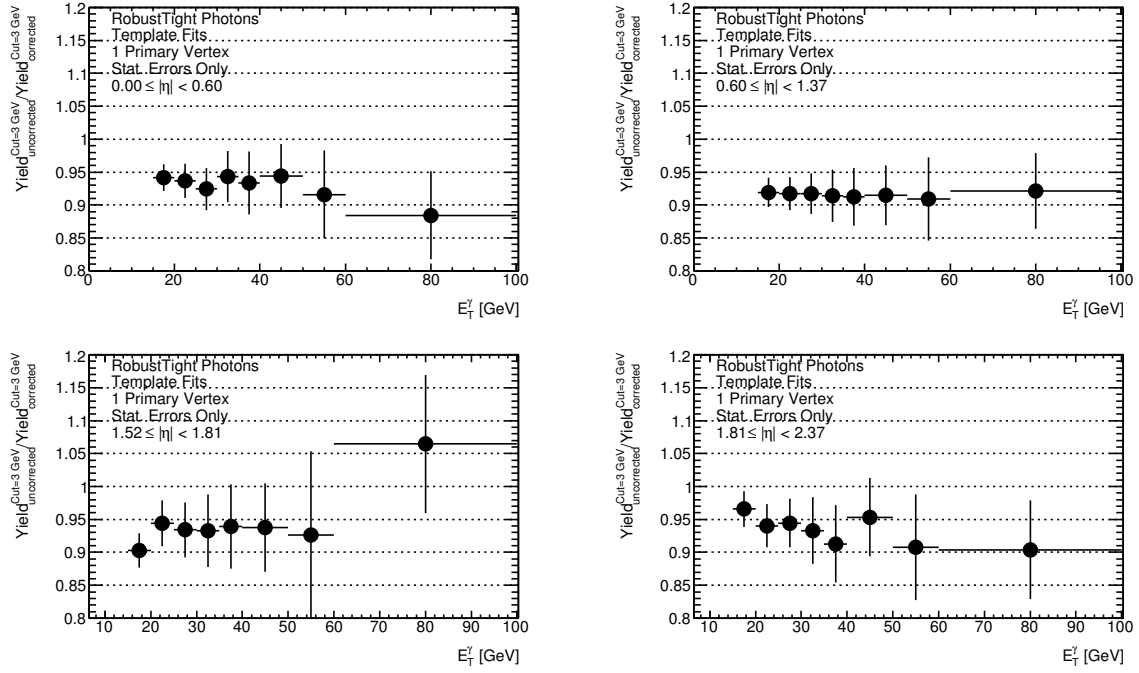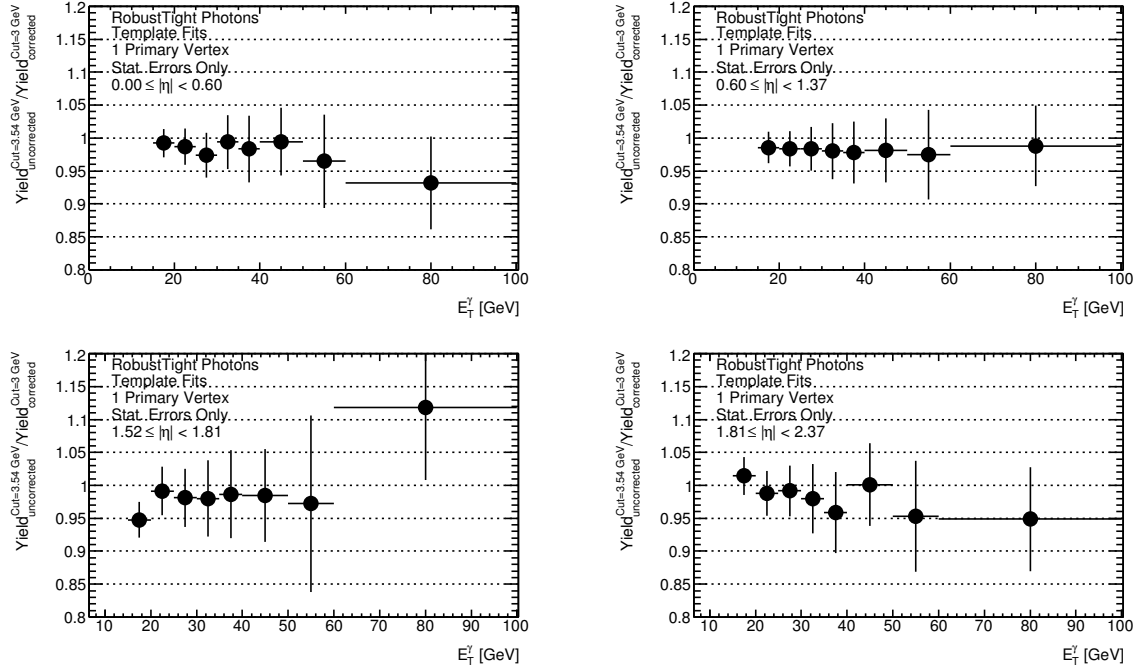
Figure 46: The estimated signal yields when applying a 3 GeV cut on the uncorrected isolation energy, normalized to the estimated yields after applying a 3 GeV cut on the corrected isolation energy. The error bars represent statistical uncertainties only. No apparent trend is seen as a function of E_T^γ or η^γ. The drop in the signal yield due to the missing corrections is $\approx 7\%$.

Figure 47: The estimated signal yields when applying a 3.54 GeV cut on the uncorrected isolation energy, normalized to the estimated yields after applying a 3 GeV cut on the corrected isolation energy. The error bars represent statistical uncertainties only. No apparent trend is seen as a function of E_T^γ or η^γ. The 540 MeV addition to the cut on the uncorrected energy represents the mean correction applied to tight photons in collision events with a single reconstructed primary vertex. The signal yields for in the uncorrected case are consistent with the yields in the corrected case, within statistical uncertainties.
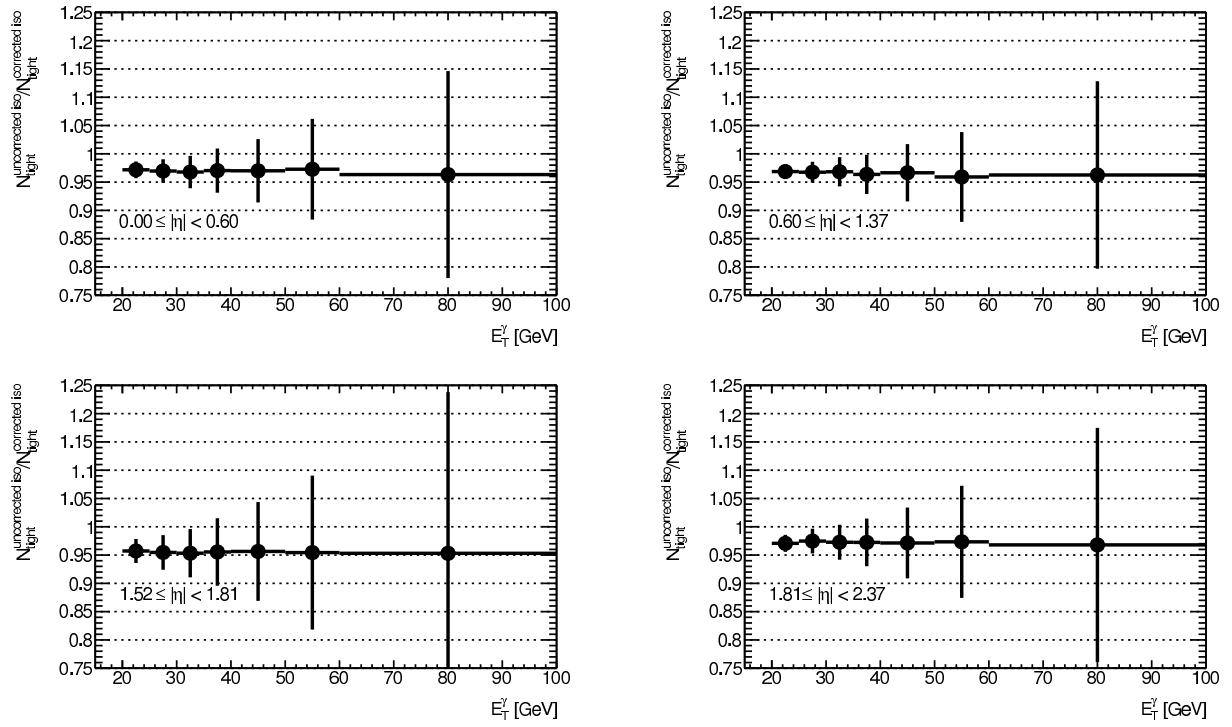
Figure 48: The estimated signal yields in a pure sample of true prompt photons generated in PYTHIA, after making a 3 GeV cut on the uncorrected isolation, normalized to the signal yields estimated from the same sample after making a 3 GeV cut on the corrected isolation.
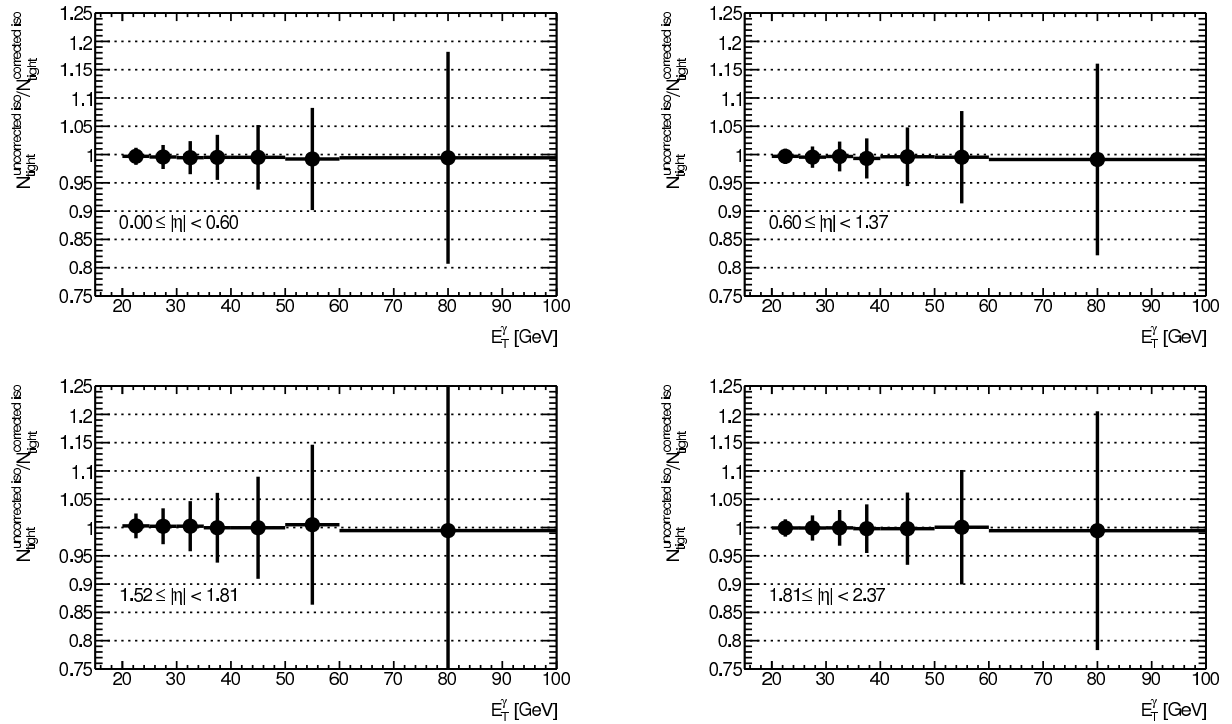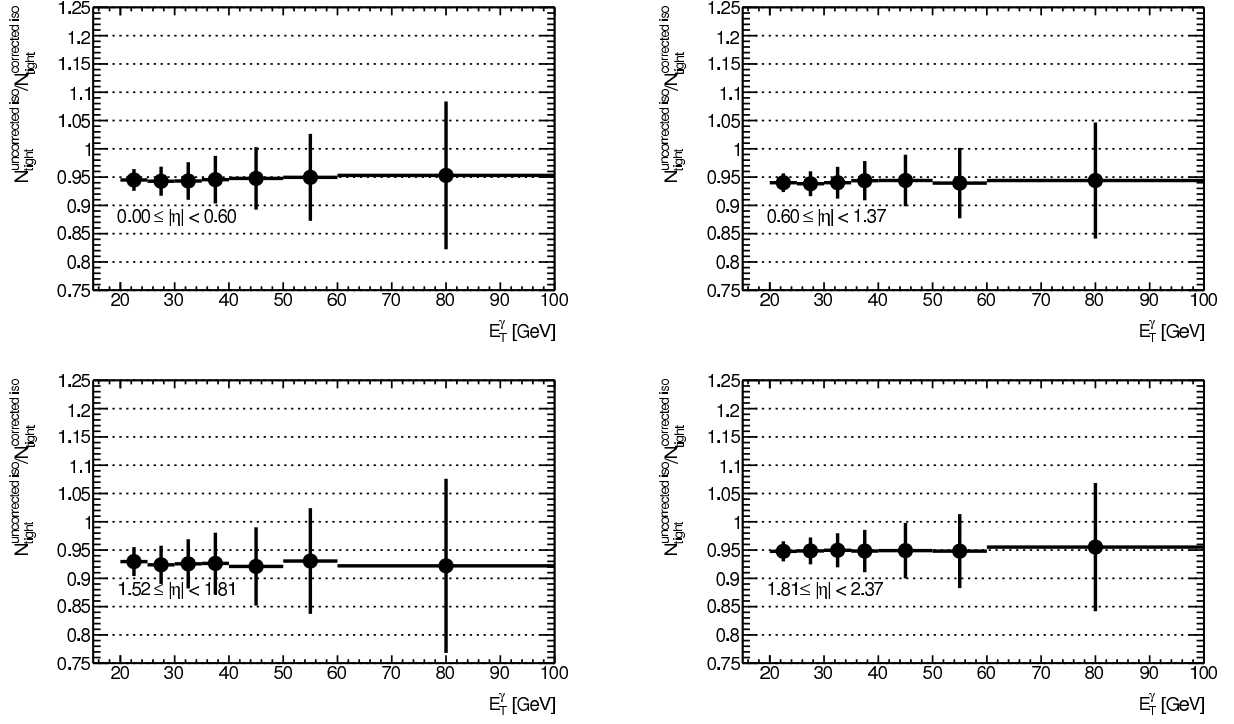

Figure 49: The estimated signal yields in a pure sample of true prompt photons generated in PYTHIA, after making a 3.444 GeV cut on the uncorrected isolation, normalized to the signal yields estimated from the same sample after making a 3 GeV cut on the corrected isolation.

Figure 50: The estimated signal yields in a pure sample of true prompt photons generated in HERWIG, after making a 3 GeV cut on the uncorrected isolation, normalized to the signal yields estimated from the same sample after making a 3 GeV cut on the corrected isolation.
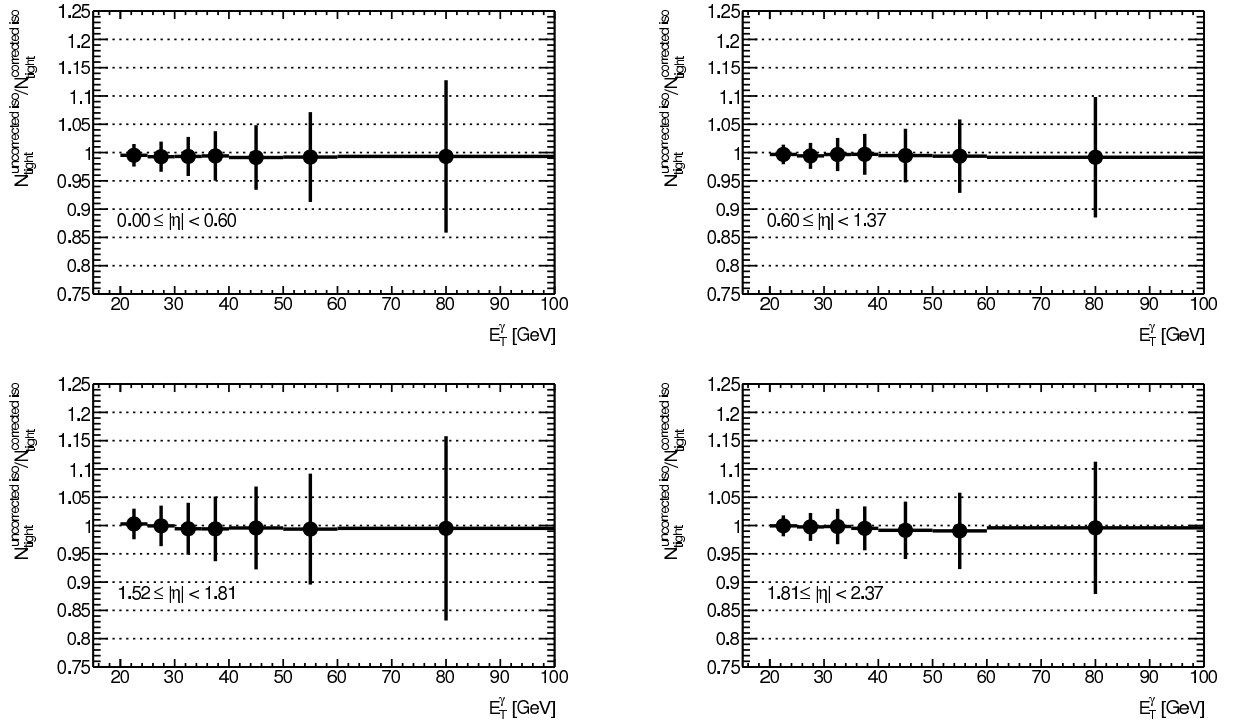

Figure 51: The estimated signal yields in a pure sample of true prompt photons generated in HERWIG, after making a 3.554 GeV cut on the uncorrected isolation, normalized to the signal yields estimated from the same sample after making a 3 GeV cut on the corrected isolation.